CONDENSATION OF CO_2 IN BRAZED PLATE HEAT EXCHANGERS

By

NIEL MARTIN HAYES

A thesis submitted in partial fulfillment of
the requirements for the degree of

MASTER OF SCIENCE IN MECHANICAL ENGINEERING

WASHINGTON STATE UNIVERSITY
SCHOOL OF ENGINEERING AND COMPUTER SCIENCE

AUGUST 2009

To the Faculty of Washington State University:

The members of the Committee appointed to examine the thesis of NIEL MARTIN HAYES find it satisfactory and recommend that it be accepted.

Amir Jokar, Ph.D., Chair

Stephen Solovitz, Ph.D.

Wei Xue, Ph.D.

ACKNOWLEDGMENT

I would like to acknowledge a man who has been my advisor, mentor, and personal friend over the past two years, Dr. Amir Jokar. He has gone above and beyond the call of being a professor and research investigator throughout the course of my graduate studies. I hold Dr. Jokar in high esteem, for his exemplary leadership skills, his integrity, as well as his camaraderie. I also need to thank the American Society of Heating Refrigeration and Air-conditioning Engineers (ASHRAE) who sponsored the research project which I have worked on for the span of my time at WSU Vancouver. Lastly, I would like to recognize my parents who have been very supportive and influential in my decisions throughout my life, including furthering my education.

CONDENSATION OF CO_2 IN BRAZED PLATE HEAT EXCHANGERS

Abstract

by Niel Martin Hayes, M.S.
Washington State University
August 2009

Chair: Amir Jokar

The experimental study of carbon dioxide condensation in brazed plate heat exchangers is the main objective of this research project. The current level of concern for our environment is at an all time high, and as such, it is important that we look to methods and resources that will lead to a cleaner and healthier future for the planet. This thesis details one such effort to reach this goal, focusing on how a natural refrigerant undergoes the condensation step of the refrigeration cycle in compact heat exchangers.

Condensation flow consists of two phases, vapor and liquid, existing simultaneously, however, in order to analyze and formulate the two-phase flow characteristics, it is essential to characterize the single-phase flow through the tested minichannel heat exchangers. Three brazed plate heat exchangers with different interior configurations, each consisting of three channels, are considered and tested in this study.

For the single-phase analysis, data were taken using hot and cold water counter flowing through the middle and side channels, respectively. Data were also taken flowing hot water in the middle and chilled dynalene in the surrounding channels. The modified Wilson plot technique was applied to obtain single-phase heat transfer coefficients, and the Fanning friction factor was estimated for the pressure drop. The resulting correlations were within reasonable ranges of standard deviation and uncertainty, and compared well with other relevant studies.

For the two-phase analysis, carbon dioxide was the working fluid, flowing through the middle channel, while dynalene, the cooling fluid, flowed through the side channels of the three different exchangers. Condensation of carbon dioxide occurred at saturation temperatures ranging from 0°F (-17.8°C) to -30°F (-34.4°C) and heat fluxes spanning 800 Btu/hr.ft^2 (2.5 kW/m^2) to 5,000 Btu/hr.ft^2 (15.7 kW/m^2). Comparisons of the two-phase heat transfer and pressure drop characteristics are given for the heat exchangers, and conclusions are made from the two-phase data. The purpose of this study is to mathematically understand the condensation behavior of CO_2 in brazed plate heat exchangers; not to compare different refrigerants' capacities with that of CO_2 or compare heat exchanger performances one with another.

TABLE OF CONTENTS

Page

LIST OF TABLES

LIST OF FIGURES

LIST OF FIGURES

Page

LIST OF FIGURES

NOMENCLATURE

A_s: heat transfer surface area (m^2)
A_o: minimum free flow open area between two neighboring plates (mm^2)
$A_{onepass}$: single smallest cross sectional area of flow within channel in BPHE (mm^2)
b: average plate spacing (mm)
Bo: boiling number, dimensionless
C: constant
C_p: specific heat (J/kg. K)
C_f: Fanning friction factor
D: diameter (m, in.)
D_{hyd}: hydraulic diameter (taken as twice the mean plate spacing in PHEs) (m, in.)
g: gravity acceleration (m/s^2)
G: mass flux ($kg/m^2.s$)
H: dimensionless parameter accounting for sub-cooling in the condensate film
h: heat transfer coefficient (W/m^2. K)
h_{fg}: latent heat (J/kg)
i: enthalpy (J/kg)
Δh_{fg}: specific enthalpy of vaporisation (J/kg)
Ja: Jakob number
k: thermal conductivity (W/m .K)
KE: kinetic energy
L_T: plate length (mm, in.)
L_{HT}: heat transfer length (bottom of top port to top of bottom port) (mm, in.)
L_P: pressure drop length (middle of top port to middle of bottom port) (mm, in/)
$\dot{m}$: mass flow rate (kg/s)
N: number of plates
Nu: Nusselt number
P: Reynolds number power coefficient
p: system pressure (Pa, psi)
Pr: Prandtl number
q'': heat flux (W/m^2, $Btu/ft^2.s$)
Re: Reynolds number
S: nominal heat transfer area
T: temperature (^oC)
t: plate thickness (mm, in.)
U: overall heat transfer coefficient (W/m^2. K)
u: flow velocity (m/s)
V: volume (m^3)
$\dot{V}$: volume flow rate (m^3/s, gpm)
w: width of BPHE (mm, in.)

Greek Symbols:
β: plate corrugation inclination angle (deg.) measured from horizontal
ΔJ: specific enthalpy of vaporization (J/kg)
ΔP: pressure drop (Pa, psi)
ΔT: temperature difference (°C)
λ: corrugation pitch (mm, in.)
μ: dynamic viscosity (cP,)
ξ: friction coefficient of single phase
ρ: density (kg/m^3)
Φ: enlargement factor

Subscripts:
c: cold side (heat absorption channels)
CO: condensation
eq: equivalent values
f/F frictional
fg: difference between liquid and vapor phase properties
film: film condensation
g: gas (vapor)
gr: gravitational
h: hot side (heat rejection channel)
ht: heat transfer
hyd: hydraulic
i: in, entrance side of system
l: liquid
lm: logarithmic mean
m: mean values
man: manifold
o: out, exit side of system
p: plate
s: at surface condition
sat: saturation
sp: single-phase
sub: sub cooled
sup: superheat
t: thickness
tot: total
tp: two-phase
v: vapor
w: water

CHAPTER 1: INTRODUCTION

Global warming concerns are gaining momentum in the twenty-first century and as such, environmentally friendly refrigerants are quickly becoming a necessity rather than just an interesting topic to speculate about for the future. Carbon dioxide, CO_2 or R-744, is a top contender, as instigated in the Montreal protocol, to phase out the use of ozone depleting chlorofluorocarbon (CFC) and hydrochlorofluorocarbon (HCFC) refrigerants, especially in low temperature applications. As mentioned by Bodinus [1], the idea of using carbon dioxide as a refrigerant started in the mid 19th Century by Alexander Twining; however, it was not readily implemented until Franz Windhausen made a CO_2 compressor in 1886. CO_2 refrigeration systems gained popularity until the late 1920s and early 1930s in the Great Depression. Due to the rise in demand for smaller systems in the non-commercial refrigeration market, coupled with the extremely high pressures required to use CO_2 as a refrigerant, an innovation was needed. Companies such as General Motors and DuPont funded research to develop new refrigerants that could operate under much lower pressures, as summarized by Pearson [2]. Thus, synthetic CFC refrigerants were invented, which allowed refrigeration units to be sized much smaller and cheaper due to lower working pressure requirements. Figure 1.1 shows the contrast in vapor pressure curves for CO_2 compared with several other refrigerants. When these new refrigerants were developed, research and use of R-744 was close to none-existent.

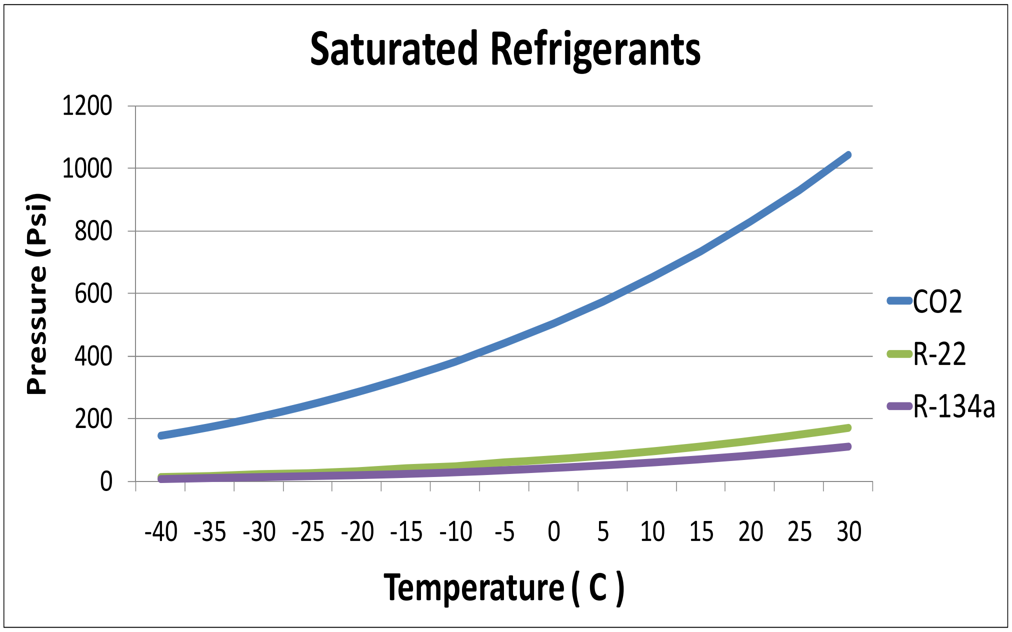

Figure 1.1 Saturated vapor pressure curves of select refrigerants.

With the introduction of the new CFCs/HCFCs refrigerants, such as R-12 and R-22, the refrigeration market's needs were met, but at the same time these innovations created environmental problems. The chlorine molecules in CFCs/HCFCs proved to be harmful when leaked and released into the atmosphere. The ozone molecules in the stratosphere, which protect humans from harmful ultra-violet rays, are absorbed and destroyed by the chlorine molecules through a chemical reaction. In the early 1990s, a few hydrofluorocarbon (HFC) refrigerants, such as R-134a, were developed in which chlorine molecules were totally replaced by hydrogen molecules. In spite of this improvement regarding the ozone depletion problem, HFCs are still not perfect refrigerants due to their excess carbon, which contributes to the potential for global warming. In general, the existing refrigerants in the market today have two potential harmful effects on environment: Global Warming Potential (GWP) and Ozone Depletion Potential (ODP). Global Warming Potential measures how harmful a greenhouse gas can be compared to carbon dioxide, which is defined as the GWP base reference having a value of 1. Ozone

Depletion Potential characterizes how harmful a chemical compound can be in depleting the ozone layer on a scale of 0 to 1. These two measured potentials are typically presented for common refrigerants in Table 1.1.

Table 1.1 Adverse effects of refrigerants on the environment from UNEP [3]

Refrigerants	ODP	GWP (100 year time horizon)
R-12 (CFC)	1.00	10,890
R-22 (HCFC)	0.050	1810
R-134a (HFC)	0	1430
R-744 (CO_2)	0	1

While it is known that CO_2 is one of the most common contributors to global warming problem, the synthetic refrigerants that can leak into the atmosphere are orders of magnitude more harmful to the environment than CO_2. Comparing GWPs and ODPs of R-744 to R-134a, R-22, and R-12 in Table 1.1, one can find that more research and application must be established to further the progress of CO_2 as an eco-friendly refrigerant.

Not only is carbon dioxide promising as a refrigerant with respect to the environment's protection, but it also works as a great refrigerant due to its abundance, safety, as well as its thermophysical properties. Halder and Sarkar [4] found that CO_2 had several advantages over conventional refrigerants, which included lower pumping power requirements (attributed to a lower required volumetric flow rate), higher efficiency in heat exchangers, and higher latent heat. However, one of the leading factors in the decline of CO_2 as a practical refrigerant in the early 20th century was due to the lack of technology in using this refrigerant under its high pressure demands in smaller applications. With the substantial development in heat exchanger and compressor technologies, now CO_2 can seriously be considered as a potential working refrigerant in industrial as well as non-commercial applications.

Since the 1930s, plate heat exchangers have served well for single-phase heat transfer applications, e.g., beverage and food processing, pharmaceutical industries, paper and rubber industries, and dairy pasteurization, as mentioned by Shah and Wanniarachchi [5]. The introduction of brazed plate heat exchangers in the 1970s offered a new manufacturing process that brazes the plates together rather than using gaskets, bolts, and carrying bars. This new technology opened the possibilities of using refrigerants that require higher operating pressures. Plate heat exchangers in general are innovative in how heat transfer is achieved. The compact design allows high heat transfer per unit volume compared to other types of heat exchangers. Complex inner geometries contribute to creating turbulence at relatively low flow rates compared to those of shell and tube exchangers, which results in high heat transfer coefficients at low flows. One of the drawbacks to the brazed plate heat exchanger though, is the difficulty of freeing the plates of fouling, unlike the earlier gasket and bolt plate heat exchangers that could be disassembled, cleaned, and reassembled. If over time fouling buildup occurs in the brazed plate heat exchanger, this could contribute to a decline in plate performance over the life of an exchanger.

This research project was sponsored and supported by the American Society of Heating Refrigeration and Air-conditioning Engineers (ASHRAE) and a company which manufactures heat exchangers. This study focused on the condensation of carbon dioxide in brazed plate heat exchangers. It is one of the first ASHRAE sponsored projects designed to better understand the physics of the condensing phenomenon of carbon dioxide in heat exchangers consisting of complex inner geometries. The objectives for the research project are outlined as follows:

- Conduct tests on three stainless steel brazed plate heat exchangers consisting of different plate geometries;
    - Low (soft) profile, (inclination angle) β=60°-65°
    - High (hard) profile, (inclination angle) β=30°-35°
    - Medium (mixed) profile, (inclination angle) β=45° or mix of low and high profiles
    - Corrugation pitch, λ=0.25" (6 mm) – 0.6" (15 mm)
    - Corrugation depth, (plate spacing) b=0.08" (2 mm) – 0.16" (4 mm)
    - Plate width, length, and thickness to be selected accordingly
- Test data will be taken on each of the plate configurations described above operating at the following conditions
    - Saturated CO_2 temperature range: 0°F (-17.8°C) to -30°F (-34.4°C)
    - Heat flux range: 800 Btu/hr.ft^2 (2.5 kW/m^2) to 5,000 Btu/hr.ft^2 (15.7 kW/m^2)
    - Inlet condition: superheated gas to saturated vapor
    - Exit condition: saturated liquid to sub-cooled liquid
    - Approach temperature: not to exceed 10°F (5.6°C)
- Data reduction for both single-phase and two-phase heat transfer and pressure drop data will be performed and presented in the form of correlations and charts.

A detailed literature search is presented in Chapter 2. Due to the fact that condensation of carbon dioxide in brazed plate heat exchangers has not been reported to date in open literature, other similar research was reviewed. Studies which involved carbon dioxide as a refrigerant are reported, then several well established single-phase heat transfer and friction factor correlations in plate heat exchangers are compared. Condensation in plate heat exchangers is then reviewed and then a compendium on evaporation in plate heat exchangers is presented.

The facility equipment being used for both single-phase and two-phase experimentation is explained in chapter 3. Details of the geometry of the three different brazed plate heat exchangers are given as well as information on the chiller and CO_2 pump. Specifications and explanations are given for the instrumentation such as RTDs, thermocouples, pressure transducers, and flow meters.

Chapters 4 through 6 discuss the single-phase portion of the study. The single-phase experimentation schematic, setup and test procedure comprise chapter 4. Single-phase analysis procedures including the modified Wilson plot technique and pressure drop equations can be studied in chapter 5. Chapter 6 presents the single-phase results and conclusions of single-phase heat transfer and pressure drop in the three different tested brazed plate heat exchangers. The results compare well with other well established studies and single-phase correlations are stated with an uncertainty analysis and conclusions.

The last chapters, 7 through 9, report the two-phase condensation of carbon dioxide in the tested heat exchangers. Similar to the single-phase chapters, the two-phase schematic, setup and experimental test procedures are discussed in chapter 7. The two-phase data reduction process is detailed in chapter 8, and chapter 9 shows, compares and discusses the two-phase heat transfer and pressure drop data between the different plates. The summary and conclusions chapter, gives a brief overview of the project and its results, and concludes this thesis.

CHAPTER 2: LITERATURE REVIEW

The focus of this research is to understand the condensation behavior of CO_2 in three brazed plate heat exchangers with differing interior plate configurations. To date, no research has been reported in literature on condensing CO_2 in brazed plate heat exchangers. Nevertheless, there has been research on other refrigerants being condensed in brazed plate heat exchangers as well as CO_2 being used as a refrigerant in refrigeration cycles.

2.1 Carbon Dioxide as a Refrigerant

Searching and reviewing the open literature, there is no single work reported on the condensation of CO_2 in brazed plate heat exchangers to date. However, there is research that has been done on carbon dioxide being used in refrigeration systems, as outlined in Table 2.1.

Table 2.1 Carbon dioxide used in refrigeration systems, as reported in open literature

Researcher	**Heat Exchanger Type**	**Remarks**
Robinson and Groll [6]	Single straight tubes with outside fins of constant thickness and spacing	CO_2 and R-22 two-phase behavior was compared and CO_2 heat exchanger dimension ratios were proposed
Pertersen et al. [7]	Small diameter mechanically expanded round-tube heat exchanger and brazed micro-channel type heat exchanger	Discussed advantages and disadvantages of how various exchangers may be used for CO_2 refrigeration cycles in automotive and residential air conditioning
Kim and Kim [8]	Counter flow type heat exchanger with concentric dual tubes using R774/134a and R744/290 mixtures	Experimentation and simulation were performed showing that as mass fractions of R744 increased, cooling capacity and compressor power increased but COP decreased
Rauch et al. [9]	Double pipe heat exchangers	Numerical and experimental results of trans-critical CO_2 cycle discovering optimal gas cooler pressure values in the trans-critical CO_2 cycle
Rigola et al. [10]	Double pipe counter flow	Numerical analysis was performed
Brown et al. [11]	Evaporator and condenser heat exchanger types not specified in simulation program	Visual Basic programs were used to simulate single and two-phase CO_2 vapor compression cycles

As far as research on developing CO_2 as a refrigerant, Hwang et al.[12] explored CO_2 behavior and produced a database to provide a better understanding of the environmentally friendly compound. The researchers utilized fin and tube as well as microchannel heat exchangers to explore CO_2 condensation and evaporation properties. Airside pressure drops were compared according to different air frontal velocities. As inlet pressure of CO_2 increased, its heating capacity did the same up to a pressure of about 10 or 11MPa. Various overall heat transfer coefficients were measured, tabulated, and graphically presented. As air frontal velocities increased, heat transfer values increased. As mass flow rates increased heat transfer values increased as well.

Rigola et al. [13] compared numerically and experimentally a CO_2 transcritical refrigeration system and sub-critical R-134a refrigeration cycle. Although the research was heavily based on numerical analysis, two prototyped single stage hermetic reciprocating compressors (one being an improvement of the other) were used in the CO_2 refrigeration cycle to validate the numerical results. Both numerical and experimental results showed only a 10% lower COP in the CO_2 refrigeration cycle than that of R-134a under similar cooling capacity parameters.

This research that has been done on using CO_2 in the refrigeration cycle, both numerically and experimentally, shows that the compound can be a promising option, but more research is definitely needed to help it move into mainstream HVAC applications.

2.2 Single-phase Flow in Plate Heat Exchangers

To be able to properly study two-phase flow in the plate heat exchangers, comprehensive single-phase flow experimentation is required to ensure that two-phase flow will be valid. Table 2.2 and Table 2.3 show experimental correlations for single-phase heat transfer coefficients and friction factors, respectively, in plate heat exchangers, as presented in Ayub [14].

Table 2.2 Single-phase plate heat exchanger heat transfer correlations using an enlargement factor of unity (ϕ=1)

General Single-Phase Heat Transfer Correlation: $Nu = C_1 \mathrm{Re}^{C_2} \mathrm{Pr}^{C_3} (\mu/\mu_w)^{C_4}$

Kumar [15]

ß	Re	C_1	C_2	C_3	C_4
30	>10	0.348	0.663	0.33	0.17
45	10-100	0.400	0.598	0.33	0.17
60	20-400	0.306	0.529	0.33	0.17

Focke et al. [16]

ß	Re	C_1	C_2	C_3	C_4
30	20-150	1.89	0.46	0.5	0
	150-600	0.57	0.7	0.5	0
	600-16000	1.112	0.6	0.5	0
45	45-300	1.67	0.44	0.5	0
	300-2000	0.405	0.7	0.5	0
	2000-20000	0.84	0.6	0.5	0
60	120-1000	0.77	0.54	0.5	0
	1000-42000	0.44	0.64	0.5	0

Thonon [17]

ß	Re	C_1	C_2	C_3	C_4
30	$50 \le \mathrm{Re} \le 15000$	0.2946	0.700	1/3	0
45	$50 \le \mathrm{Re} \le 15000$	0.2998	0.645	1/3	0
60	$50 \le \mathrm{Re} \le 15000$	0.2267	0.631	1/3	0

Table 2.3 Single-phase plate heat exchanger friction factor correlations using an enlargement factor of unity (ϕ=1)

General Friction Factor Correlations: $f = C_5 \mathrm{Re}^{-C_6} + C_7$

Kumar [15]

ß	Re	C_5	C_6	C_7
30	10-100	19.4	0.589	0
45	15-300	18.29	0.652	0
60	40-400	3.24	0.631	0

Focke et al. [16]

ß	Re	C_5	C_6	C_7
30	90-400 400-16000	188.75 6.7	1.0 0.209	1.2575 0
45	150-1800 1800-30000	91.75 1.46	1.0 0.177	0.3025 0
60	260-3000 3000-50000	57.5 0.8975	1.0 0.263	0.093 0

Thonon [17]

ß	Re	C_5	C_6	C_7
30	≤160 >160	45.57 0.370	0.670 0.172	0 0
45	≤200 >200	18.19 0.6857	0.682 0.172	0 0
60	≤550 >550	26.34 0.572	0.830 0.217	0 0

2.3 Condensation in Plate Heat Exchangers

While heat transfer coefficients and pressure drops have been studied extensively in the single-phase realm in plate heat exchangers as documented by Ayub [14], two-phase vaporization and condensation have not received as much attention, let alone in brazed plate heat exchangers.

A comprehensive condensation table of plate channels has been presented by Würfel and Ostrowski [18]. Various entries of that table, as well as more recent findings, are focused on in the present section of literature review.

Panchal [19] observed condensation heat transfer of ammonia in Alfa-Laval plate heat exchangers. Two exchangers with chevron angles of 60° (high) and 30° (low) were used. Heat transfer was observed using the different parameters of film Reynolds numbers (200-2,000) in the high angle plate and low angle plates. Experimental data was compared against theoretical calculations. The conclusion that was made stated that for both low and high angle plates the heat transfer coefficients increased with the film Reynolds number or remained constant. This behavior was attributed to high interfacial shear stress for laminar-film condensation and the occurrence of the shear-stress-controlled condensation at low Reynolds numbers. From their experimental data though, one can see in Figure 2.1 that the low angle plate heat exchanger has higher heat transfer coefficients than the high angle plate heat exchanger.

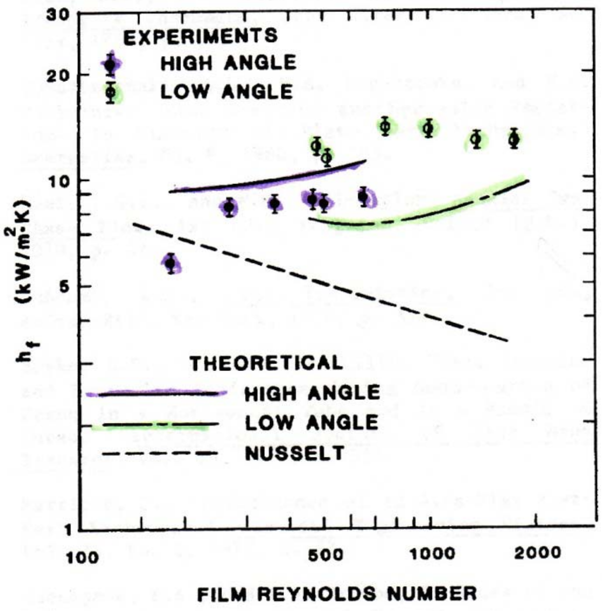

Figure 2.1 Heat-transfer coefficient as a function of film Reynolds number, Panchal [19].

Although no analytical relationship was made from Panchal's [19] experiments, it was compared to Tovazhnyanski's [20] Nusselt numbers for high and low angle plates:

$$Nu = 0.34924Re^{0.75}Pr^{0.4} \quad \text{(high-angle plates)} \tag{2.1}$$

$$Nu = 0.11159Re^{0.75}Pr^{0.4} \quad \text{(low-angle plates)} \tag{2.2}$$

Water-steam condensation was studied by Wang et al. [21] in a plate heat exchanger with a chevron angle of 90 degrees, consisting of 3 channels (2 plates). Parameters measured and were flow, steam content, temperature differences and pressures to obtain heat transfer coefficients. Condensation heat transfer was directly proportional to pressure drop. The heat flux in the plate heat exchanger was consistently larger than shell and tube condensers, this is due in part by the complex configurations of the channels, small cross sections, and shearing of steam flow with high velocities.

Arman and Rabas [22] reported their results using ammonia in their plate heat exchangers with chevron angles of 30° and 60° to test single component condensation correlation equations. A propane/butane mixture was used in a plate heat exchanger (angle not specified) to study binary-component condensation as well. The single component condensation results revealed that the high chevron angle achieved high pressure drops at Reynolds numbers (5000-7500), where the low angle plate achieved the same pressure drop at almost 3 times the Reynolds numbers. Also, from the tables in the paper, it appeared that the high angle chevron plate required a lower mass flow rate than the low angle chevron plate to achieve the same heat transfer coefficients.

Yan et al. [23] found that the condensation trends for R-134a in plate heat exchangers were that the higher the vapor quality, the greater the heat transfer coefficient as well as pressure drop. Their experimental parameters included mass flux, average imposed heat flux, saturated pressure, and vapor quality. Using an inclination angle of 60° in the 500mm by 120mm plates, it was noted that the chevron configuration in plate heat exchanger create high turbulence at low Reynolds numbers which increased heat transfer at slower flow rates. The following heat transfer coefficient and friction factor were correlated:

$$Nu = 4.118{Re_{eq}}^{0.4}{Pr_l}^{1/3} \tag{2.3}$$

$$f_{tp}Re^{0.4}Bo^{-0.5}\left({}^{p_m}/_{P_c}\right)^{-0.8} = 94.75{Re_{eq}}^{-0.0467} \tag{2.4}$$

Würfel and Ostrowski [18] used chevron angles from 30 degrees to 60 degrees with plate spacing/amplitude of corrugation of 2.5-7.4 mm. Reynolds numbers of 80 – 2000 were measured during the experimentation. Measuring the drag in the plate concluded that an increase in the inclination angle of the plates increased the drag as well as the heat transfer. In fact, the researchers claimed an increase of 3-4 times the heat transfer coefficient as inclination angles increased from 30 to 60 degrees. The proposed heat transfer condensation correlation was

$$Nu_{CO} = CRe_{hyd}^{m}Pr_l^{0.33} \tag{2.5}$$

and the pressure drop

$$\Delta p_{CO,F} = F\left(\left(\frac{(1-x)}{x}\right)^{0.9}\left(\frac{\rho_V}{\rho_l}\right)^{0.5}\left(\frac{\eta_l}{\eta_V}\right)^{0.1}\right)^{-2}\left(\frac{(\bar{\dot{m}}_l^2 L\xi)}{2\rho_l d_{hyd}}\right) \tag{2.6}$$

Jokar et al [24] explored single and two-phase heat transfer and pressure drop correlations of R-134a that were found in three heat exchanger depths (34, 40, and 54 plates) of 112mm by 311mm plates all having a corrugation inclination angles of 60°. These heat exchangers were used as both evaporators as well as condensers in the standard compression refrigeration cycle. The two-phase flow correlations proved to be much more complex than that of the single-phase. The following relations were proposed for the two-phase condensation heat transfer and pressure drop:

$$\begin{aligned} &Nu_{tp} \\ &= 3.371Re_l^{0.55}Pr_l^{0.3}\left(G^2/\rho_l^2C_{p,l}\Delta T\right)^{1.3}\left(\rho_l^2{i'}_{fg}/G^2\right)^{1.05}(\rho_l\sigma/\mu_lG)^{0.05}(\rho_l/(\rho_l-\rho_v))^2 \end{aligned} \tag{2.7}$$

$$C_{f,tp} = 2.139 * 10^7 \left(\frac{GD_H}{\mu_{m,sat}}\right)^{-1.6} \quad \text{for} \quad 960 \leq \left(\frac{GD_H}{\mu_{m,sat}}\right) \leq 4160 \tag{2.8}$$

Important two-phase behaviors were observed in the experimentation of condensation in the brazed plate heat exchangers. For example, when the temperature differences were not large, film condensation proved to be the dominant characteristic when determining heat transfer correlations. Also, as the mass flow rates increased within the minichannels of the brazed plate heat exchangers, convection proved to be more important in driving heat to transfer.

Longo and Gasparella [25] studied the condensation of R-134a in a brazed plate heat exchanger. Three parameters were observed to conclude how each affected the heat transfer coefficients and pressure drop in the exchanger; mass flux, saturated R-134a vapor, and superheated R-134a vapor. The brazed plate heat exchanger used consisted of 10 plates, 72mm by 310mm that had the inclination chevron angle of 65°. It appeared that gravity controlled condensation occurred at mass fluxes less than 20kg/m^{2}s, but when the flux exceeded this, forced convection condensation was achieved, producing a 30% increased heat transfer coefficient when the mass flux was 40kg/m^{2}s. The behavior of the saturated vapor versus the superheat was similar, with the superheat yielding only an 8-10% increase in heat transfer over the saturate. Saturation temperature however played no great significance in heat transfer in the brazed plate heat exchanger. For saturated vapor condensation Longo and Gasparella [25] proposed the average heat transfer coefficient on the vertical plate as

$$h_r = \Phi 0.943\left[\left({\lambda_L}^3 {\rho_l}^2 g \Delta J_{LG}\right)/\left(\mu_l \Delta T L\right)\right]^{\frac{1}{4}} \tag{2.9}$$

where Φ is the enlargement factor equal to the ratio between the actual area and the projected area of the plates due to corrugation. For forced convection condensation the average heat transfer coefficient was found to be modeled closely to

$$h_r = (1/S)\int_0^S \Phi 5.03(\lambda_L/d_h) Re_{eq}^{\frac{1}{3}} Pr_L^{\frac{1}{3}} dS \tag{2.10}$$

for equivalent Reynolds numbers less than 50,000. Pressure drop was derived from the experimental data as

$$\Delta p_f = 1.816KE/V \tag{2.11}$$

Longo et al. [26] also researched the correlations between surface smoothness within plate heat exchangers and condensation and evaporation heat transfer coefficients. Three types of smoothness were observed; smooth, rough, and cross-grooved. The plates were all of the chevron or herringbone type with inclination angles of 65°. It was concluded that the increased roughness was only advantageous in vaporization, whereas the cross-grooved plates improved both vaporization and condensation by 30%-40% and 60% respectively when compared to smooth plates.

Many condensation correlations were given by the different literatures reviewed, but all the studies shared similar behavioral trends. Regardless of the refrigerant type, in the studies that compared inclination angles, higher heat transfer rates were achieved by the plates which consisted of steeper inclination angles. Of all the studies, common influential condensation variables included mass flux, saturation quality, temperature differences, and pressure drops across the plates.

2.4 Evaporation in Plate Heat Exchangers

Evaporation is another field of two-phase flow that is important, but not focused on in this study. Table 2.4 tracks some of the research that has been conducted on vaporization in plate heat exchangers.

Table 2.4 Vaporization research in plate heat exchangers

Researchers	**Refrigerant**	**Dominating Experimental Factors**
Kedzierski [27]	HCFC-22	Tilting angle from intended vertical position
Yan et al. [28]	R-134a	Mean vapor quality, mass and heat flux
Hsieh and Lin [29]	HFC-410A	Mean vapor quality, mass and heat flux, saturation pressure
Ayub [14]	Ammonia and R-22	Although Ayub did not focus solely on BPHEs, he did formulate a universal equation for heat transfer during evaporation in PHEs corresponding to chevron angle.
Han et al. [30]	HFC-410A	Mass and heat flux, saturation temperature, chevron angles
Claesson [31]	HFC-134a	Inlet quality, pressure, mass flux
Jokar et al. [24]	HFC-134a	Heat and mass flux, chevron angles
Sterner [32]	Ammonia	Inlet flow and temperature
Longo and Gasperlla [25]	R-236fa, R-134, R-410A	Heat flux, refrigerant mass flux, saturation temperature, outlet conditions/fluid properties

The present thesis will explore the heat transfer correlations and pressure drops of CO_2 condensing in three brazed plate heat exchangers having inclination angles of 30°, 60° and a mix of the two inclination angles.

CHAPTER 3: TEST FACILITY

Equipment was selected, purchased, installed, and used in the thermo/fluids laboratory at Washington State University Vancouver to conduct both single-phase and two-phase experimentation. Schematics of the single-phase and two-phase loops are presented in Figures 3.1 and 3.2, respectively. Each loop is described and discussed in the following chapters, while details of major components are given in this chapter. Information sheets (where available from companies) on the selected equipment can be found in Appendix B.

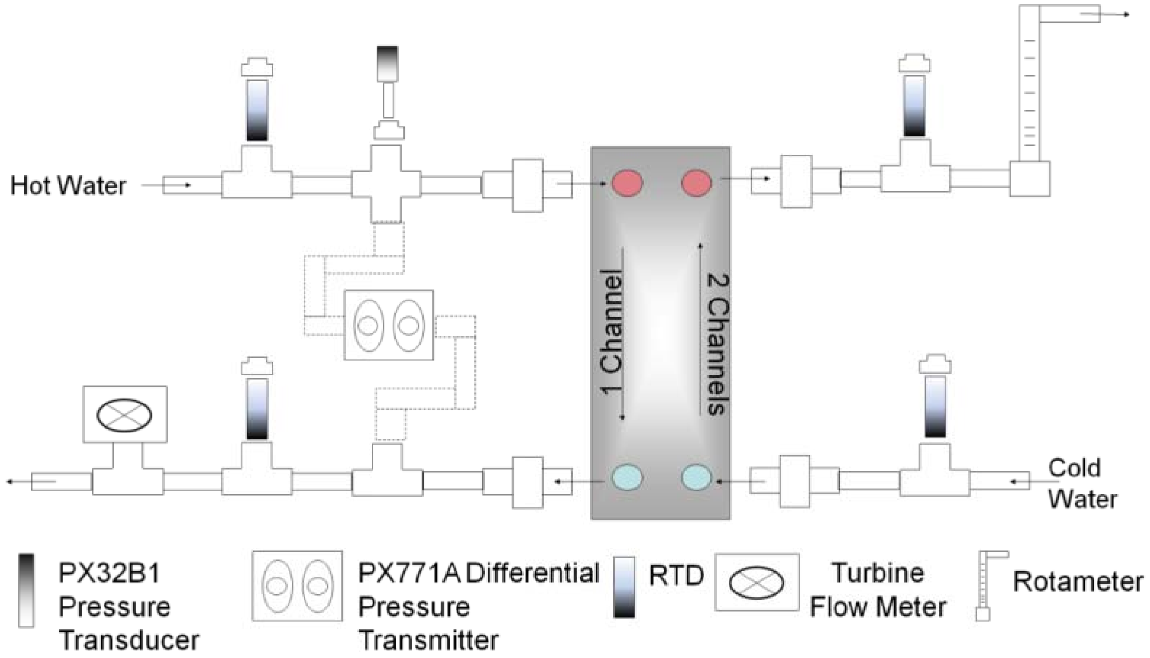

Figure 3.1 Single-phase schematic.

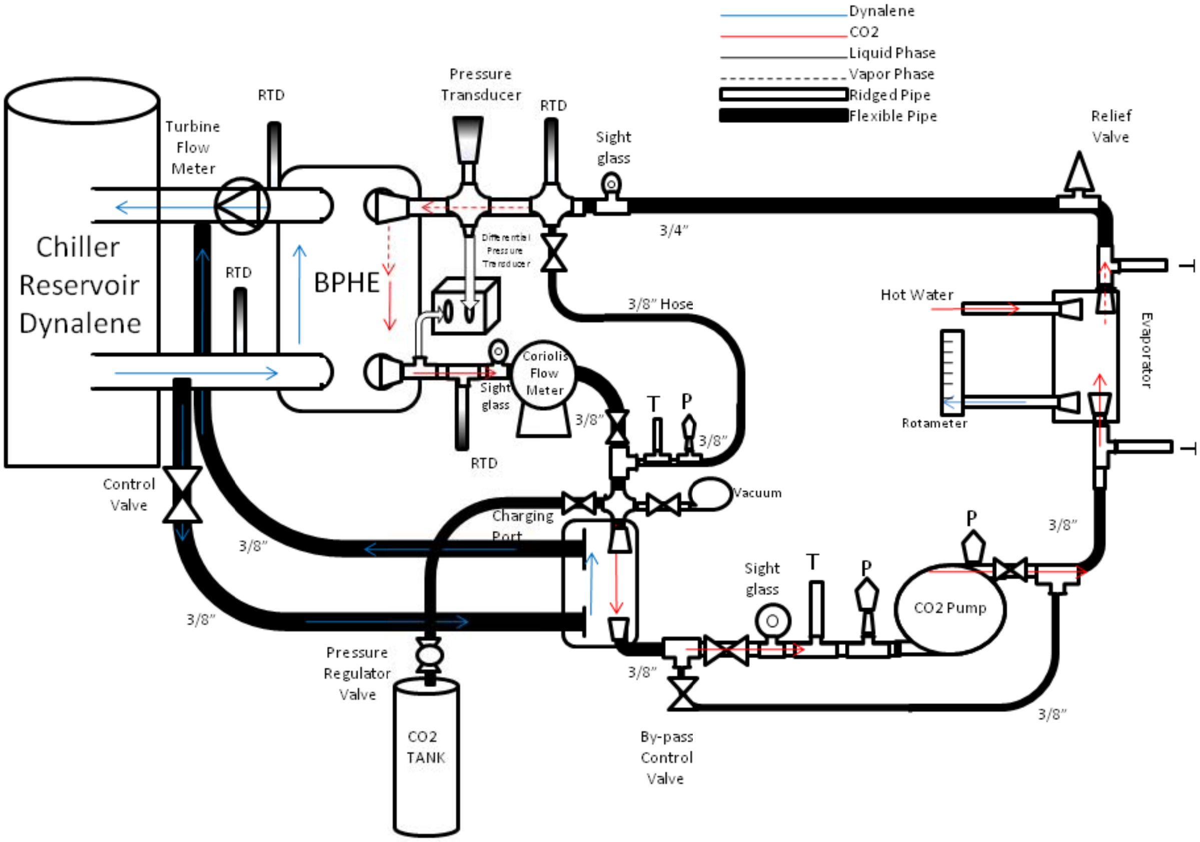

Figure 3.2 Two-phase schematic.

3.1 Brazed Plate Heat Exchangers

The present study is sponsored in part by a manufacturer of brazed plate heat exchangers, and as such, produced specific heat exchangers for this study. The company desired to know how their exchangers would perform condensing CO_2. The exchangers, as typically shown in Figure 3.3, have similar outside dimensions but contain different inner plate geometries, consisting of different chevron angle profiles. Each plate within an exchanger is formed with a corrugated angle. Two plates in contact one with another, create a channel through which a fluid flows, and the inclination angles of two neighboring plates are oriented in opposing directions. Three exchangers consisting of high, low and a mix of high and low angle profiled plates will be studied to find pressure drop and heat transfer correlations. The brazed plate heat exchangers used in this study are 5” by 21” consisting of 3 channels. Counter flow, detailed in Figure 3.4, is a flow pattern that requires neighboring channels to have fluids flow in opposing directions. This counter flow method, coupled with alternating inclination angle corrugated plates (effectively creating a high roughness for a passing fluid), allows for high heat transfer rates and an increase in pressure drop across the plates. Figure 3.4 and Table 3.1 define the dimensions and give measurements of the three different exchangers being tested in the present study; low profile (60°/60° channels), high profile (27°/27° channels) and mixed profile (60°/27° channels).

Figure 3.3 Typical brazed plate heat exchanger.

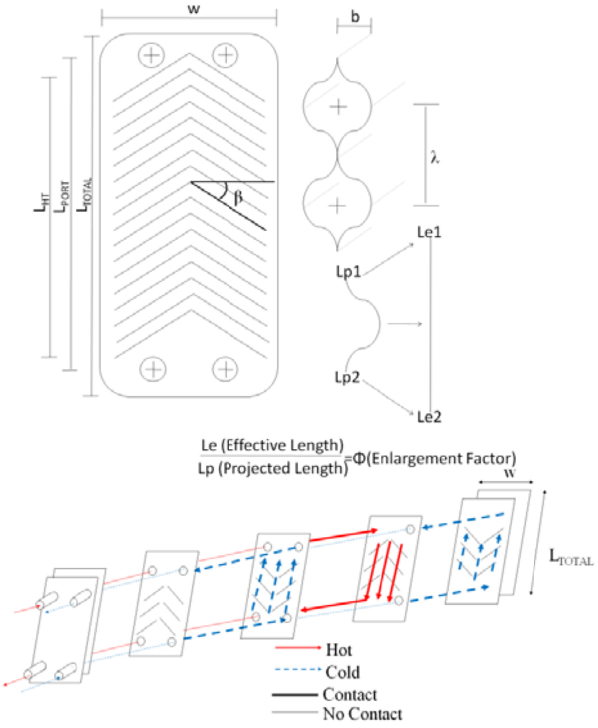

Figure 3.4 BPHE measurement definitions and flow characteristics.

Table 3.1 BPHE low, mixed and high profile geometric measurements

	L Plate	M Plate	H Plate
Chevron Angle, degrees (measured from horizontal in a vertical instillation) [β]	60°/60°	27°/60°	27°/27°
Length $_{\text{Total}}$, mm/in. [L_{Total}]	533.4/21	533.4/21	533.4/21
Length $_{\text{Heat Transfer}}$ (Top of Bottom Port to Bottom of Top Port), mm/in. [L_{HT}]	444.5/17.5	444.5/17.5	444.5/17.5
Length $_{\text{Pressure Drop}}$ (Middle of Top Port to Middle of Bottom Port), mm/in [L_{Port}]	476.25/18.75	476.25/18.75	476.25/18.75
Width, mm/in. [w]	127/5	127/5	127/5
Port Diameter, mm/in.	25.4/1	25.4/1	25.4/1
Corrugation Pitch, mm /in. [λ]	6.27/0.2468	6.19/0.2437	6.03/0.2374
Enlargement Factor [Φ]	1.2	1.2	1.2
Projected Surface Area, m^2/$in.^2$	0.05645/87.5	0.05645/87.5	0.05645/87.5
Effective Surface Area, m^2 /$in.^2$ [A_s]	0.06774/105	0.06774/105	0.06774/105
Plate Thickness, mm /in. [t]	0.4/0.0157	0.4/0.0157	0.4/0.0157
Mean Channel Spacing, mm /in. [b]	2/0.0787	2/0.0787	2/0.0787
Number of Channels	3	3	3

3.2 Chiller

A packaged water-cooled chiller was selected from Chiller Solutions LLC, purchased, and installed in the thermal/fluid laboratory where the facility is set up. The chiller, as shown in Figure 3.5, is rated at a 39,275 BTUH (3.3 Tons) capacity @ -40°C and uses R507a as the working fluid to chill the secondary cooling fluid dynalene (HC-50). A chiller designed to work with dynalene was found to be necessary for this project rather than a chiller using ethylene glycol since dynalene is less viscous at very low temperatures. Furthermore, a 50/50 ethylene glycol water mixture may freeze at -37°C. Table 3.2 shows some of the thermo-physical properties of the two cooling fluids at -35°C. Although dynalene is 25% more dense and its specific heat value is 20% less than glycol, it is 75% less viscous than the ethylene glycol mixture.

Table 3.2 Thermal fluid property comparison

-35°C	Density (kg/m^3)	Specific Heat (kJ/kg*K)	Dynamic Viscosity (cP)	Freezing Point (°C)
dynalene (HC50)	1370.5	2.59	15.7	-55
50/50 ethylene glycol	1089.94	3.07	66.93	-37

Figure 3.5 Packaged water-cooled chiller.

The chiller uses a 75 gallon stainless steel tank insulated with 3” expanded foam in a 0.080” aluminum jacket to store and maintain the dynalene at desired temperatures. The chiller uses a water-cooled condenser that, depending on the load conditions, needs different flow rates of cooling water. At the peak load of the compressor, the condenser uses tap water flowing at a rate of 10-15 gpm at about 65°F, e.g., to cool the dynalene from room temperature to about 0°F at start up. After passing the peak point, the tap water line is replaced with a chilled water line, supplied by the university facilities plant, flowing at a rate of 5-8 gpm at about 50°F to operate the chiller system efficiently.

3.3 CO_2 Pump

In order to study the condensation of carbon dioxide, a CO_2 refrigeration loop must be built. The specifications for the test conditions state that the temperature range of saturated CO_2 should be from 0°F (-17.8°C) to -30°F (-34.4°C) and the heat flux in the heat exchanger spans 800 Btu/hr-ft^2 (2.5 kW/m^2) to 5,000 Btu/hr-ft^2 (15.7 kW/m^2). Not knowing initially the size of plates being used for the heat exchanger, maximum and minimum flow rates and pressures were calculated from the possible plate geometries to size the CO_2 pump. By multiplying the given fluxes (kJ/sm^2) by the approximate possible plate geometry areas (m^2), minimum and maximum loads were found (kJ/s). These loads were then divided by the latent heat of vaporization (kJ/kg) of CO_2 at the low and high temperatures to yield a mass flow rate (kg/s). The mass flow was then converted to a volumetric flow based on appropriate properties of CO_2. The flow range that was calculated was on the order of 0.01 gpm for the smallest plate and lowest heat flux, while for the largest plates and highest heat flux, 0.4 gpm. When researching companies to find a suitable CO_2 pump, information on safety pressure levels was acquired. Knowing at what pressures CO_2 changes phase at given temperatures is not enough, pumps need to work well into the liquid state in order to ensure longevity which requires higher pressures, approximately 150-200 psi higher than saturation pressures. Due to the lack of demand for small load CO_2 refrigeration loops, finding a pump that would operate at low temperatures (down to -40°C) pumping extremely low amounts of CO_2 (0.01 to 0.4 gpm) at safe pressures proved to be laborious. A sturdy CO_2 pump that has the capability of withstanding extreme low temperatures and extreme low flow rates was purchased to facilitate the need. Giant Industries provided such a pump, as shown in Figure 3.6.

Figure 3.6 GIANTPUMP liquid CO_2 pump.

The pump offered the possibility of working with CO_2 at low temperatures down to -40°C and achieving the low flow rates required by the project. The CP230 is rated at 0.5 gpm at 2000 psi at 750 rpm. But with the variable frequency drive, which was purchased and integrated with the pump, it should be able to move CO_2 from low rates ranging from 0.1 to 0.5 gpm with inlet pressures of 300 to 500 psi. If the flow rates that are required go below the 0.1 gpm then a by pass line should be constructed to achieve the proper flow.

3.4 Temperature Reading Devices

Resistance Temperature Detectors (RTD): Temperature must be measured accurately at the inlets and outlets of the plate heat exchangers, and as such, RTDs provided the accuracy needed to deliver reliable temperature readings. Just as with thermocouples, there are several kinds of RTDs that are configured differently and have different accuracies. Of the three different wire configurations (2-wire, 3-wire, 4-wire) that are available, the 4-wire RTD were used in the test set up, as shown in Figure 3.7. The 4-wire design touts the highest accuracy and reliability of the different configurations because the resistance error due to lead wire resistance is nonexistent in this design.

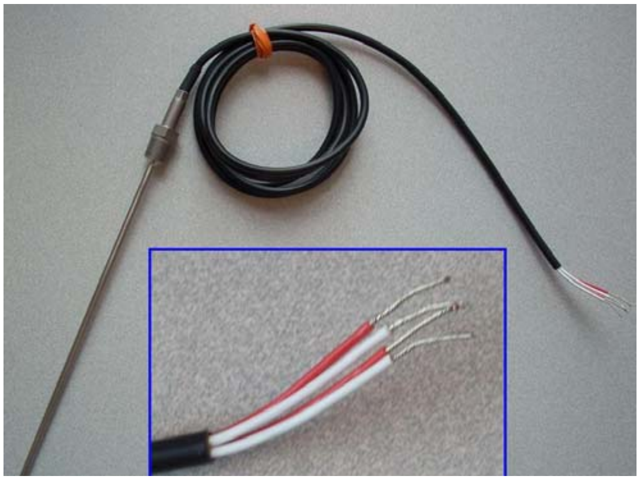

Figure 3.7 6” RTD with 4-wire configuration.

There are five different tolerance classes that depict temperature accuracy; Class B, Class A, DIN (Deutsches Institute fur Normung or German Institute for Standardization) 1/3, DIN 1/5, and DIN 1/10. Table 3.3 shows comparison of four of the temperature reporting tolerances for RTDs.

Table 3.3 Temperature tolerances for RTDs

Temp (°C)	Class B (±°C)	Class A (±°C)	1/3 DIN (±°C)	1/10 DIN (±°C)
-40	0.50	0.25	0.13	0.050
-30	0.45	0.23	0.13	0.045
-20	0.40	0.20	0.12	0.040
-10	0.35	0.18	0.11	0.035

The RTDs in this experiment are of the 4-wire configuration with an accuracy following the 1/3 DIN. There are also several different curves that RTDs can be calibrated to, of those, the 100 Ω platinum RTDs used will conform to the Pt 3851 curve. Each of the RTDs have stem lengths of 6" to minimize stem conduction effects. This measurement surpasses the recommended minimum stem length of 20 times the RTD diameter, and with the diameter of 1/8", the 6" sheath is 48 times the diameter, so temperature reading disturbances from ambient temperatures will not influence experimental data.

Thermocouples: For areas of the condensing loop that do not require as high of accuracy temperature readings, type T thermocouples will suffice. The temperature range of type T thermocouples is adequate for the present experimentation parameters. The thermocouples, as shown in Figure3.8, are classified in tolerance class 1, which for type T is ±0.5°C between -40°C to 125°C. This accuracy is actually 3 times better than the more common K and J type thermocouples, which are rated at ±1.5°C between -40°C to 375°C. Again the stem lengths are 6" as to minimize stem conduction interference.

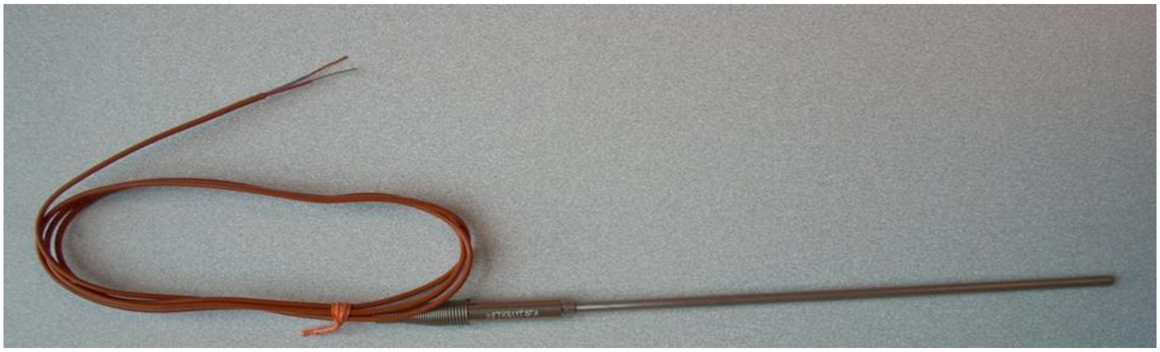

Figure 3.8 Type T thermocouple.

3.5 Pressure Transducers

Obtaining accurate pressure drop is critical in the project, and as such, high accuracy gauge and differential pressure transducers will be utilized to measure pressure behaviors. For the gauge pressure transducer, the PX32B1 from OMEGADYNE Inc. is installed in the experimental apparatus, as shown in Figure 3.9.

Figure 3.9 PX32B1 pressure transducer.

This specific pressure transducer will serve well considering the fact that it is one of the few pressure transducers to have a compensated temperature range of -40° to +168°C. It is made of all stainless steel and hermetically sealed. It requires a 10V ac or dc excitation voltage and returns a 3mV/V ±1% and has an accuracy of 0.25% linearity, with hysteresis and repeatability combined. The pressure transducer is designed to work in a range of 0-500 psi. To measure the pressure drop across the plate heat exchangers, the PX771A differential pressure transmitter will be used. This devise, as shown in Figure 3.10, is made of all stainless steel wetted parts as well and can operate up to 2000 psi and has a processes operating temperature of -40° to 104°C. The transmitter works off of an excitation voltage ranging from 6-42 Vdc and outputs either a 4-20 mA or 1-5 Vdc signal. The PX771A has an accuracy of ±0.1% of the upper range limit or ±0.15% of full scale.

Figure 3.10 Differential pressure transmitter.

3.6 Turbine Flow Meter (Dynalene)

To accurately meter the flow of dynalene which will ultimately condense the CO_2 refrigerant, the FT-10 flow meter from Flow Technology was used. The meter, as shown in Figure 3.11, was a turbine flow meter made of stainless steel using a ceramic journal bearing with a RF (radio frequency) pickoff signal to ensure the widest flow metering range of 0.3 to 15 gpm. The ceramic journal bearing is necessary for the dynalene due to its high viscosity. The flow meter has a 10 point calibration in water to ensure a reading accuracy of ±0.05%. The FT-10 had temperature and pressure operating ranges of -100° to 800°F and up to 5000 psig. The flow meter required an input DC voltage range of 8 to 30V and produced 0 to 5V pulses ranging from 5 to 5000 Hz.

Figure 3.11 Flow meter to measure dynalene flow.

3.7 Coriolis Flow Meter (CO_2 Flow Meter)

To accurately measure the low flow rates of the low temperature and high pressure CO_2, a coriolis flow meter was selected. Micro Motion, Inc. was the manufacturer of the specific coriolis flow meter used for this experimentation set up. The flow meter measuring ranges from 0.002267 kg/sec up to 0.02267 kg/sec maintaining an uncertainty of ±0.100%. The CO_2 flow required by the project ranges from 0.001 kg/sec to 0.01 kg/sec. The lower flow rates will exhibit a higher uncertainty, but the majority of the data points will be within a confident flow measuring range. The flow meter can withstand pressures up to 1812 psig with the safety housing being able to withstand 425 psig. Operation temperatures range from -240° to 204°C. Figures 3.12 and 3.13 show the coriolis flow meter and its transmitter.

Figure 3.12 Coriolis flow meter.

Figure 3.13 Coriolis flow meter with transmitter.

3.8 Uncertainty Analysis

The instrumentation used in the experimental process detected and recorded temperatures, pressures, and flow rates. The uncertainties for the instrumentation are presented in Table 3.4.

Table 3.4 Uncertainty of data collecting devices

Parameter	Instrument (Range of measurement in tests)	Measurement Uncertainty
Temperature	RTD 4-wire DIN 1/3 (10° to 50°C)	±0.16°C
Pressure	Gauge Transducer (< 50 psi)	±0.1 psi
Differential Pressure	Differential Transmitter (<40 psi)	±0.1 psi
Flow	In-Line Turbine Type (0.3-15 gpm)	±0.1 gpm
	Coriolis Mass Flow (0.002267- 0.02267kg/s)	±0.1 % flow

CHAPTER 4: SINGLE-PHASE EXPERIMENTATION

A thorough single-phase analysis, including water/water and dynalene/water, was conducted since single-phase heat transfer and pressure drop coefficients are needed in the mathematics of the two-phase analysis of CO_2 condensation.

4.1 Single-Phase Loop Setup

To mimic the two-phase flow behavior of CO_2 condensing (rejecting heat) in the middle of three channels within the heat exchanger, single-phase hot water entered the top of the exchanger, flowing through the middle channel. On the other side, cold water entered from the bottom of the exchanger, flowing through the side channels, to produce counter flow heat transfer. The hot water line contained the instrumentation to record temperature, pressure drop, and flow rate; however, the cold water line recorded only temperature and flow rate. The reason no pressure measuring devises were used on the cold side was because only hot side coefficients were needed from the water/water experimentation to be used in CO_2 two-phase mathematics. To most accurately observe the pressure drop across the plates, the pressure transducers on the hot line were positioned as close as possible to the inlet and outlet of the exchanger, followed by temperature reading and flow metering devices. The schematic of the single-phase test facility is depicted in Figure 4.1.

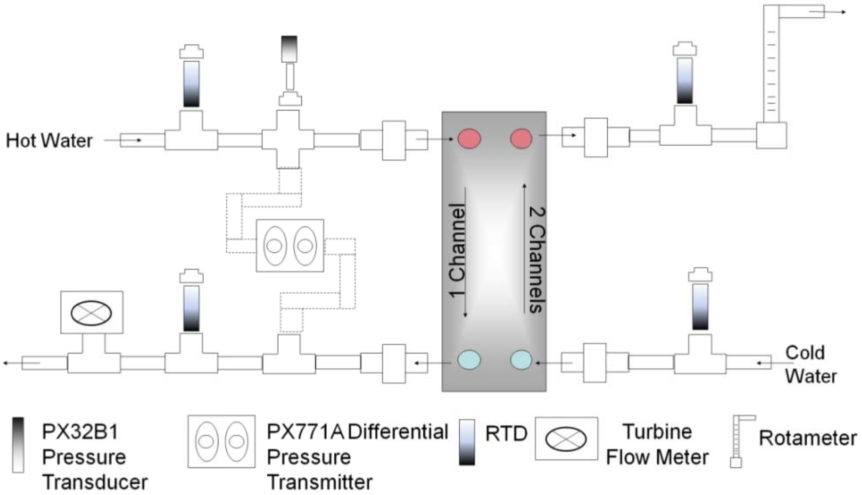

Figure 4.1 Single-phase experimental schematic.

In order to obtain reliable data for the full range of flows, it was important to make sure that both hot and cold water completely filled the lines to avoid air-water mixture flow (part water part air). To achieve this, nozzles were placed at the end of each line to ensure that the lines were free of air.

For the dynalene/water experimentation, the single-phase flow configuration was similar, i.e., hot water flowing through the middle channel and chilled dynalene flowing through the side channels. But the instrumentation used for the hot side in the water/water configuration (temperature, pressure drop, flow rate) was switched to record data for the cold side in the dynalene/water test, in order to obtain more precise measurements on the dynalene side. It is this single-phase dyanlene data which would render cold side coefficients that would be used later in the CO_2 two-phase mathematics.

The tested brazed plate heat exchanger is housed vertically in an insulated box for all single-phase and two-phase data collection. The back of the box contains 5” of R-4 insulation and the front of the plate was covered with 4” of R-4 insulation, giving 20 and 16 hr.ft^2.°F/BTU respectively for each side. Figure 4.2 shows the brazed plate heat exchanger in the insulation box with and without the front insulation installed.

Figure 4.2 Condensor housing box with and without front insulation.

All the tubing for both single-phase and two-phase experimentation was also insulated to reduce heat absorption to the CO_2 and dynalene. Although it is impossible to create a fully adiabatic system, the precaustions taken minimized the amount of heat loss to surroundings. Calculating the total heat loss throughout the entire system is impractical, but estimated to be no larger than 0.5%.

4.2 Data Acquisition

All of the data acquisition equipment was integrated into a National Instruments SC2345 Signal Conditioning Connector Block which transmitted signals to the DAQ National Instruments USB-6251 16 input, 16-bit, 1.25MS/s multifunction I/O with Correlated Digital I/O for USB by which a Labview 7.2 program was written to record and display all the temperatures, pressures, and flow rates necessary. Each data acquisition device used a specific National Instruments module in the SC2345, details of which are shown in Table 4.1. A Tektronix PS2520G power supply was used to power the flow meter as well as the differential pressure transmitter. Figure 4.3 shows the front panel of the LabView program as it took real time data.

Table 4.1 DAQ instrumentation

Device	Module	Measurement Mode	Power Supply
RTD	SCC RTD01	Wheatstone Bridge Resistance	n/a
Differential Pressure	SCC CI20	Current Input	24V @ 1A
Gauge Pressure	SCC SG24	10v Excitation Full Bridge Strain Gauge	n/a
Flow Meter	SCC FT01	Feed Through Component (Frequency)	10V @ 10ma

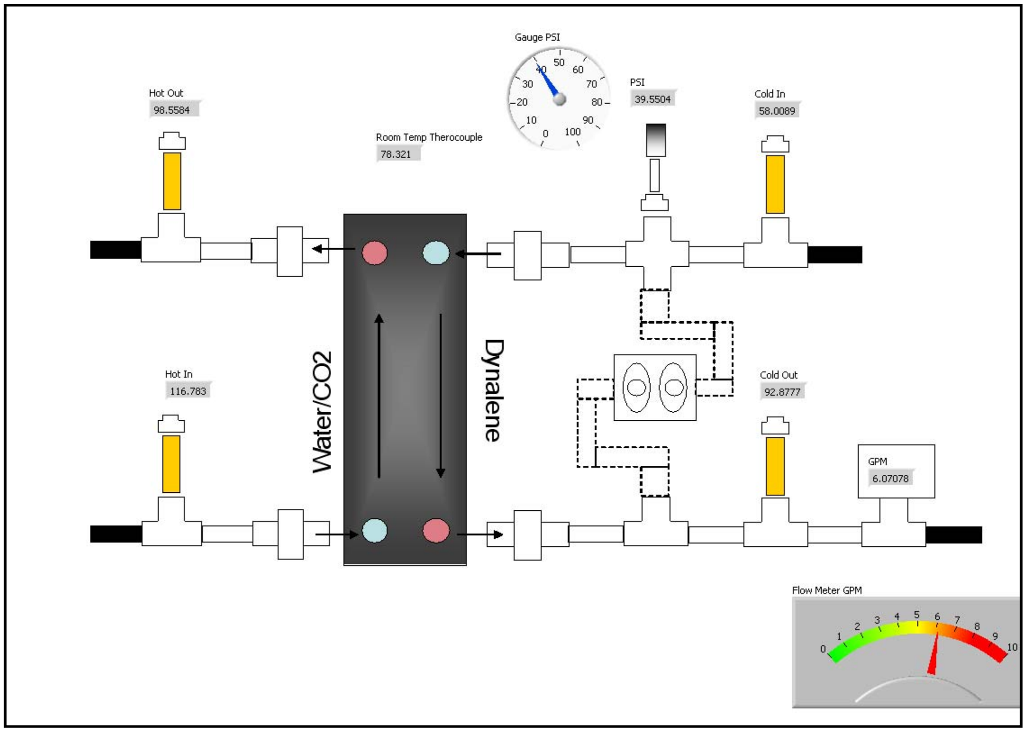

Hot Out 98.5584

Room Temp Therocouple 78.321

PSI 39.5504

Cold In 58.0089

Hot In 116.783

Cold Out 92.8777

GPM 6.07078

Figure 4.3 DAQ program monitoring and collecting single-phase data.

4.3 Experimental Test Procedure

To be as consistent as possible in the data collection process, identical steps were used for each heat exchanger.

1. Both hot and cold water ran until maximum hot and minimum cold temperatures were achieved.
2. Data collecting began by finding the maximum flow rates permitted by each side of each plate (1 channel side and 2 channel side) and assigning flow increments to be analyzed.
3. The DAQ recorded the inlet and outlet temperatures, gauge and differential pressures, as well as the flow from the turbine flow meter every 2 seconds for a duration of 2 minutes yielding a total of 60 data points per data collection set.
4. Data collection sets started by recording maximum flows of cold fluids and hot water. The hot flow stayed constant as the cold flow decreased for each iteration. When the

minimum cold flow iteration was completed, the next permeation of reduced hot flow was set constant and the cold flow increased for each iteration. Data collection followed this fashion until all combinations of low and high flows for cold and hot water were recorded.

5. Statistical analysis was performed on each data set before moving to the next data set to ensure low standard deviations and acceptable precision intervals.

Data was then verified by the energy balance equation, assuming the specific heats of the hot and cold water to be equal. The ratio of cold mass flow rate with cold side temperature difference and hot mass flow rate with hot side temperature difference should equal unity.

CHAPTER 5: SINGLE-PHASE ANALYSIS

The raw data collected by the data acquisition system are used to obtain the single-phase heat transfer and pressure correlations within the three brazed plate heat exchangers. This section reviews the data reduction method, and discusses the resulted correlations.

5.1 Modified Wilson Plot Technique (Heat Transfer)

As the first step in analyzing the collected data, properties of water for each test point were calculated at bulk temperatures averaged between the inlet and outlet ports on each side.

Each property, including density, specific heat, conductivity, and viscosity, was evaluated and correlated, using third order logarithmic regressions. These properties were then used to find the flow characteristics in the channels for each plate.

The Reynolds number of the flow within the channels was calculated by:

$$\mathrm{Re} = \frac{G D_{hyd}}{\mu} \tag{5.1}$$

where the hydraulic diameter was defined as two times the average plate spacing (D_{hyd}=2b), and the mass flux was calculated based on the minimum free flow area (A_o) between the plates, as described by Shah and Wanniarachchi (1992):

$$G = \frac{\rho \dot{V}}{A_o} \tag{5.2}$$

Due to the complicated geometries that brazed plate heat exchangers contain, this minimum free flow area is difficult to estimate and has not been universally standardized. However for the sake of simplicity, many studies have considered this free flow area as the average plate spacing, *b*, multiplied by the width of the plate:

$$A_o \approx bw \tag{5.3}$$

It is notable that the *minimum* free flow area (MFFA) between the two neighboring plates, which depends on the corrugation angle, are much less than the area given by Equation 5.3. A more thorough description of the minimum free flow area is given in the appendix, while Equation 5.3 is used for data reduction in this study.

An energy balance was applied in order to obtain heat transfer rates on both hot and cold sides:

$$Q = \dot{m} c_p \Delta T \tag{5.4}$$

Using the log-mean temperature difference

$$\Delta T_{lm} = \frac{\left[\left(T_{h,i} - T_{c,o}\right) - \left(T_{h,o} - T_{c,i}\right)\right]}{\ln\left[\left(T_{h,i} - T_{c,o}\right) / \left(T_{h,o} - T_{c,i}\right)\right]} \tag{5.5}$$

the overall heat transfer coefficient in the heat exchanger was calculated by:

$$U = \frac{Q_h}{2 A_s \Delta T_{lm}} \tag{5.6}$$

where A_s is the effective heat transfer surface area, which was calculated by the projected heat transfer area multiplied by the enlargement factor (effective length divided by projected length, refer to Figure 3.4).

A common analysis method of single-phase heat transfer in brazed plate heat exchangers is the modified Wilson plot technique. Due to the possibility of large property variations, especially the viscosity of dynalene, the heat transfer correlation format was chosen similar to the Sieder-Tate equation, as explained in Incropera and DeWitt [33]:

$$Nu = C \operatorname{Re}^{P} \operatorname{Pr}^{1/3} \left(\mu / \mu_s\right)^{0.14} \tag{5.7}$$

The heat transfer coefficients for the hot and cold sides of the brazed plate heat exchanger are thus obtained by:

$$h_c = (k_c / D_{hyd}) C_c \operatorname{Re}_c{}^P \operatorname{Pr}_c{}^{1/3} (\mu / \mu_s)_c^{0.14} \tag{5.8}$$

and

$$h_h = (k_h / D_{hyd}) C_h \operatorname{Re}_h{}^P \operatorname{Pr}_h{}^{1/3} (\mu / \mu_s)_h^{0.14} \tag{5.9}$$

In the original Wilson plot technique, used for shell-and-tube heat exchangers, C_h and C_c are the only coefficients that need to be found to be able to find Nusselt numbers. Reynolds number exponent (0.8), Prandtl number exponent (1/3), as well as the viscosity ratio exponent (0.14) for the tube side is assumed constant due to the widely accepted characteristics of in tube flow. The shell side Reynolds number exponent, however, is not necessarily 0.8 and can be optimized, based on the magnitude of Reynolds number, in the Wilson plot calculations. Plate geometries in brazed plate heat exchangers are so complex and varied among different manufacturers, the flow regimes (and as a result, the Reynolds number exponents) cannot be assumed like the in-tube flow. Due to the similarity in geometries and configurations on the cold and hot channels of a brazed plate heat exchanger, the flow regimes and the Reynolds number exponents on both sides can be assumed identical at any given Reynolds number. This flow assumption is safe even for very different fluids flowing in the exchanger because the fluid properties are taken into account with the Prandtl number and the viscosity ratio portions of the mathematical relations. Prandtl number exponent and viscosity ratio exponents, which account for the different fluid properties of water and dynalene, can also be assumed constant at 1/3 and 0.14, respectively. The original Wilson plot technique requires the data to be recorded at constant flow rates and constant average bulk fluid temperatures on both hot and cold sides, which is not easily accomplished. However, the modified Wilson plot technique, devised by

Briggs and Young [34], allows data to be taken at varying flow rates and varying bulk fluid temperatures on hot and cold sides. The overall heat transfer equation based on this method is obtained through the following thermal resistance equation:

$$\frac{1}{U}-\left(\frac{t}{k}\right)_{wall}=\frac{1}{C_c\frac{k_c}{D_{hyd}}\left(\frac{D_{hyd}G}{\mu}\right)_c^P\left(\frac{c_p\mu}{k}\right)_c^{1/3}\left(\frac{\mu}{\mu_s}\right)_c^{0.14}}+\frac{1}{C_h\frac{k_h}{D_{hyd}}\left(\frac{D_{hyd}G}{\mu}\right)_h^P\left(\frac{c_p\mu}{k}\right)_h^{1/3}\left(\frac{\mu}{\mu_s}\right)_h^{0.14}} \tag{5.10}$$

Multiplying both sides of the above equation by

$$\frac{k_c}{D_{hyd}}\left(\frac{D_{hyd}G}{\mu}\right)_c^P\left(\frac{c_p\mu}{k}\right)_c^{1/3}\left(\frac{\mu}{\mu_s}\right)_c^{0.14} \tag{5.11}$$

gives:

$$\left(\frac{1}{U}-\left(\frac{t}{k}\right)_{wall}\right)\left[\frac{k_c}{D_{hyd}}\left(\frac{D_{hyd}G}{\mu}\right)_c^P\left(\frac{c_p\mu}{k}\right)_c^{1/3}\left(\frac{\mu}{\mu_s}\right)_c^{0.14}\right]=\frac{1}{C_c}+\frac{\frac{k_c}{D_{hyd}}\left(\frac{D_{hyd}G}{\mu}\right)_c^P\left(\frac{c_p\mu}{k}\right)_c^{1/3}\left(\frac{\mu}{\mu_s}\right)_c^{0.14}}{C_h\frac{k_h}{D_{hyd}}\left(\frac{D_{hyd}G}{\mu}\right)_h^P\left(\frac{c_p\mu}{k}\right)_h^{1/3}\left(\frac{\mu}{\mu_s}\right)_h^{0.14}} \tag{5.12}$$

which is in the form of

$$Y = mX + b \tag{5.13}$$

where

$$Y=\left(\frac{1}{U}-\left(\frac{t}{k}\right)_{wall}\right)\left[\frac{k_c}{D_{hyd}}\left(\frac{D_{hyd}G}{\mu}\right)_c^P\left(\frac{c_p\mu}{k}\right)_c^{1/3}\left(\frac{\mu}{\mu_s}\right)_c^{0.14}\right] \tag{5.14}$$

$$X = \frac{\frac{k_c}{D_{hyd}}\left(\frac{D_{hyd}G}{\mu}\right)_c^P\left(\frac{c_p\mu}{k}\right)_c^{1/3}\left(\frac{\mu}{\mu_s}\right)_c^{0.14}}{\frac{k_h}{D_{hyd}}\left(\frac{D_{hyd}G}{\mu}\right)_h^P\left(\frac{c_p\mu}{k}\right)_h^{1/3}\left(\frac{\mu}{\mu_s}\right)_h^{0.14}} \tag{5.15}$$

$$m = \frac{1}{C_h} \tag{5.16}$$

and

$$b = \frac{1}{C_c} \tag{5.17}$$

Since the viscosity ratio groups and the Reynolds number exponents are relaxed with the fluid flow rates and temperatures, successive linear regressions can be performed to execute the nonlinear regression that these equations require. These two linear regressions consist of evaluating X (Equation 5.15) and Y (Equation 5.14) and X’ (Equation 5.18) and Y’ (Equation 5.19).

$$X' = \ln\left(\mathrm{Re}_c\right) \tag{5.18}$$

$$Y' = \ln\left(C_c \mathrm{Re}_c^P\right) \tag{5.19}$$

The X and Y regression starts with an initial P value as well as a guess for the C_h value. These values have an impact on the wall temperature calculations; therefore, the viscosity ratio must be adjusted in both linear regression processes. From the X and Y regression, C_c and C_h coefficients are found. This C_h coefficient is then used in a mathematical relaxation method to converge the viscosity ratio in the X’ and Y’ linear regression, producing values of P and C_c. The new P is used in the next iteration of regressions (which has new viscosity ratios to be relaxed), and this C_c is compared to the C_c of the X and Y regression. Calculations continue following this procedure until the difference between the successive P and C_h values and the C_c values from the X-Y and X'-Y' linear regressions reach a predetermined allowable error. These values can then be verified by executing a reverse calculation that requires multiplying both sides of Equation 5.10 by the hot side heat transfer denominator instead of the cold side heat transfer denominator, and undergoing the same process to converge at similar P, C_c and C_h coefficients. Both calculation procedures were done in this study and minute differences were observed between the two methods, so the average of the two methods coefficients was taken into account.

5.2 Pressure Drop

To determine the single-phase pressure drop due to friction across the brazed plate heat exchanger, the manifold pressure loss (pressure loss from pressure transducer location to just after the port of the exchanger) was subtracted from the measured pressure drop recorded by a differential pressure transmitter.

$$\Delta P_f = \Delta P_{total} - \Delta P_{man} \tag{5.20}$$

The contribution of pressure loss due to gravitation was zero in this case since the pressure drop was measured using a single differential pressure transducer. The manifold pressure loss was estimated by 1.5 times the inlet velocity head, as reported by Shah and Wanniarachchi [5],

$$\Delta P_{man} = 1.5\left(\frac{u_m{}^2 \rho}{2}\right) \tag{5.21}$$

where u_m is the mean velocity of the fluid at the manifold.

The Fanning friction factor is given by

$$C_f = \Delta P_f \frac{D_{hyd}\rho}{2L_p G^2} \tag{5.22}$$

where L_p is the characteristic length, which was here defined as the distance from the middle of the top inlet port to the middle of the bottom outlet port. The Fanning friction factor in the turbulent regime can then be correlated based on the Reynolds number by the following general form:

$$C_f = C'\mathrm{Re}^{-p'} \tag{5.23}$$

CHAPTER 6: SINGLE-PHASE RESULTS

Using the single-phase equations and analysis techniques, the data could then be properly interpreted and compared. Comparisons between the three different plates as well as with other established single-phase studies are presented in this chapter.

6.1 Heat Transfer

The single-phase analysis was conducted on the three previously described brazed plate heat exchangers. Data are presented of the water/water analysis as well as the dynalene/water analysis. Implementing the modified Wilson plot technique and reverse calculations for the three different plates gave correlations with an average standard deviation less than 1%. The plots of the modified Wilson method for each plate are shown in Figure 6.1, while the heat transfer correlations are presented in Table 6.1.

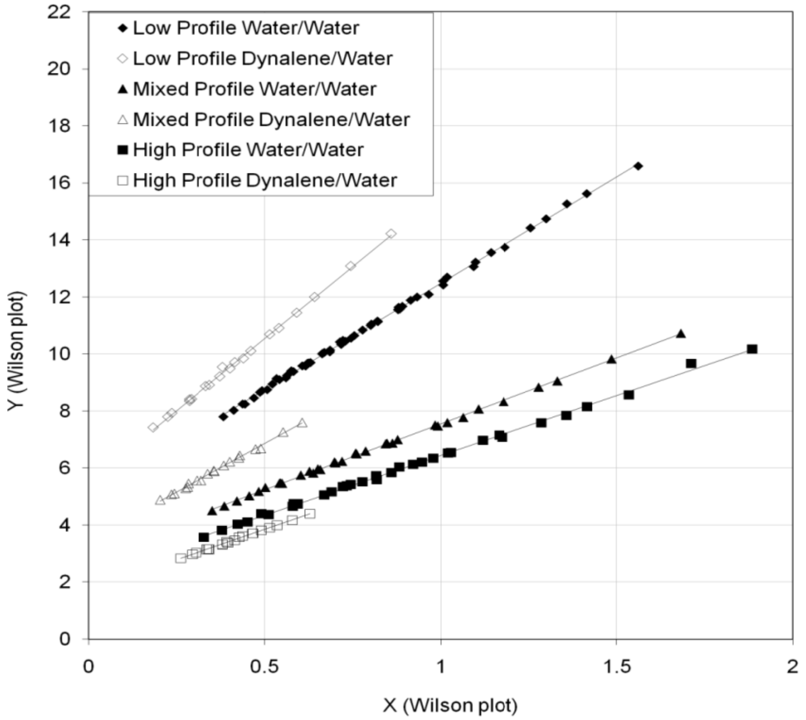

Figure 6.1 Modified Wilson plot including water/water and dynalene/water.

Table 6.1 Current study single-phase heat transfer correlations

$$Nu=C.Re^{P}.Pr^{(1/3)}.(\mu/\mu_{s})^{0.14}$$

water/ water	60/60 Plate	27/60 Plate	27/27 Plate
C_h	0.134	0.214	0.240
P	0.712	0.698	0.724

dynalene/ water	60/60 Plate	27/60 Plate	27/27 Plate
C_c	0.177	0.278	0.561
P	0.744	0.745	0.726

With plate heat exchangers, defining plate orientation (whether installation of the plate is vertical or horizontal) and hot and cold fluid flow direction in a single-phase study is not as critical as it is in two-phase flow. Installation orientation and direction of flow in plate heat exchangers in two-phase flow is very important because the gravitational effects can help or hinder evaporation and condensation. However, based upon the present experimentation, it is interesting to note that mixed angle exchangers may require such a definition in single-phase flow. Because the neighboring plates alternate chevron angles, mixed-angle exchangers exhibit different behavior for opposite flow directions. For example, if a 30/60 mixed-angle exchanger consists of plates where the high-profile (30°) plates are pointed up and the low-profile (60°) plates are pointed down, the middle channel's fluid would have a different flow pattern in this orientation compared to the opposite orientation, where the high-profile (30°) plates are pointed down and the low-profile (60°) plates are pointed up. In the 60/60 and 30/30 exchangers, this problem is eliminated because the fluid's flow pattern is similar regardless of flow direction. This was apparent in the dynalene/water data which demonstrated that in one orientation the C_c, C_h, and P values were 0.272, 0.136, and 0.759, respectively, and in the opposite orientation the corresponding values were 0.278, 0.143, and 0.745. The latter data is reported here because its orientation is similar to the two phase experimentation.

In order to properly compare the findings presented in this paper with those by other authors in the field, a meticulous comparison of definitions and calculations needed to be accomplished to make sure that continuity was maintained. For the most part, parameters were commonly defined, but there were discrepancies among them. One of these was the definition and use of the characteristic flow length. It is important to note that the length (and resulting area) along the plate that experiences heat transfer is not the same length that contributes to a pressure drop, and as such, different lengths should be defined and utilized for each calculation. In various published plate heat exchanger literature, common definitions of length include "heat transfer length", "port to port length", "length between ports", "length of channel", "chevron area length", "distribution region length", and just "length". As these researched calculations and correlations will ideally be used in industry, simple, externally measured, and logical lengths should be used. The length used to find the amount of heat transfer area is most easily attained by measuring the distance between the ports (L_{HT}), i.e., the distance measured from the top of the bottom port to the bottom of the top port. No heat transfer occurs at the entrance of each port and it is impossible to know, by external examination, exactly where the entrance or distribution length of the plate ends, and the chevron area begins, and exactly how much of the distribution length actually transfers heat. The pressure drop length, however, is affected by the distance that the fluid travels through the ports, therefore an easy measurement between the middle of each port suffices (L_P). The data from other authors being compared with the present data has been mapped to eliminate the discrepancies that arise from the inconsistencies of definitions and calculations. For example, the heat transfer area from other studies was converted to the definition in the present study. Comparing these results shows consistent qualitative heat transfer behavior, as shown in Figure 6.2 through Figure 6.4 for the three plates, although there are still quantitative differences that can be attributed to different geometrical plate configurations and flow conditions.

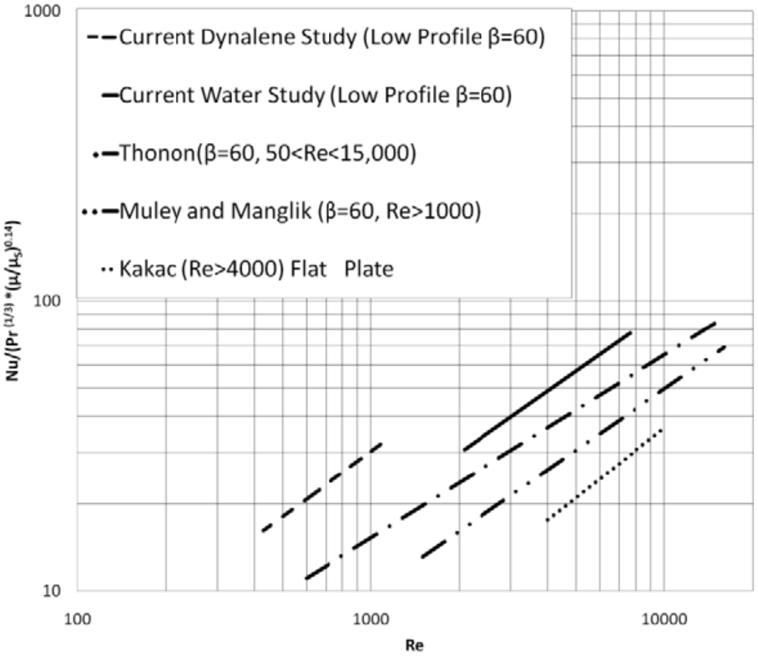

Figure 6.2 Single-phase heat transfer comparison of low profile plates.

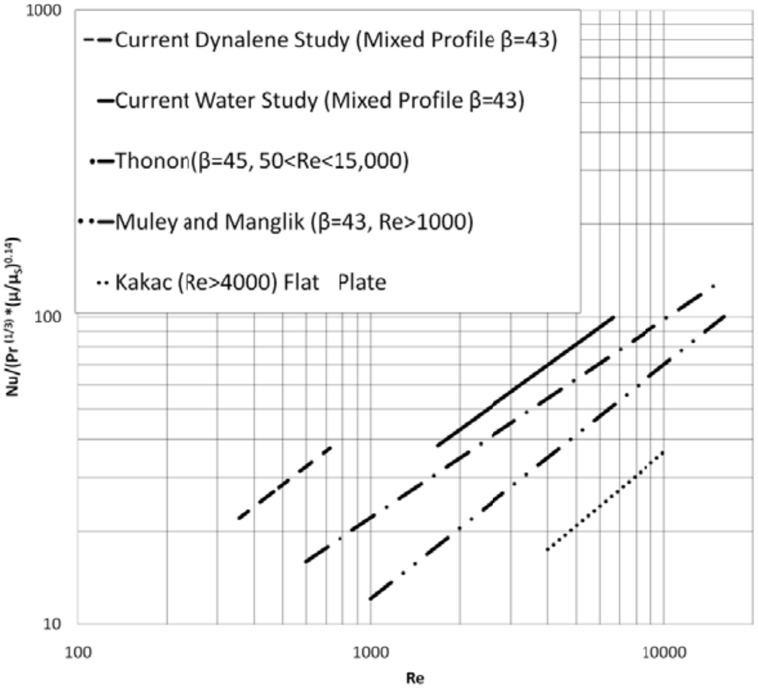

Figure 6.3 Single-phase heat transfer comparison of mixed profile plates.

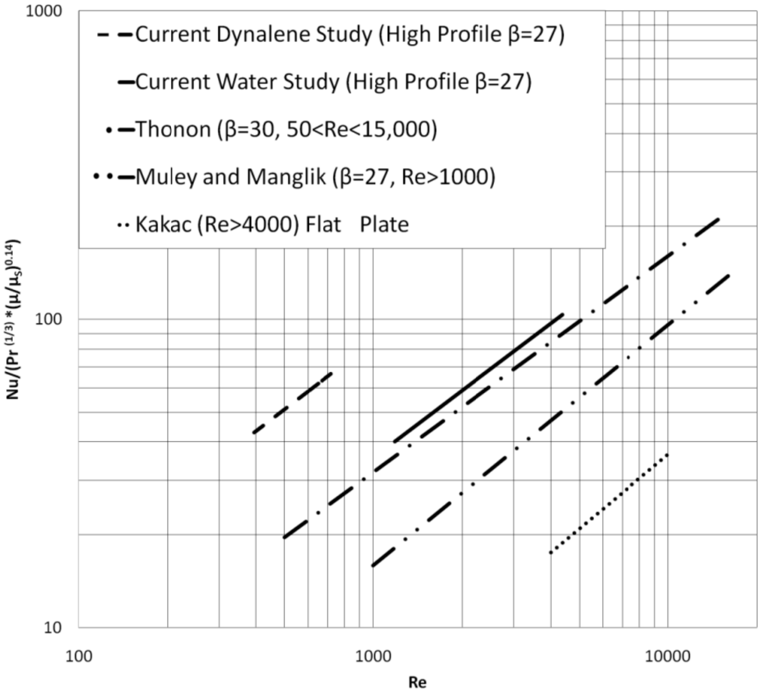

Figure 6.4 Single-phase heat transfer comparison of high profile plates.

6.2 Pressure Drop

The pressure drop through the middle channel of the three brazed plate heat exchangers was recorded by a differential pressure transducer. The pressure drop reported is based on the assumption of L_P, meaning that the length used in the calculations was not that of the heat transfer length but the length measured from the middle of the top port to the middle of the bottom port. The resulting correlations are summarized in Table 6.2, and compared with other studies in Figure 6.5 through Figure 6.7. In the Fanning friction correlations the P' coefficient values depict how much the flow influences pressure drop; the closer the value to zero, the less the flow depends on the Reynolds number to depict pressure drop and the friction factor becomes constant. This behavior is also related to the roughness that the fluid sees as it flows through the exchanger. Roughness can be very smooth or very rough, contributing a little or greatly to the pressure drop respectively. The geometry of the corrugated (very unsmooth) plates actually lends to a very large roughness, so the P’ values reported in Table 6.2 show that the pressure drop in each of the plates is not entirely dependent on the Reynolds number, and that all of the present study flows are in the turbulent regime, even at low Reynolds numbers.

Table 6.2 Current study fanning friction factor correlations

$$C_f = C'.Re^{P'}$$

water/ water	60/60 Plate	27/60 Plate	27/27 Plate
C’	1.18	1.56	3.09
P’	-0.10	-0.08	-0.06

dynalene/ water	60/60 Plate	27/60 Plate	27/27 Plate
C’	0.57	21.40	3.15
P’	0	-0.46	-0.08

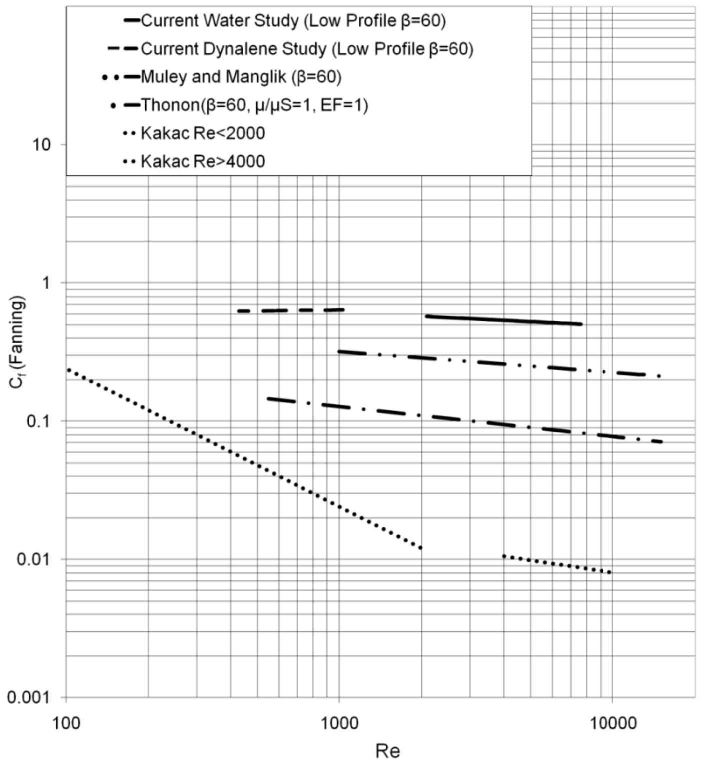

Figure 6.5 Fanning friction factor for low profile plates.

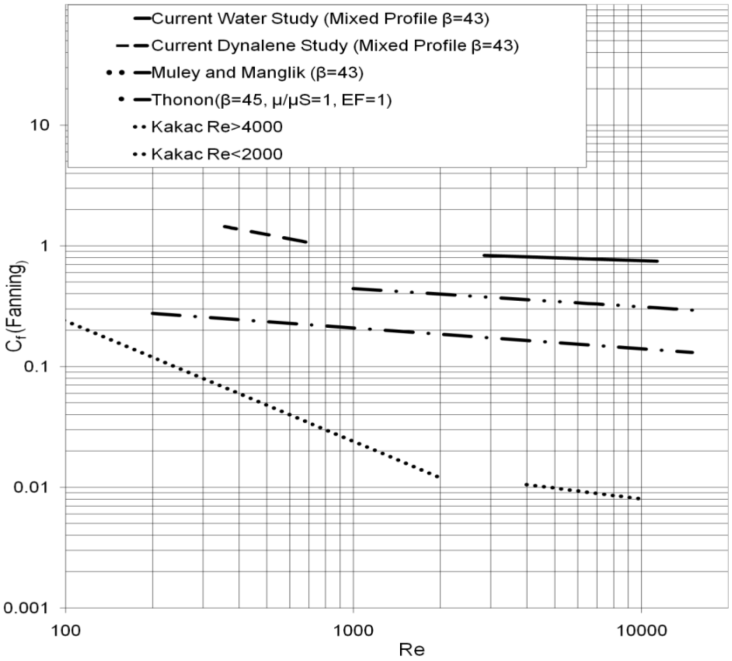

Figure 6.6 Fanning friction factor for mixed profile plates.

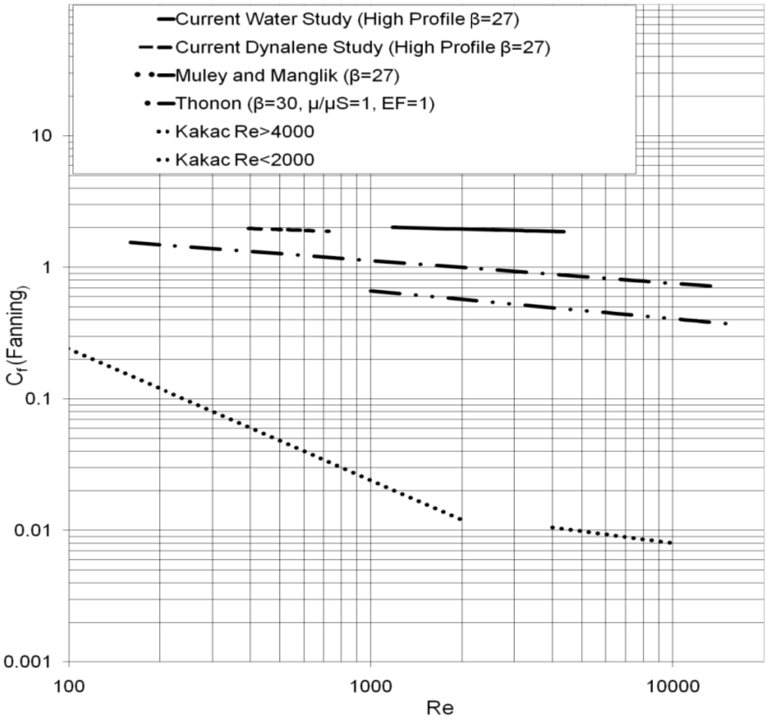

Figure 6.7 Fanning friction factor for high profile plates.

It is important to note that the previous comparisons between studies do not necessarily show that one heat exchanger is better than another, because the heat exchanger correlations in the different studies (i.e. the present study compared to Thonon, or Thonon compared to Muley and Manglik) use different sized heat exchangers with similar (not always exact) inclination angles. Many more geometric plate parameters can affect the flow and heat transfer, such as plate spacing, corrugation pitch and over all aspect ratio of the plate (whether the plate's height is twice or three times the length of the plate, essentially describing how 'slender' the plate is). With this information in mind, it was more prudent to find single-phase correlations for the specific plates used in this study then it would have been to simply use another researcher's correlation made from similar plates. These plates now have their own descriptive single-phase models that will be used for their respective two-phase modeling correlations.

6.3 Uncertainty Analysis

Each device had unique responses and uncertainties, all of which were taken into account when performing a single-phase propagation of error analysis. An example uncertainty equation is given in equation 6.1. The uncertainties for the study are presented in Table 6.3.

$$U(Re) = \frac{1}{Re} \cdot \left\{ \begin{matrix} \left(\frac{\partial Re}{\partial \rho} U(\rho) \cdot \rho\right)^2 + \left(\frac{\partial Re}{\partial \mu} U(\mu) \cdot \mu\right)^2 \\ + \left(\frac{\partial Re}{\partial Q_f} U(Q_f) \cdot Q_f\right)^2 + \left(\frac{\partial Re}{\partial D} U(D) \cdot D\right)^2 + \end{matrix} \right\}^{1/2} \tag{6.1}$$

Table 6.3 Uncertainty of calculated correlations

Correlation	Coefficient (Range in Correlations)	Calculation Uncertainty
Single-phase Fanning friction factor	C_f (0.2-2.3)	±1.3%
Single-phase heat transfer	h (8-27 kW/(m^2*K))	±4.4%

The uncertainty calculated for the single-phase correlations reported in Table 6.3 are actually the uncertainty for a given experimental point, not for the whole correlation itself. For example, for single-phase heat transfer, if a data point that was collected gave a value of 10 kW/m^{2}K at a certain flow, it would actually be expected to have a heat transfer value between 9.56-10.44 kW/m^{2}K. The scatter of data points taken between 8-27 kW/m^{2}K and the uncertainty of where they lie with respect to the correlation line is not described here.

CHAPTER 7: TWO-PHASE CONDENSATION EXPERIMENTATION

With a completed single-phase analysis of the three brazed plate heat exchangers, a two-phase condensation analysis commenced. The two-phase experimentation set up and test procedure are reviewed to demonstrate the level of control achieved over the system. A breakdown of how the data was collected is also explained.

7.1 Schematic and Setup

All of the same equipment which was used in the single-phase data collection setup was used for the two-phase setup. In addition, the CO_2 pump, Coriolis flow meter, after condenser, evaporator, control valves, and a 1000 psi pressure relief valve were inserted into the CO_2 line. All the components of the CO_2 line were connected with high pressure flexible hose, 3/8" on the liquid side and ¾" on the vapor side. The two-phase setup consisted of the tested brazed plate heat exchanger, an after condenser (a 20-plate 5" by 10" BPHE), CO_2 pump, and evaporator (a 20-plate 5" by 10" BPHE) to complete the refrigeration pump loop. Originally the system had a pressure regulator valve that served to break the vapor pressure, but after some initial difficulties of operating the system (a stoppage of flow believed to be originating from the pressure regulator valve), the valve was removed. The pressure drop created from the tubing and heat exchangers proved to be enough to operate the system adequately. Since only the condensation portion of the refrigeration cycle was studied, it was not necessary to use a compressor to simulate the refrigeration cycle; rather, a refrigeration pump loop, that operates similar to a heat pipe, was used to complete the condensation portion of the refrigeration cycle as shown in Figure 7.1.

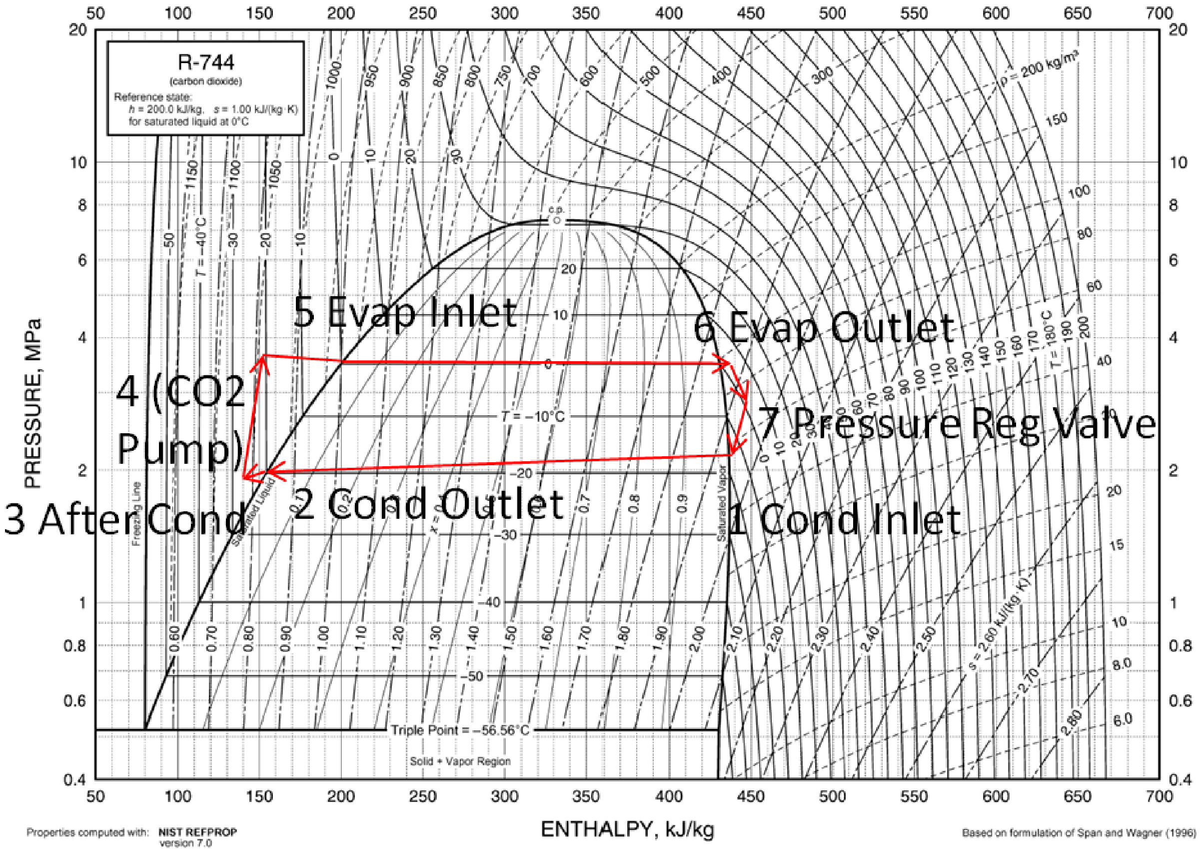

Figure 7.1 Ideal thermodynamic cycle of the two-phase condensation in refrigeration pump loop.

Figure 7.2 details the two-phase schematic and Figure 7.3 shows the physical lab experimentation setup. The testing conditions that ASHRAE had specified for the two-phase condensation experimentation were as follows:

1. Saturated CO_2 temperature range: 0°F (-17.8°C) to -30°F (-34.4°C)
2. Heat flux range: 800 Btu/hr.ft^2 (2.5 kW/m^2) to 5,000 Btu/hr.ft^2 (15.7 kW/m^2)
3. Inlet condition: superheated gas to saturated vapor
4. Outlet condition: saturated liquid to sub cooled liquid
5. Approach temperature: not to exceed 10°F (5.6°C)

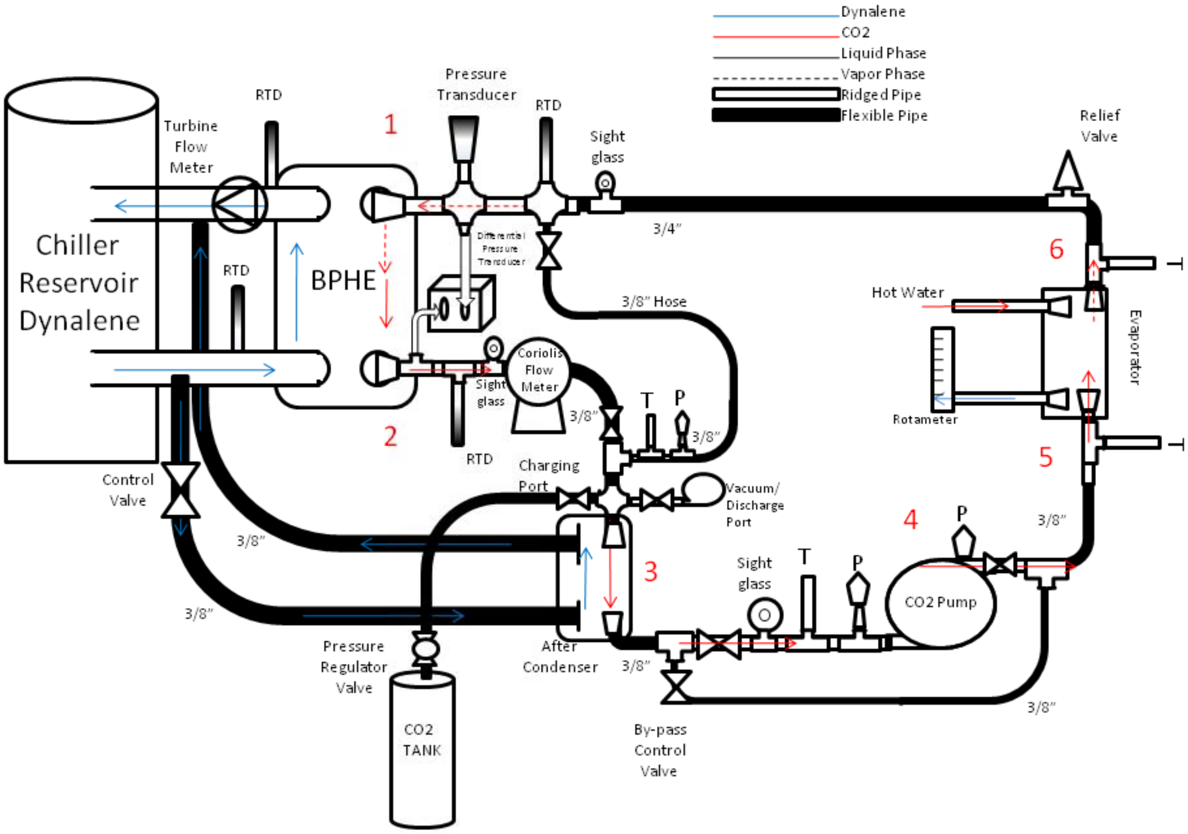

Figure 7.2 Two-phase schematic.

Figure 7.3 Two-phase experimental facility.

7.2 Experimental Test Procedure

To record the data and monitor the two-phase system, the same National Instruments data acquisition equipment from the single-phase system was used, but with an updated two-phase program. Inlet and outlet temperatures for both dynalene and CO_2 were recorded as well as their respective flow rates. Real time pressures and temperatures at the inlet and outlet of the CO_2 side of the condenser were monitored and compared to data tables from NIST REFPROP v 8.0 to make sure that superheated and sub cooled states of CO_2 were achieved. In order to properly run the system, a series of steps were performed to ensure the desired accurate data were collected.

1. Vacuum the entire CO_2 line using the laboratory's vacuum line. Wait till the system pressure reads a gauge pressure between -12 to -13 psi (absolute pressure of 2 to 3 psi). This may take up to an hour to achieve. It is important to make sure that non-condensable gasses (air) are not mixed in the CO_2 line.
2. Turn the chiller on, achieving the desired dynalene temperature. Open the valves to allow dynalene to flow through the condenser and the after condenser.
3. Start either cold or hot tap water flowing through the evaporator brazed plate heat exchanger.
4. Introduce CO_2 into the system, only to about 300 psi of CO_2 at a time. Wait till the dynalene cools the CO_2 and the pressure drops down to about 225 or 250 psi, then introduce more CO_2. Repeat this till the CO_2 outlet temperature is within a few degrees of the dynalene.
5. Once the outlet CO_2 temp is sub cooled liquid CO_2, it is safe to start the CO_2 pump.
6. Turn on the CO_2 pump at frequencies ranging from 15-25 Hz. While the CO_2 pump is initially starting up, make sure to check the sight glass at the entrance of the pump

to make sure liquid is entering the pump. It is not uncommon for the system to require more CO_2 at this stage, introduce more CO_2 slowly, making sure to not exceed 450psi, until visible liquid is entering the pump.

7. Once liquid CO_2 is flowing through the CO_2 pump, increase the pump frequency to 45-50 Hz.
8. Monitor the condenser inlet CO_2 temperature, which will be initially 30° to 40° C superheat. Slowly add more CO_2 to the system to drop the CO_2 inlet temperature. Be patient, as adding too much refrigerant will cause the entire line to become liquid. Add small amounts of CO_2 and wait till the superheat temperature and pressure become steady state.
9. Continue adding CO_2 till the superheat and sub cooled temperatures are within 5° C of the respective saturated pressures.
10. Once the desired CO_2 flow is achieved and superheat and sub cooled parameters are met and held at steady state (check the sight glasses at the entrance and exit of the brazed plate heat exchanger to ensure that no liquid is present at the entrance and that liquid flows at the end of the plate), begin recording data.
11. Data sets are recorded once every 10 seconds for 15 minutes for a total of 90 sets of data per point.
12. After a successful point has been recorded, lower the chiller temperature to the next specified point. Keep in mind that it is easier to acquire data points with similar flow rates at the different temperatures than it is to keep the temperature constant and vary the flow rates.

13. Minor adjustments may need to be made to keep the approach temperatures within 5 degrees C and the flow at similar rates. These adjustments can be made by adjusting bypass valves around the condenser and after condenser as well as the amount of CO_2 in the system.

As given per the required test conditions that ASHRAE set forth, the following testing matrix was used as a guide to take data for each plate. Data was taken in heat flux groupings, keeping a similar flow rate while changing the saturation temperatures. To calculate the needed flow rate for a given temperature and heat flux the following equation was used,

$$\dot{m} = Q"A_{Tot}/i_{fg} \tag{7.1}$$

where Q” is the required heat flux and i_{fg} is the latent enthalpy at the desired condensation temperature.

Table 7.1 Mass flow requirement matrix to fulfill temperature and heat flux ranges

Mass Flows (kg/s)		*Heat Flux (kW/m^2)*							
		20	*17.5*	*15*	*12.5*	*10*	*7.5*	*5*	*2.5*
Temp C (4 Deg Step)	**-17.6**	0.00979	0.00856	0.00734	0.00612	0.00489	0.00367	0.00245	0.00122
	-21.6	0.00948	0.00830	0.00711	0.00593	0.00474	0.00356	0.00238	0.00119
	-26	0.00919	0.00804	0.00689	0.00574	0.00460	0.00345	0.00230	0.00115
	-30	0.00895	0.00783	0.00671	0.00559	0.00448	0.00336	0.00224	0.00112
	-34.4	0.00871	0.00762	0.00653	0.00544	0.00435	0.00327	0.00218	0.00109
	-38	0.00853	0.00746	0.00640	0.00533	0.00426	0.00320	0.00213	0.00107

Each data point was observed as it was recorded to make sure that steady state was achieved. If pressures or temperatures ever deviated from the beginning of taking the point, the data point was retaken. Figure 7.4 shows an example of the system at steady state recording a single data point. The table on the right hand side of the DAQ in Figure 7.4 is NIST REFPROP v8.0 giving the saturation temperatures and pressures of CO_2. The pressure readings of the inlet and exit of the condenser were read off of the NIST table. For example, if the monitored CO_2

inlet temperature at the monitored inlet pressure was higher than the NIST saturation temperature, superheat vapor state was achieved. Likewise for the exit, if the monitored CO_2 exit temperature at the monitored exit pressure was lower than the NIST saturation temperature, sub cooled liquid state was achieved.

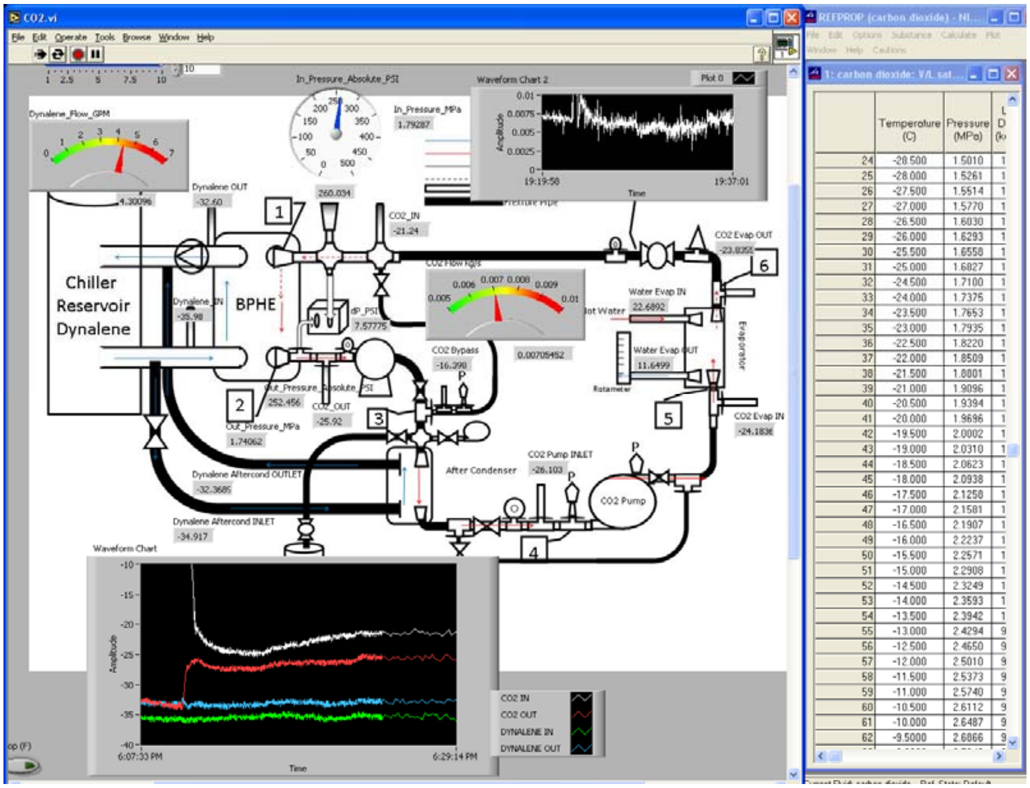

Dynalene_Flow_GPM 4.30096

Dynalene OUT -32.60

In_Pressure_Absolute_PSI 260.034

In_Pressure_MPa 1.79287

CO2_IN -21.24

CO2 Evap OUT -23.8355

Dynalene_IN -35.98

dP_PSI 7.57775

CO2 Flow kg/s 0.00705452

Water Evap IN 22.6892

CO2 Bypass -16.390

Water Evap OUT 11.6499

Out_Pressure_Absolute_PSI 252.456

CO2_OUT -25.92

Out_Pressure_MPa 1.74062

CO2 Evap IN -24.1836

CO2 Pump INLET -26.103

Dynalene Aftercond OUTLET -32.3685

Dynalene Aftercond INLET -34.917

	Temperature (C)	Pressure (MPa)	L D (k
24	-28.500	1.5010	1
25	-28.000	1.5261	1
26	-27.500	1.5514	1
27	-27.000	1.5770	1
28	-26.500	1.6030	1
29	-26.000	1.6293	1
30	-25.500	1.6558	1
31	-25.000	1.6827	1
32	-24.500	1.7100	1
33	-24.000	1.7375	1
34	-23.500	1.7653	1
35	-23.000	1.7935	1
36	-22.500	1.8220	1
37	-22.000	1.8509	1
38	-21.500	1.8801	1
39	-21.000	1.9096	1
40	-20.500	1.9394	1
41	-20.000	1.9696	1
42	-19.500	2.0002	1
43	-19.000	2.0310	1
44	-18.500	2.0623	1
45	-18.000	2.0938	1
46	-17.500	2.1258	1
47	-17.000	2.1581	1
48	-16.500	2.1907	1
49	-16.000	2.2237	1
50	-15.500	2.2571	1
51	-15.000	2.2908	1
52	-14.500	2.3249	1
53	-14.000	2.3593	1
54	-13.500	2.3942	1
55	-13.000	2.4294	9
56	-12.500	2.4650	9
57	-12.000	2.5010	9
58	-11.500	2.5373	9
59	-11.000	2.5740	9
60	-10.500	2.6112	9
61	-10.000	2.6487	9
62	-9.5000	2.6866	9

Figure 7.4 DAQ showing steady state conditions.

CHAPTER 8: TWO-PHASE DATA REDUCTION

The two-phase condensation data collected by the data acquisition system are used to obtain heat transfer and pressure drop correlations within the three tested brazed plate heat exchangers. This chapter reviews the two-phase data reduction methods.

8.1 Two-Phase Condensation

In order to have complete two-phase condensation, it is important to ensure that superheated vapor and sub cooled liquid are actually present at the entrance and exit of the heat exchanger respectively. To do so, the inlet and outlet temperatures and pressures must be measured and monitored carefully. In the data reduction process, the properties of CO_2 are found by the recorded average pressure and temperature at the inlet and exit by way of NIST REFPROP V8.0. By copying the pressure and temperature for each data point into the NIST software program, the superheated and sub cooled enthalpies can be calculated. Multiplying the difference in enthalpies by the mass flow rate of the CO_2 gives the total energy loss of the CO_2.

$$Q_{CO2} = (i_{in} - i_{out})\dot{m}_{CO2} \tag{8.1}$$

Dividing the energy loss by the surface area by which the CO_2 dissipates heat renders the overall heat flux:

$$q^{"} = \frac{Q_{CO2}}{A_{surface}} \tag{8.2}$$

This heat flux however is not the condensation heat flux. The heat flux depicted here takes into account the superheated pressure and temperature as well as the sub cooled pressure and temperature, so this flux contains three regimes of heat transfer; superheat, saturated liquid/vapor, and sub cooled heat flux. To be as accurate as possible in two-phase data reduction, it is important to understand how much of the energy that is dissipated is sensible energy (superheat and sub cooled regimes) and how much is latent energy (energy used to condense). In this experimentation's parameters, the approach temperature was never to exceeded 5°C, which means that the intended super heat temperature measured at the inlet port of the exchanger was to be as close to the saturation temperature as possible, but just high enough to ensure 100% vapor and not exceed 5°C from the saturated vapor pressure's temperature. Similar to superheat, the approach temperature describes how the intended sub cooled temperature (measured outside the exchanger outlet port) needed to be lower than the saturated liquid temperature to ensure a full liquid state, but no colder than 5°C from the saturated liquid pressure's temperature. The saturated temperature for each data point was thus mathematically found (not empirically found from data acquisition equipment) at each inlet and exit pressure. The idea behind this is to find out how many degrees superheat and sub cooled (approach temperature) the CO_2 has achieved, as well as determining how much energy was dissipated in each of the single-phase regimes. Finding the energy in each regime requires more mathematical work, but not doing so would render erroneous correlations. For example, no two approach temperatures are identical from one condensation data point to another, and if no separation of regimes was implemented, any given condensation point would have much more energy reported for a higher approach temperature than a lower approach temperature. The separation of the three regimes in the two-phase flow cancels out the need to have every condensation point have exact approach temperatures for vapor and liquid and gives more accurate saturation condensation correlations.

To properly separate the three regimes of CO_2, the difference in enthalpies of the calculated saturated vapor/liquid and the recorded superheat/sub cooled liquid pressure were multiplied by the CO_2 mass flow rate to give the amount of energy dissipated in the superheat and sub cooled regions of the plate.

$$Q_{CO2\,Sup} = (i_{in} - i_g)\dot{m}_{CO2} \tag{8.3}$$

$$Q_{CO2\,Sub} = (i_f - i_{out})\dot{m}_{CO2} \tag{8.4}$$

Subtracting the superheat and sub cooled heat from the total CO_2 heat loss gives the saturated heat, or the two-phase heat transfer amount.

$$Q_{CO2\,Sat} = Q_{CO2\,Tot} - Q_{CO2\,Sup} - Q_{CO2\,Sub} \tag{8.5}$$

To accurately find the overall heat transfer coefficients and Nusselt numbers of the condensing CO_2, all three regions need to be accounted for. This involves accurately estimating the amount of surface area occupied in the exchanger where only single-phase vapor and single-phase liquid exist. The rest of the surface area in the exchanger is then estimated to be in two-phase condensation and it is this area of heat transfer that must be reported and analyzed. A simple yet practical homogeneous model for two-phase flow is assumed and Figure 8.1 depicts how the flow may appear in the heat exchanger during the condensation process. This assumption and the diagram in Figure 8.1 are not exact representations of what is physically occurring in the exchanger, but using this assumption leads to more accurate correlations than those that would have been found without using the assumption.

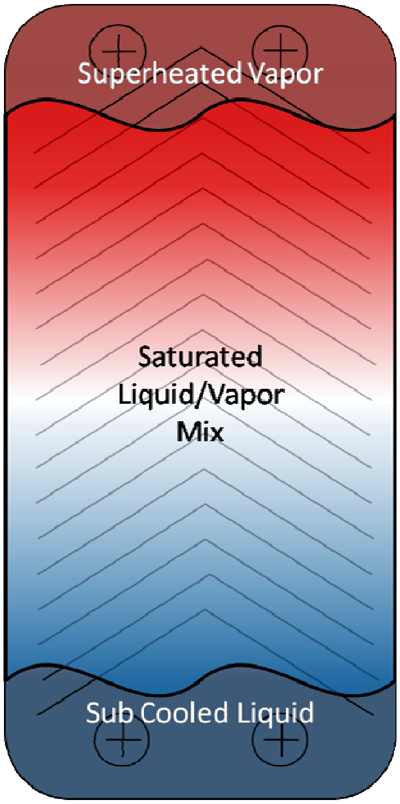

Figure 8.1 Three regions of two-phase condensation.

The data on the heat absorption side of the heat exchanger, containing dynalene, also needs to be organized and reduced, for it will be integral in the two-phase analysis later on. The inlet and outlet temperatures as well as the flow rate for the dynalene were monitored and recorded. The temperatures were used to find properties, which were obtained by using the same third order logarithmic relations as in the single-phase analysis for dynalene.

Even though the heat absorbing fluid was always single-phase, the two-phase CO_2 information was used to find out how much of the dynalene contributed to absorbing heat from the superheat region, the saturated dome region, and the sub cooled region. Figure 8.2 describes how the fluids interact thermodynamically.

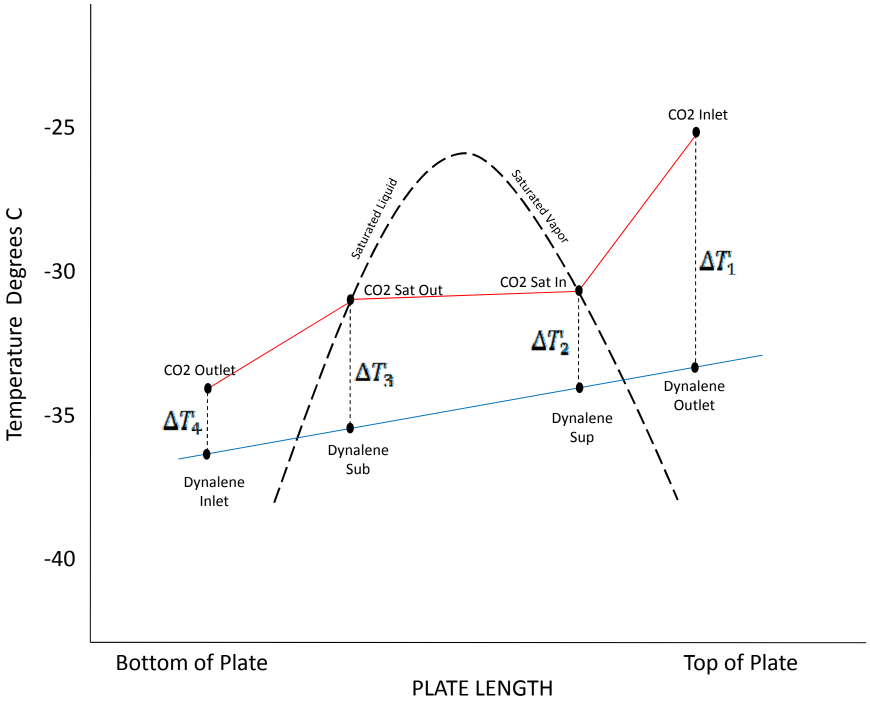

Figure 8.2 Thermodynamic display of two-phase CO_2 with single-phase dynalene.

Realizing that the installed RTDs only recorded temperatures at the inlet and outlet ports of the exchanger, mathematical estimations were needed to find the saturation temperatures (vapor and liquid temperatures at estimated locations in the channels of the plate) and the respective dynalene temperatures at those CO_2 saturated temperature locations. The dynalene Sub and Sup temperatures, relating to the calculated CO_2 saturated vapor and liquid temperatures, were found by using equations 8.6 and 8.7 respectively.

$$T_{Dyn\ Sup} = \frac{-Q_{CO2\ Sup}}{\dot{m}_{Dyn} c_{p\ Dyn\ In}} + T_{Dyn\ Out} \tag{8.6}$$

$$T_{Dyn\ Sub} = \frac{Q_{CO2\ Sub}}{\dot{m}_{Dyn} c_{p\ Dyn\ Out}} + T_{Dyn\ In} \tag{8.7}$$

Finding the log mean temperature differences for the superheat, saturated and sub cooled regions are defined as follows:

$$\Delta LMTD_{Sup} = \frac{\Delta T_1 - \Delta T_2}{\ln(\Delta T_1/\Delta T_2)} \tag{8.8}$$

$$\Delta LMTD_{Sat} = \frac{\Delta T_2 - \Delta T_3}{\ln(\Delta T_2/\Delta T_3)} \tag{8.9}$$

$$\Delta LMTD_{Sub} = \frac{\Delta T_3 - \Delta T_4}{\ln(\Delta T_3/\Delta T_4)} \tag{8.10}$$

where

$$\Delta T_1 = T_{CO2\ Inlet} - T_{Dyn\ Outlet} \tag{8.11}$$

$$\Delta T_2 = T_{CO2\ Sat\ In} - T_{Dyn\ Sup} \tag{8.12}$$

$$\Delta T_3 = T_{CO2\ Sat\ Out} - T_{Dyn\ Sub} \tag{8.13}$$

$$\Delta T_4 = T_{CO2\ Outlet} - T_{Dyn\ Inlet} \tag{8.14}$$

To find heat transfer coefficients for each of the three regimes, the Sieder-Tate form of the heat equation as given by Incropera and DeWitt [33]

$$Nu = CRe^{P}Pr^{1/3}(\mu/\mu_s)^{0.14} \tag{8.15}$$

where

$$Re = \frac{GD_{hyd}}{\mu} \tag{8.16}$$

$$Pr = \frac{c_p\mu}{k} \tag{8.17}$$

where properties were taken at the temperature averages in each regime for both CO_2 and dynalene. Even in the saturated regime, where the span of Reynolds and Prandtl numbers is large, the average of the vapor and liquid properties were used. The viscosity ratio term, which contains the viscosity of the fluid taken at the temperature of the surface, assumes a linear temperature profile between the two working fluids and thus the viscosity property is calculated at the average temperature of the average CO_2 and average dynalene temperatures for each regime. This linear temperature profile assumption to estimate the surface temperature turns out to be a sound assumption due to the fact that the resulting heat transfer coefficients are on the same order of magnitude. Were the heat transfer coefficients of CO_2 and dynalene on different orders of magnitude, the temperature profile would most likely not be linear.

$$T_s \approx \frac{T_{CO2\ ave} + T_{Dyn\ ave}}{2} \tag{8.18}$$

The coefficients of C and P for both the superheat and sub cooled regions (single-phase) are the coefficients reported for each respective plate from the single-phase analysis, using the water/water C_h and P coefficients for the single-phase CO_2 side and the water/dynalene C_c and P coefficients for the dynalene side. Finding the Nusselt number for the CO_2 superheat/sub cooled regions and the dynalene superheat/sub cooled regions allows each of the heat transfer coefficient to be found.

$$h = \frac{kNu}{D_{hyd}} \tag{8.19}$$

Using the thermal resistance form

$$\frac{1}{U} = \frac{1}{h_{hot}} + \frac{t}{k} + \frac{1}{h_{cold}} \tag{8.20}$$

the overall heat transfer coefficient for the CO_2 superheat and sub cooled regions can be calculated by the following equations

$$\frac{1}{U_{CO2\ Sub}} = \frac{1}{h_{CO2\ Sub}} + \frac{t}{k} + \frac{1}{h_{Dyn\ Sub}} \tag{8.21}$$

$$\frac{1}{U_{CO2\ Sup}} = \frac{1}{h_{CO2\ Sup}} + \frac{t}{k} + \frac{1}{h_{Dyn\ Sup}} \tag{8.22}$$

and thus the areas of the superheated, sub cooled and saturated CO_2 regions can be calculated from the equations

$$A_{CO2\,Sub} = Q_{CO2\,Sub}/U_{CO2\,Sub}\Delta LMTD_{Sub} \tag{8.23}$$

$$A_{CO2\,Sup} = Q_{CO2\,Sup}/U_{CO2\,Sup}\Delta LMTD_{Sup} \tag{8.24}$$

$$A_{CO2\,Sat} = A_{CO2\,Tot} - A_{CO2\,Sub} - A_{CO2\,Sup} \tag{8.25}$$

The overall heat transfer CO_2 coefficient then can be found by using equation 8.26 but solving for U.

$$U_{CO2\,Sat} = Q_{CO2\,Sat}/A_{CO2\,Sat}\Delta LMTD_{Sat} \tag{8.26}$$

Using the resistance equation again will give the saturated heat transfer coefficient

$$\frac{1}{h_{CO2\,Sat}} = \frac{1}{U_{CO2\,Sat}} - \frac{t}{k} - \frac{1}{h_{Dyn\,Sat}} \tag{8.27}$$

which can be used to find the Nusselt number for the saturated CO_2 in equation 8.27.

$$Nu_{CO2\,Sat} = \frac{h_{CO2\,Sat}D_{hyd}}{k} \tag{8.27}$$

CHAPTER 9: TWO-PHASE RESULTS

Approximately 30 two-phase data points for each plate were recorded and analyzed. The data collected coincides with the objectives of the project by condensing CO_2 in the temperature range of -17.8°C to -34.4°C all within the range of fluxes of 2.5 kW/m^2 to 15.7 kW/m^2. Using the collected data to build two-phase correlations of heat transfer and friction factor is a very lengthy process that involves a dimensional analysis. Such analysis can include parameters and variables on the order of 10 to 20 per correlation. Such correlations are outside the scope of this thesis work and will not be presented, however, valuable relations and behaviors can be observed from the two-phase data when studying three to four variables. This chapter discusses the two-phase comparisons and observations of heat transfer and fluid flow, temperature gradients, heat transfer and mass flow, and pressure drop.

9.1 Dimensionless Heat Transfer and Fluid Flow

A common method of classifying a heat transfer relationship is through a dimensionless temperature gradient consisting of a heat transfer coefficient, a characteristic length and a thermal conductivity. These parameters combined make a Nusselt number. In a similar fashion, flow can be characterized by a dimensionless ratio of inertial and viscous forces using mass flow, a characteristic length and viscosity, which gives the relationship defined by the Reynolds number. Figure 9.1 shows a comparison of the two-phase Nusselt numbers and Reynolds numbers for each plate configuration. As the inclination angles or the profile of the plates increases, the heat transfer also increases at any given Reynolds number. As the Reynolds number or the flow increases through each plate though, the rate at which the heat transfer occurs in each plate differs, the lowest rate of change in the low profile plate and the highest rate of change in the high profile plate.

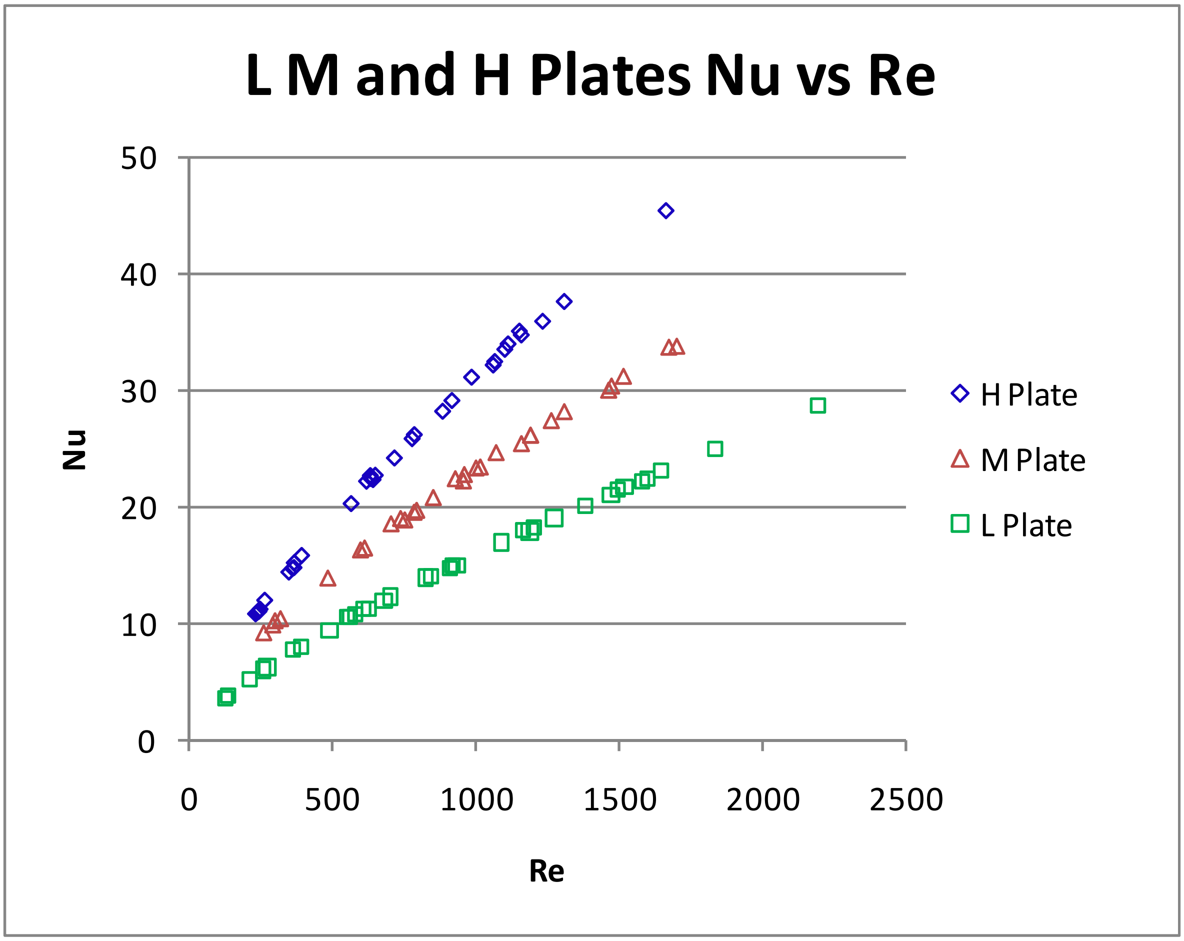

Figure 9.1 Three plates' CO_2 heat transfer and flow characteristics.

9.2 Temperature Gradient

There are several different ways to look at the two-phase data to understand how certain parameters affect the behavior of CO_2 condensing in each plate. One such parameter to observe is the temperature gradient consisting of the temperature of the surface to the temperature of the fluid passing by that surface. Figures 9.2 through 9.4 show the relations that the heat flux and mass flux have on the assumed plate and CO_2 temperatures.

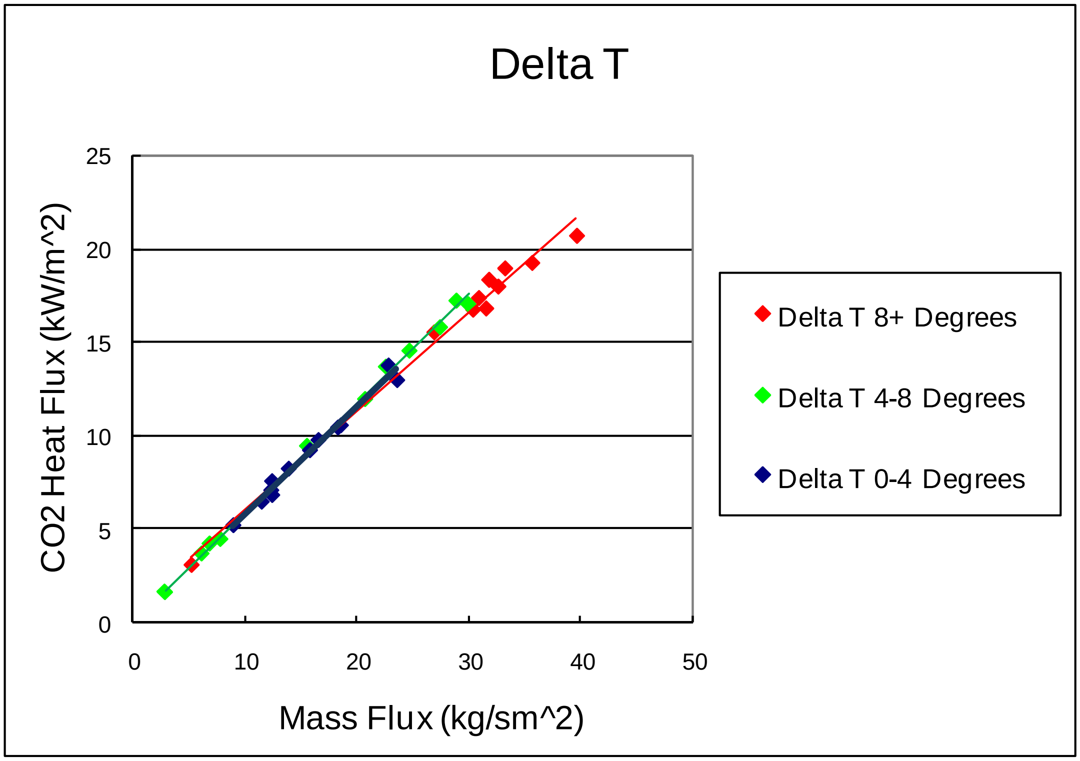

Figure 9.2 L plate delta T influencing mass fluxes and heat fluxes.

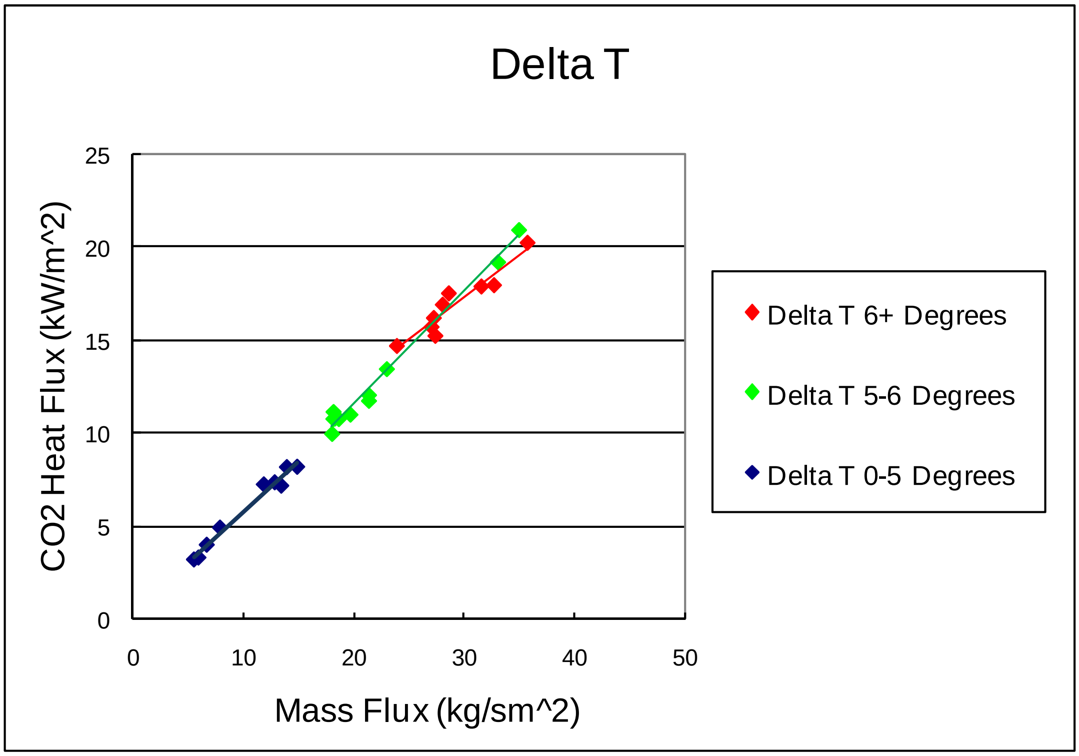

Figure 9.3 M plate delta T influencing mass fluxes and heat fluxes.

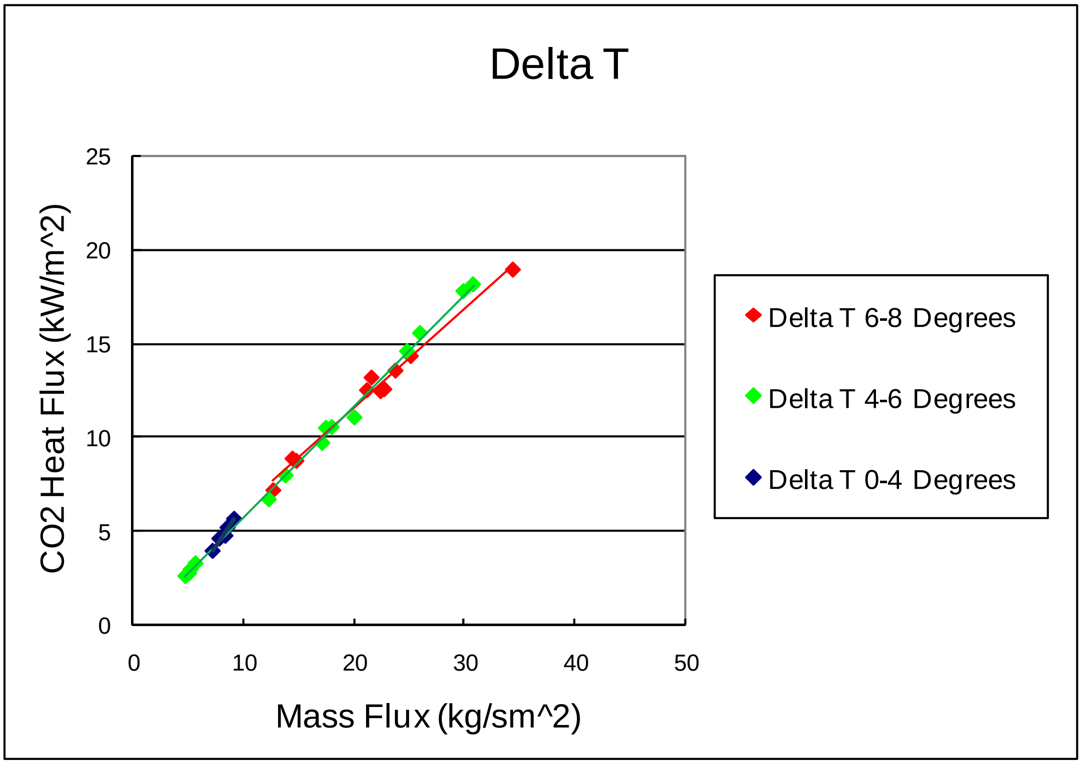

Figure 9.4 H plate delta T influencing mass fluxes and heat fluxes.

All three plates consistently show a strong correlation that low delta T temperatures are dominated by plate profile; the higher the profile, the range of heat flux and mass flux attenuates for delta T temperatures less than 4°C. However, when the delta T temperature is greater than 4°C, regardless of plate profile, both high and low mass and heat fluxes are observed.

9.3 Heat Transfer and Mass Flow

It is also useful to compare flow parameters with heat transfer coefficients. Figures 9.5 through 9.7 detail the relation that mass flow and heat transfer coefficients have one with another.

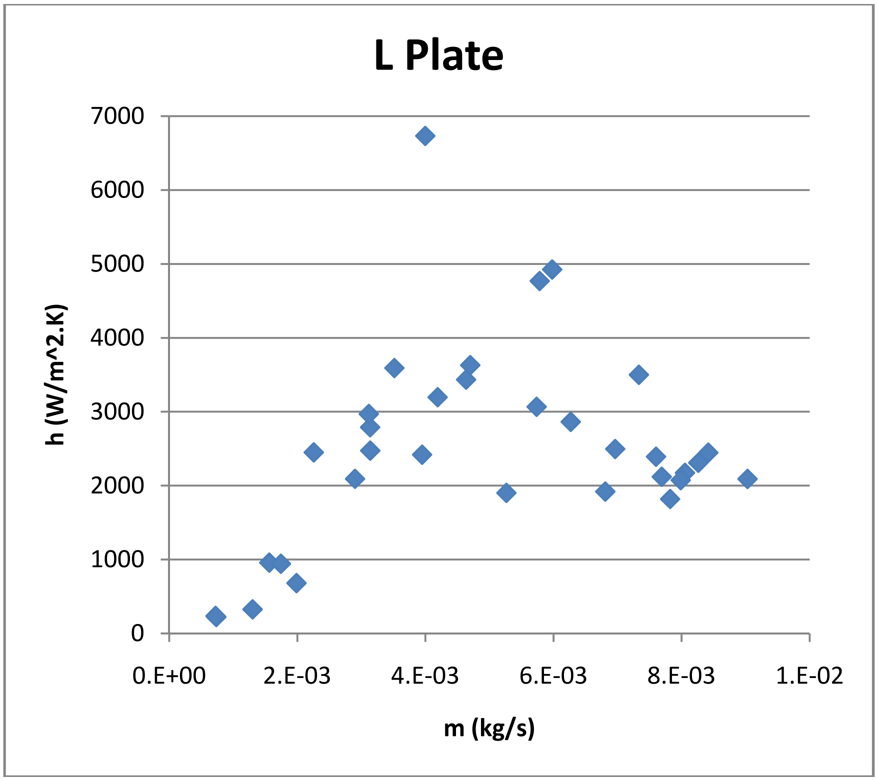

Figure 9.5 L plate heat transfer vs mass flow.

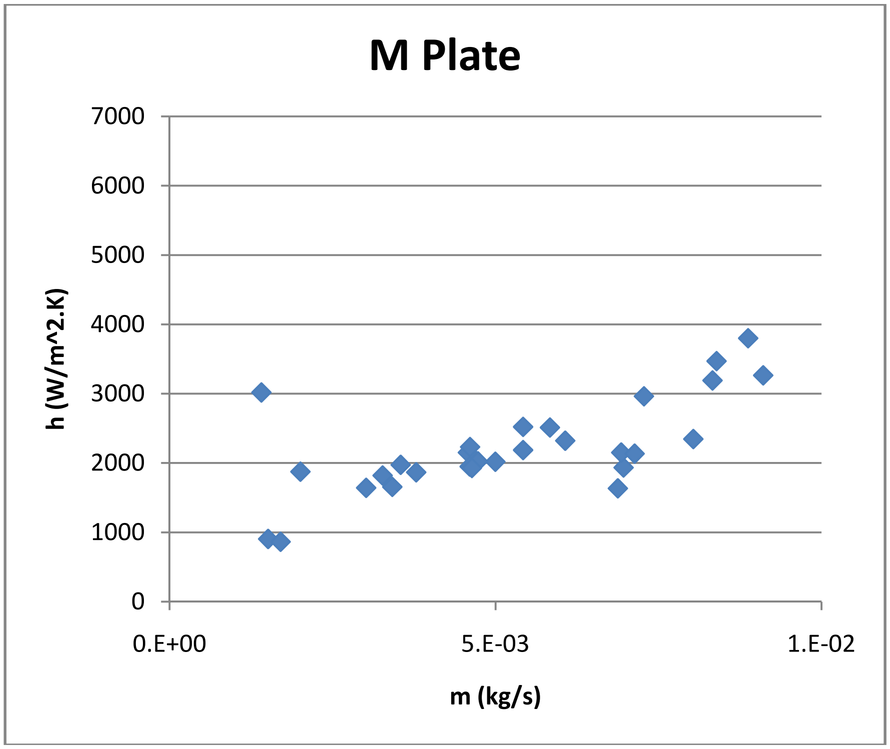

Figure 9.6 M plate heat transfer vs mass flow.

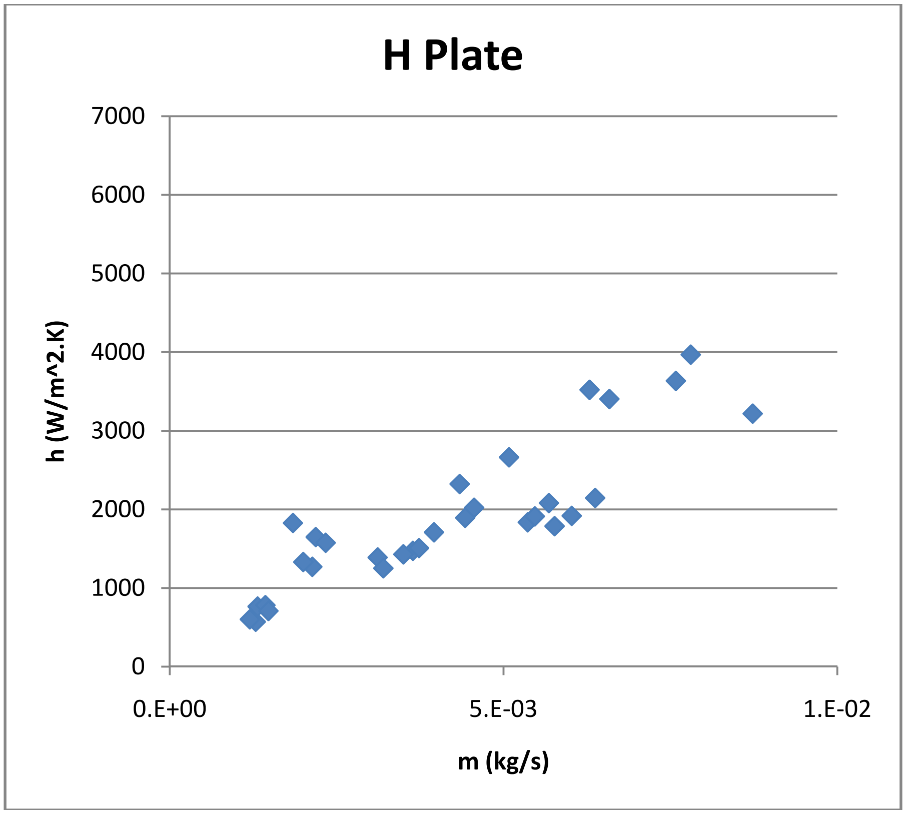

Figure 9.7 H plate heat transfer vs mass flow.

The scatter of the three plates' two-phase comparison of heat transfer and mass flow is larger than the scatter found in the single-phase data. This is due to the inherent characteristics of two-phase flow; as flow changes from one phase to another, properties such as viscosity, density and specific heat can change orders of magnitude. With these large changes in properties, it is less likely to achieve very linear data results. The overall heat transfer and mass trends of the H and M plates do show a strong correlation that as mass flow increases, the heat transfer will increase as well. The L plate however exhibits a larger scattering of data than that of the H and M plates after about 0.005 kg/s. This could be attributed to a transitional flow phenomenon that could occur in the plate at certain flow rates. These comparisons of the two-phase data will help in the dimensional analysis which will give specific correlations for each plate as to how CO_2 will condense at a given temperature and heat flux.

9.4 Two-Phase Pressure Drop

The pressure drop that occurs across the plates during the condensation process is shown in Figures 9.8 through 9.10. Pressure drops were low due to the low flow and effects of gravity helping the condensation process.

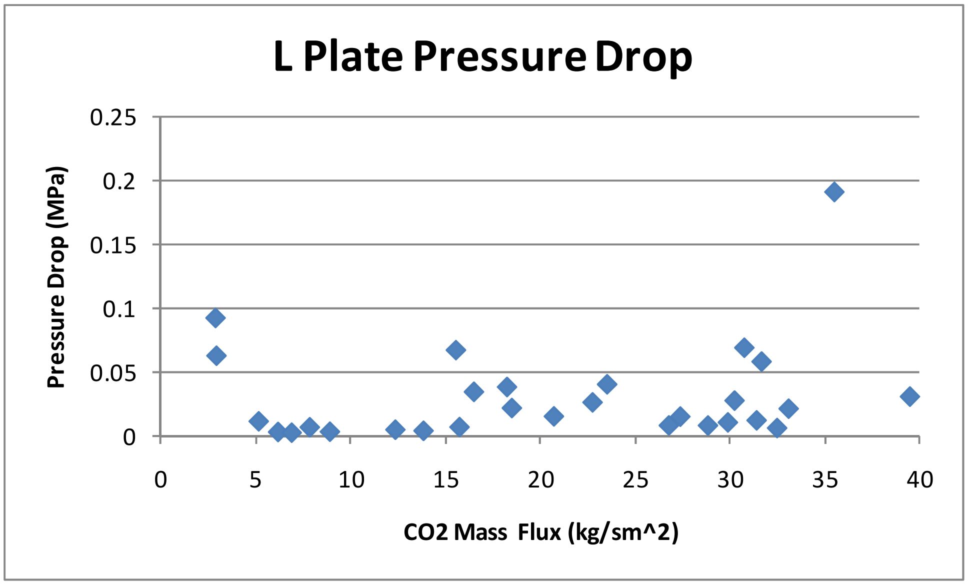

Figure 9.8 L plate pressure drops at various mass fluxes.

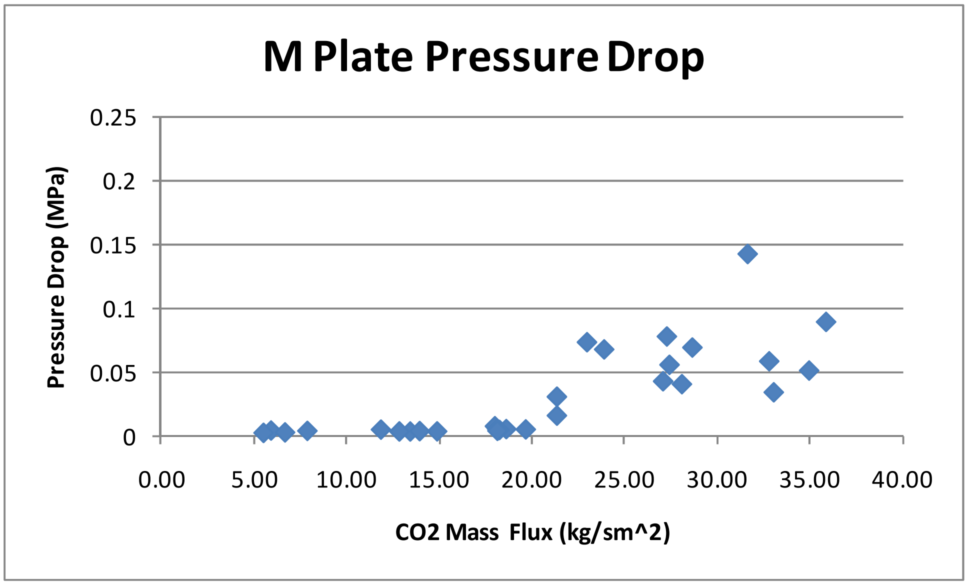

Figure 9.9 M plate pressure drops at various mass fluxes.

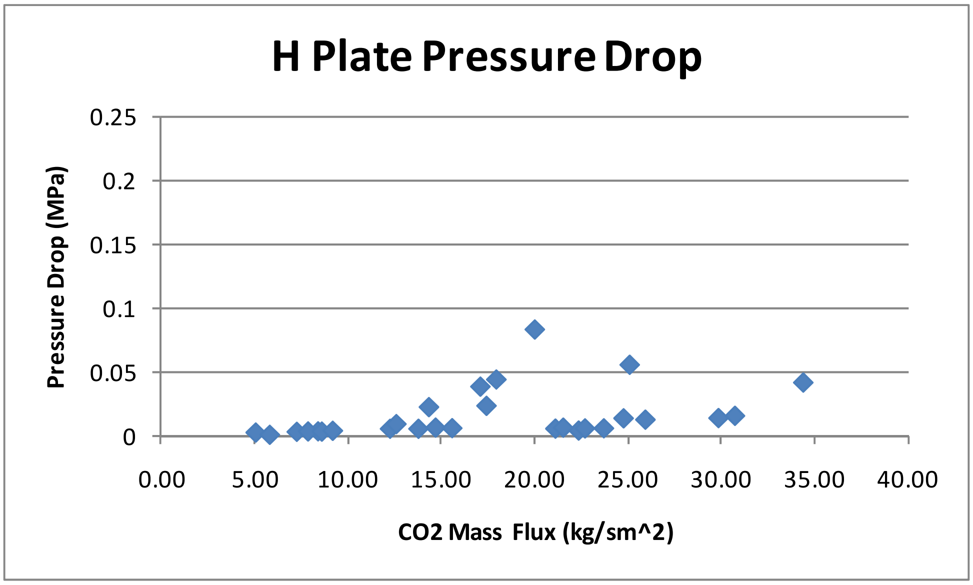

Figure 9.10 H plate pressure drops at various mass fluxes.

The pressure drop that is depicted in the previous three figures does not model the two-phase pressure drop only. It includes several contributing pressure drop factors, like those relating to gravity as well as the manifold regions of the system and the pressure drop in the sub cooled and superheated regimes of the plate. Generally for the three plates, for mass fluxes less than 15 kg/m^{2}s, the pressure drops are very minimal. This could be due to the gravitational effects of condensation being more influential than the flow from the pump. The pressure differences in the plates when the mass fluxes are greater than 15 kg/m^{2}s seem to fluctuate more and may be influenced less by the effects of gravity.

The pressure and mass flux comparisons are useful to be able to understand what regimes that laminar and turbulent flow may exist. When in laminar flow, pressure drops decrease as flow increases, so in the L plate plot Figure 9.8, the low flow pressure drop behavior could be a good indication that a laminar flow exists in flows less than 10 kg/m^{2}s. Then as flows increase to 15 kg/m^{2}s and greater, the pressure drops stay constant or increase, which is a characteristic of either transitional or turbulent flow. The M and H plates do not seem to exhibit a laminar flow in the tested flow ranges.

9.4 Analysis and Uncertainty

At this point, a proper two-phase dimensional analysis and uncertainty section would be appropriate, but as stated earlier, such activity is outside the scope of the current thesis. The two-phase dimensional analysis takes into account up to 10 to 20 variables in the heat transfer and pressure drop correlations. Since a dimensional analysis has not been completed, an uncertainty analysis also is out of the scope of the thesis, but common two-phase uncertainties are in the range of ±30-50%, and the uncertainties of the present study are anticipated to have similar uncertainty ranges.

CHAPTER 10 SUMMARY AND CONCLUSION

Three different brazed plate heat exchangers were studied in single-phase and two-phase experimentation. The equipment and facilities were explained in the research project as well as the setup using the equipment for both single and two-phase studies. Data collection and analysis were performed for both single and two-phase flows. The following sections detail the uncertainty analysis for the data collected, as well as thorough summary and stated conclusions for the study.

10.1 Summary

The importance of the current study of condensing carbon dioxide in brazed plate heat exchangers is identified at the beginning of this thesis. To date, there has been no reported literature on the condensation of carbon dioxide in brazed plate heat exchangers. The open review of literature in this thesis however, does discuss studies of carbon dioxide used as a refrigerant as well as condensation of other refrigerants in plate heat exchangers.

Equipment used during the experimentation processes of this study is summarized and schematics of how all the equipment was assembled were also shown. Each temperature, pressure and flow reading device used in the experimental facility has a detailed explanation as to why it was chosen and implemented in the setup.

For the first portion of the study, the single-phase loop setup describes how the instrumentation recorded data for both hot and cold water counter flow in the plates as well as hot water and dynalene counter flow. The data acquisition system is presented, and the single-phase experimental test procedure is explained. The modified Wilson plot technique is presented and used to find the single-phase heat transfer correlation coefficients, while the Fanning friction factor was used to find single-phase pressure drops for each plate. The final single-phase results were shown and the coefficients for water/water and dynalene/water heat transfer and pressure drop correlations are stated.

With the completed single-phase analysis, the two-phase schematic and setup of the experimentation is given, along with the test procedure to control the system and collect sound condensation data. A two-phase data reduction section explains in detail the three different regimes of flow occurring in the plate heat exchangers; vapor, saturated liquid vapor mixture, and liquid. These three regimes are used to properly calculate the heat transfer that takes place to fully condense the carbon dioxide. The two-phase results section presents comparisons of dimensionless heat transfer and flow characteristics in each plate. Condensation heat transfer coefficients are observed at various saturation temperatures and heat fluxes. Two-phase pressure drops for each of the plates are also discussed and presented in graphical forms.

10.2 Conclusions

Three brazed plate heat exchangers with different interior configuration, each consisting of three channels, were experimentally analyzed in this study. Both single-phase flow (water/water as well as dynalene/water) and two-phase condensation flow experimentation was carried out on each plate.

The resulting single-phase coefficients listed in Tables 6.1 and 6.2 to be used in their respective correlations were within reasonable range of standard deviation and uncertainty of less than 1.3% for the Fanning friction factor and less than 4.4% for heat transfer coefficients. These correlations were also compared with other well established studies on single-phase flow in plate heat exchangers. This comparison qualitatively showed good consistencies; however, differences were observed among different studies that could be explained due to several factors: (1) geometrical configuration of the plates, such as size, corrugation angle, pitch, and spacing were not exactly identical, (2) overall size and aspect ratio of the heat exchangers were different, (3) flow conditions and regimes were different, (4) thermal boundary conditions were not similar, and (5) thermo-hydrodynamic parameters, such as free flow and heat transfer areas, were not consistently defined and used. The latter looks to be a major issue on discrepancies among different studies on plate heat exchangers, which needs to be carefully and extensively investigated in the future. Although water/water and dynalene/water single-phase analyses were both completed, it is possible that only the coefficients from the water/water analysis will be necessary in the two-phase analysis. It is anticipated though that the dynanlene/water correlations will prove to be more accurate.

Comparing the data from the three plate heat exchangers in the two-phase condensation analysis shows that the data collection method was reliable. The heat transfer coefficients of the high profile plate are higher at any given flow than the mixed and low profile plates under the same flow conditions. The low profile plate exhibits heat transfer behavior that is more scattered than that of the other two profile plates. The flow in the L plate may be experiencing more of laminar or transitional flow regime, where the M and H plates are most likely transferring heat in the turbulent regime. The pressure drop for the plates may offer supporting arguments as to the possibility of different flows occurring in the plates. The pressure drop in the L plate at low flows behaves as a laminar flow, which same trend does not exist in the M and H plate at the same low flows. Both M and H plates show similar low flow behavior, where the pressure drop was minimal below 15 kg/m^2s and the pressure drops above this flow rate were noticeably higher. This behavior may demonstrate that at the low flow rates the effects of gravity on the condensing fluid overpowered the flow effects.

Future work would include a thorough two-phase dimensional and propagation of uncertainty analysis to be able to model the two-phase condensation of CO_2 in brazed plate heat exchangers. It is anticipated that the uncertainty of the two-phase correlations would lie within 30-50%.

The completed condensation of CO_2 in brazed plate heat exchangers study with correlations and an uncertainty analysis will be of great use to engineers and research in the future. Every step to better understand how to keep better care of the environment and our surroundings will have large dividends for the immediate and long term future of our planet.

REFERENCES

[1] Bodinus, W. S. “The Rise and Fall of Carbon Dioxide Systems: The First Century of Air Conditioning,” ASHRAE Journal, Vol. 41, No. 4, p 37, 1999.

[2] Pearson, A. “Carbon Dioxide-New Uses for an Old Refrigerant,” International Journal of Refrigeration, Vol. 28, pp. 1140-1148, 2005.

[3] UNEP (United Nations Environmental Programme), 2006 Report of the Refrigeration, Air Conditioning and Heat Pumps Technical Options Committee, p. 32, RTOC Assessment Report 2006.

[4] Halder, G.N. and Sarkar, S.C., “Scope of Carbon Dioxide as a Natural Refrigerant for Replacements of CFCs,” Journal of Energy in Southern Africa, Vol. 12, No. 3, pp. 408-411, 2001.

[5] Shah, R.K. and Wanniarachchi, A.S., “Plate Heat Exchanger Design Theory,” J.-M. Bushlin (Ed.), Industrial Heat Exchangers, Lecture Series #1991-04, Von Karman Institute for Fluid Dynamics, Belgium, 1992.

[6] Robinson, D. M. and Groll, E. A., “Heat Transfer Analysis of Air-to-Carbon Dioxide Two-Phase Heat Absorption and Supercritical Heat Rejection,” HAVAC&R Research, Oct, Vol. 4, No. 4, pp. 327-344, 1998.

[7] Pettersen, J., Hafner, A., Skaugen, G. and Rekstad, H., “Development of Compact Heat Exchangers for CO_2 Air-Conditioning Systems,” International Journal of Refrigeration, Vol. 25, No. 3, pp. 180-193, 1998.

[8] Kim, S.G. and Kim, M.S., “Experiment and Simulation on the Performance of an Autocascade Refrigeration System Using Carbon Dioxide as a Refrigerant,” International Journal of Refrigeration, Vol. 25, pp. 1093-1101, 2002.

[9] Raush, G., Rigola, J., Perez-Segarra C.D. and Oliva, A., “Thermal and Fluid Dynamic Behavior of a Trans-Critical Carbon Dioxide Small Cooling System: Experimental

Investigation," International Conference on Compressors and their Systems, Sept. 4-7, pp. 293-300, 2005.

[10] Rigola, J., Perez-Segarra, C.D., Oliva, A. and Raush, G., "Thermal and Fluid Dynamic Behavior of a Trans-Critical Carbon Dioxide Small Cooling System: Numerical Analysis,' International Conference on Compressors and their Systems, Sept 4-7, pp. 301-309, 2005.

[11] Brown, M., Rosario L. and Rahman M. M., "Thermodynamic Analysis of Transcritical Carbon Dioxide Cycles," AES, Vol. 45, pp. 59-70, 2005.

[12] Hwang, Y., Radermacher, R., Jin, D. and Hutchins, J. W., "Performance Measurement of CO_2 Heat Exchangers," ASHRAE Transactions, Vol. 111, Part 2, pp. 306-316, 2005.

[13] Rigola, J., Perez-Segarra, C.D., Oliva, A. and Raush G., "Numerical Simulation and Experimental Validation of Vapour Compression Systems," Special emphasis on CO_2 Trans-Critical Cycles, International Journal of Refrigeration, Vol. 28, pp. 1225-1237, 2005.

[14] Ayub, Z.H., "Plate Heat Exchanger Literature Survey and New Heat Transfer and Pressure Drop Correlations for Refrigerant Evaporators," Heat Transfer Engineering, Vol. 24, No. 5, pp. 8-12, 2003.

[15] Kumar, H., "The Plate Heat Exchanger: Construction and Design," Institute of Chemical Engineering Symposium Series, No. 86, pp. 1275-1288, 1984.

[16] Focke, W.W., Zacharides, J., and Oliver, I., "The Effect of the Corrugation Inclination Angle on the Thermohydraulic Performance of Plate Heat Exchangers," International Journal of Heat and Mass Transfer, Vol. 28, No. 8, pp. 1469-1479, 1985.

[17] Thonon, B., "Design Method for Plate Evaporators and Condensers," 1st International Conference on Process Intensification for the Chemical Industry, BHR Group Conference Series Publication, No.18, pp. 37-47, 1995.

[18] Würfel, R. and Ostrowski, N., "Experimental Investigations of Heat Transfer and Pressure Drop During the Condensation Process Within Plate Heat Exchangers of the Herringbone-Type," International Journal of Thermal Sciences, Vol. 43, pp. 59-68, 2004.

[19] Panchal, C. B., “Condensation Heat Transfer in Plate Heat Exchangers,” American Society of Mechanical Engineers, Heat Transfer Division, Vol. 44, pp. 45-52, 1985.

[20] Tovazhnyanski, L. L. and Kapustenko, P. A., “Intensification of Heat and Mass Transfer in Channels of Plate Condensers,” Chemical Engineering Communications, Vol. 31, No. 1-6, Dec., pp. 351-366, 1984.

[21] Wang, Z., and Zhao Z., “Analysis of Performance of Steam Condensation Heat Transfer and Pressure Drop in Plate Condensers,” Heat Transfer Engineering, Vol. 14, No. 4, pp. 32-41, 1993.

[22] Arman, B. and Rabas, T. J., “Condensation Analysis for Plate-Frame Heat Exchangers,” National Heat Transfer Conference, ASME 1995, Vol. 12, pp. 97-104, 1995.

[23] Yan, Y., Lio, H. and Lin T., “Condensation Heat Transfer and Pressure Drop of Refrigerant R-134a in a Plate Heat Exchanger,” International Journal of Heat and Mass Transfer, Vol. 42, pp. 933-1006, 1999.

[24] Jokar, A., Hosni, M. H. and Eckels, S. J., “Dimensional Analysis on the Evaporation and Condensation of Refrigerant R-134a in Minichannels Plate Heat Exchangers,” Applied Thermal Engineering, Vol. 25, pp. 2287-2300, 2006.

[25] Longo, G.A. and Gasparella, A., “Heat Transfer and Pressure Drop During Hfc-134a Condensation Inside a Commercial Brazed Plate Heat Exchanger,” International Congress of Refrigeration, Beijing. 2007

[26] Longo, G.A., Gasparella, A. and Sartori, R., “Experimental Heat Transfer Coefficients During Refrigerant Vaporization and Condensation Inside Herringbone-Type Plate Heat Exchangers with Enhanced Surfaces,” International Journal of Heat and Mass Transfer, Vol. 47, pp. 4125-4136, 2004.

[27] Kedzierski, M. A., “Effect of Inclination on the Performance of a Compact Brazed Plate Condenser and Evaporator,” Heat Transfer Engineering, Vol. 18, No. 3, Jul-Sep, pp. 25-38, 1997.

[28] Yan, Y., Lio, H. and Lin T., "Condensation Heat Transfer and Pressure Drop of Refrigerant R-134a in a Plate Heat Exchanger," International Journal of Heat and Mass Transfer, Vol. 42, pp. 933-1006, 1999.

[29] Hsieh, Y.Y. and Lin T.F., "Saturated Flow Boiling Heat Transfer and Pressure Drop of Refrigerant R410a in a Vertical Plate Heat Exchanger," International Journal of Heat Mass Transfer, Vol. 42, pp. 993-1006, 2002.

[30] Han, D., Lee, K. and Kim, Y., "Experiments on the Characteristics of Evaporation of R410a in Brazed Plate Heat Exchangers with Different Geometric Configurations," Applied Thermal Engineering, Vol. 23, No.10, July, pp. 1209-1225, 2003.

[31] Claesson, J., "The Influence of Brine Flow on the Flow Boiling Refrigerant Heat Transfer Coefficient in a Compact Brazed Plate Heat Exchanger," International Journal of Heat Exchangers, Vol. 6, No. 1, June, pp. 35-54, 2005.

[32] Sterner, D. and Sunden B., "Performance of Plate Heat Exchangers for Evaporation of Ammonia," Heat Transfer Engineering, Vol. 27, No. 5, June, pp. 45-55, 2006.

[33] Incropera, F.P. and DeWitt, D. P., *Fundamentals of Heat and Mass Transfer*, 5th Ed., John Wiley & Sons, New Jersey, 2002.

[34] Briggs, D.E. and Young, E.H., "Modified Wilson Plot Techniques for Obtaining Heat Transfer Correlations for Shell and Tube Heat Exchangers," Chemical Engineering Progress Symposium, AIChE Heat Transfer-Philadelphia Vol. 65, No. 92, pp. 35-45, 1969.

APPENDIX-A: MINIMUM FREE FLOW AREA CALCULATIONS

Utilizing computer modeling software can shed extra light on the minimum free flow area (MFFA) in the brazed plate heat exchangers under study. With parametric modeling it is possible to better estimate the area based not only on average plate spacing, but also corrugation pitch and chevron angle. As Figures A.1 through A.3 show, the three plates have different corrugations pitches and the angles by which the plates meet, giving different geometries for which fluid to flow through.

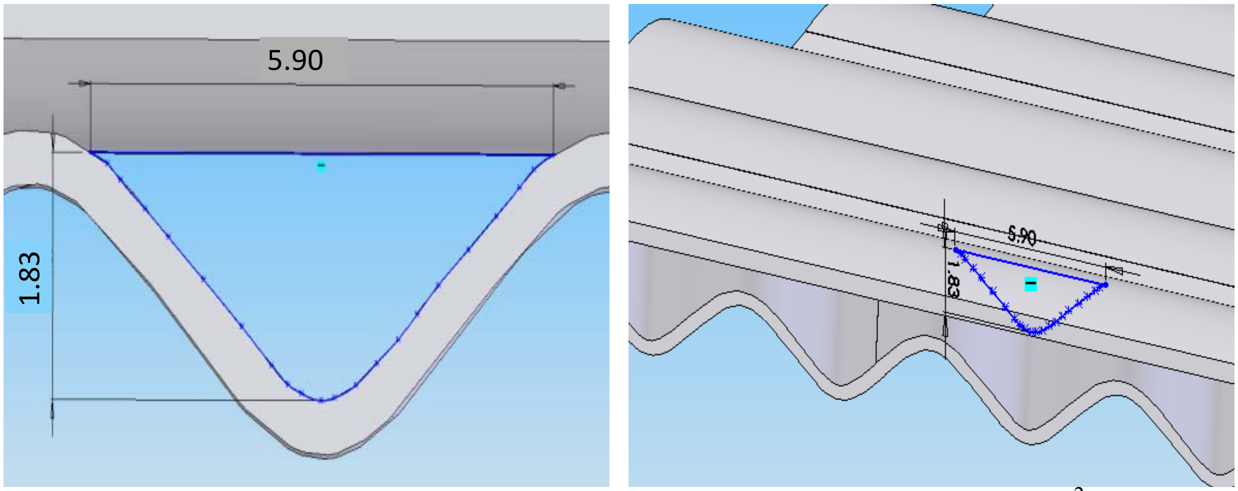

Figure A.1 H Plate 27/27, Corrugation Pitch=6.03 mm, $A_{onePass}$=5.7 mm^2

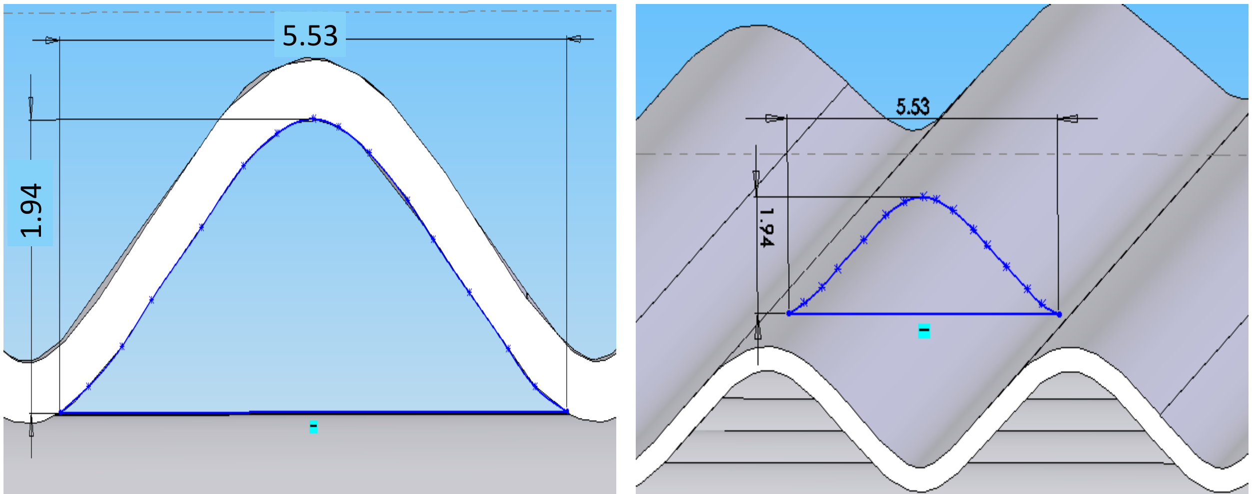

Figure A.2 M Plate 27/60, Corrugation Pitch=6.19 mm, $A_{onePass}$=5.8 mm^2

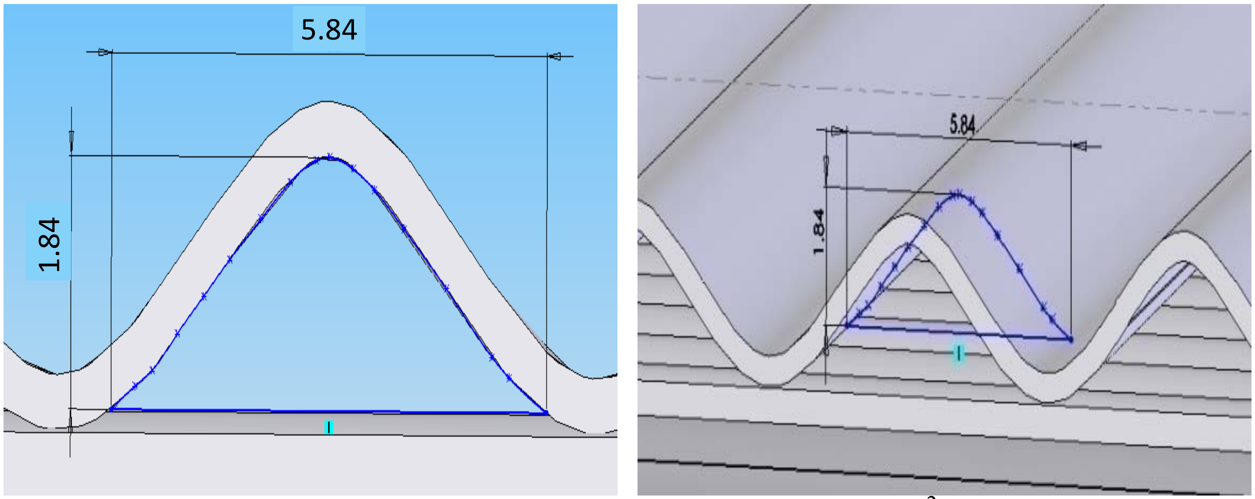

Figure A.3 L Plate 60/60, Corrugation Pitch=6.27 mm, $A_{onePass}$=5.7 mm^2

Although the three different plates demonstrate different corrugation pitches and angles, the individual passes all seem to have similar areas, 5.7 mm to 5.8 mm on average. When taking into account *all* the individual passes collectively, Figures A.4 through A.6 show that at any given cross section for the different plates, the three plates' minimum free flow areas are dissimilar. See also Table A.1.

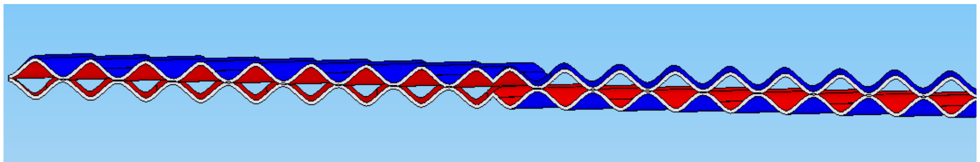

Figure A.4 L Plate 34 passes at 5.75mm^2 each. Minimum Free Flow Area=195.5 mm^2

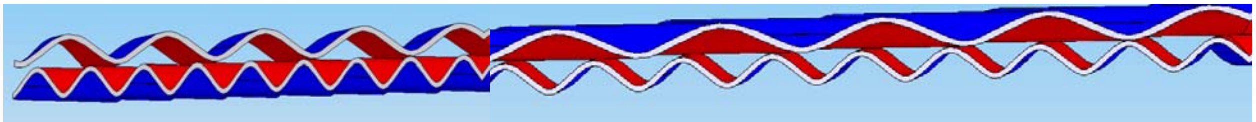

Figure A.5 M Plate 26 passes at 5.75mm^2 each. Minimum Free Flow Area=149.5mm^2

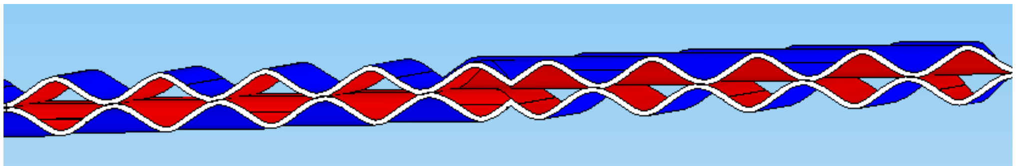

Figure A.6 H plate 18 passes at 5.75 mm^2 each. Minimum Free Flow Area=103.5mm^2

Table A.1 Brazed plate heat exchanger dimensions

Plate Designation	Chevron Angle, °	Corrugation Pitch, mm	Passes Across Width of Plate	Minimum Free Flow Area, mm^2 (in^2)	b*w Area, mm^2 (in^2)
8964 H	27/27	6.03	18	103.5	254
9866 M	27/60	6.19	26	149.5	254
8965 L	60/60	6.27	34	195.5	254

Instead of having to model each plate in the future to find the minimum free flow area, the following formulation is proposed.

$$A_o = f\left(\beta, \lambda, w, A_{onePass}\right) \tag{A-1}$$

$$A_o = \frac{2(0.000095\beta^2 - 0.0074\beta + 1.0716)w\sin(\pi\beta/180)}{\lambda} * A_{onePass} \tag{A-2}$$

where β (in degrees) is the average of the chevron angled plates from the horizontal axis of the vertically installed exchanger.

Setting the definitions of the geometries of the plates, such as minimum free flow area and hydraulic diameter, is essential in accurately analyzing the pressure drop and heat transfer of brazed plate heat exchangers. In fact, calculating the minimum free flow area corresponds to the maximum flow velocity in the channels. This velocity in turn can characterize the Reynolds number and flow regimes in the brazed plate heat exchanger. It was found that the conventional flow area, b*w, is 1.3 to 2.5 times the minimum free flow area, Equation A-2, for the three brazed plate heat exchangers in this study. This leads to an augmentation in Reynolds numbers of 30 to 150% between the two methods, which can represent different flow regimes.

The resulting heat transfer coefficients utilizing the MFFA method are shown in Table A-2.

Table A.2 Current study- modified single-phase heat transfer correlations based on MFFA

$$Nu=C.Re^{P}.Pr^{(1/3)}.(\mu/\mu_s)^{0.14}$$

water/ water	60/60 Plate	27/60 Plate	27/27 Plate
C_h	0.111	0.148	0.124
P	0.715	0.702	0.729

dynalene/ water	60/60 Plate	27/60 Plate	27/27 Plate
C_c	0.147	0.182	0.288
P	0.748	0.760	0.733

While the Reynolds number exponents do not deviate substantially from the b*w method, the cold and hot coefficients do (by as much as 94%) yielding discrepancies in the relationships between Nu and Re.

Further study and consideration is recommended to be able to standardize the measurements of the intricate and complex inner geometries of brazed plate heat exchangers.

APPENDIX-B: EQUIPMENT INFORMATION SHEETS

Information of the experimental equipment used in the single-phase and two-phase studies is detailed in this section.

B.1 Chiller

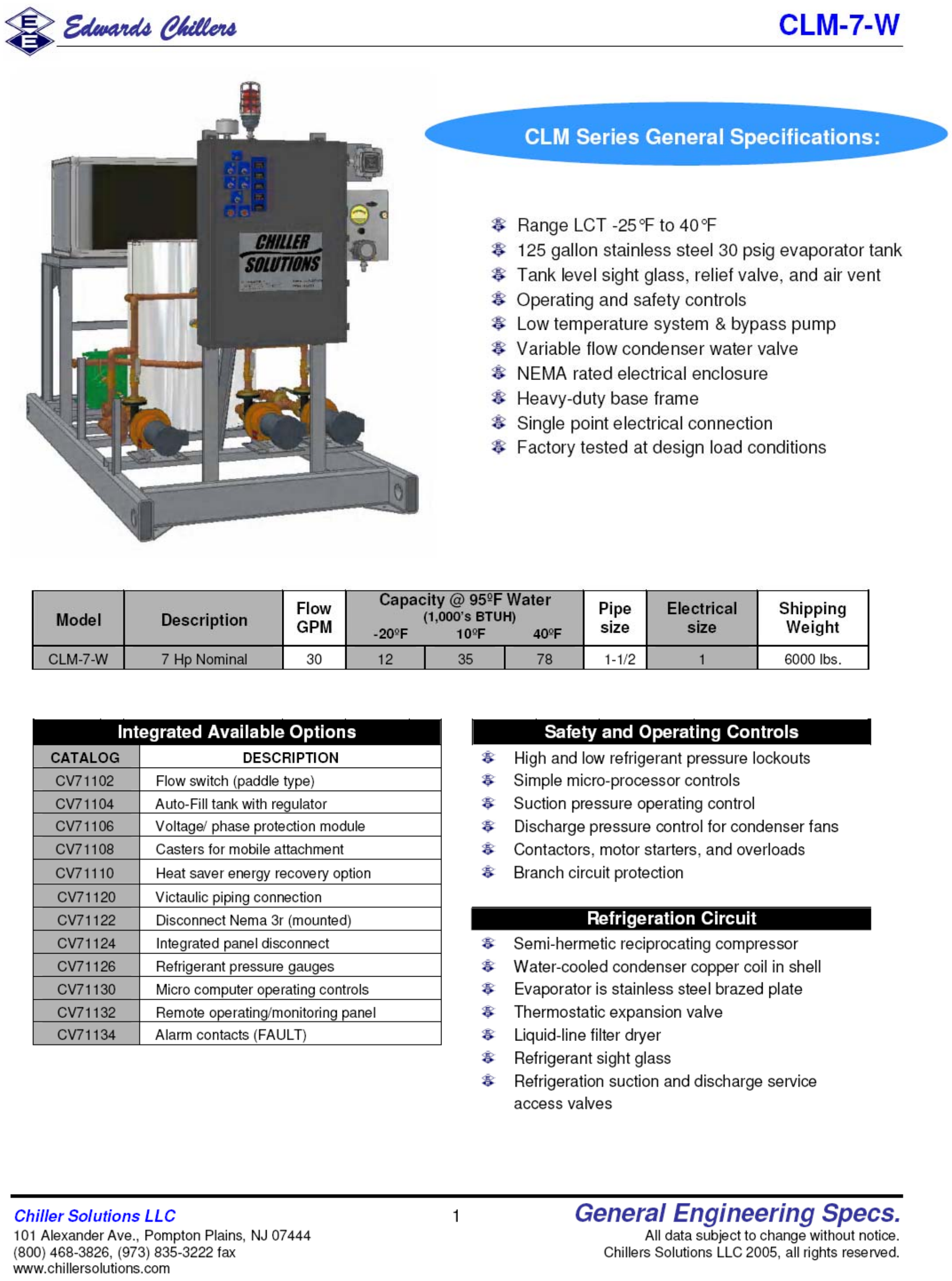

Edwards Chillers

CLM-7-W

CLM Series General Specifications:

- Range LCT -25°F to 40°F
- 125 gallon stainless steel 30 psig evaporator tank
- Tank level sight glass, relief valve, and air vent
- Operating and safety controls
- Low temperature system & bypass pump
- Variable flow condenser water valve
- NEMA rated electrical enclosure
- Heavy-duty base frame
- Single point electrical connection
- Factory tested at design load conditions

Model	Description	Flow GPM	Capacity @ 95ºF Water (1,000's BTUH) -20ºF	10ºF	40ºF	Pipe size	Electrical size	Shipping Weight
CLM-7-W	7 Hp Nominal	30	12	35	78	1-1/2	1	6000 lbs.

Integrated Available Options

CATALOG	DESCRIPTION
CV71102	Flow switch (paddle type)
CV71104	Auto-Fill tank with regulator
CV71106	Voltage/ phase protection module
CV71108	Casters for mobile attachment
CV71110	Heat saver energy recovery option
CV71120	Victaulic piping connection
CV71122	Disconnect Nema 3r (mounted)
CV71124	Integrated panel disconnect
CV71126	Refrigerant pressure gauges
CV71130	Micro computer operating controls
CV71132	Remote operating/monitoring panel
CV71134	Alarm contacts (FAULT)

Safety and Operating Controls

- High and low refrigerant pressure lockouts
- Simple micro-processor controls
- Suction pressure operating control
- Discharge pressure control for condenser fans
- Contactors, motor starters, and overloads
- Branch circuit protection

Refrigeration Circuit

- Semi-hermetic reciprocating compressor
- Water-cooled condenser copper coil in shell
- Evaporator is stainless steel brazed plate
- Thermostatic expansion valve
- Liquid-line filter dryer
- Refrigerant sight glass
- Refrigeration suction and discharge service access valves

Chiller Solutions LLC
101 Alexander Ave., Pompton Plains, NJ 07444
(800) 468-3826, (973) 835-3222 fax
www.chillersolutions.com

1

General Engineering Specs.
All data subject to change without notice.
Chillers Solutions LLC 2005, all rights reserved.

Refrigeration System

Each compressor system has a suction pressure control, condenser automatic head pressure controls, low suction safety control, and high discharge safety control.

Each refrigeration system has semi-hermetic reciprocating compressor, automatic head pressure control, evaporator, stainless steel storage tank, and temperature controls. The refrigerant circuit is pressure tested, evacuated, dehydrated, and charged with refrigerant. The refrigeration system uses one system pump to circulate the water to and from the chiller.

(Consult the Piping and Instrumentation Diagram for more information)

Compressors

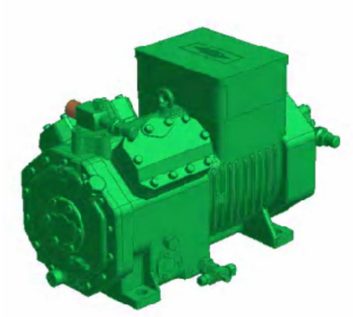

The semi-hermetic R-507 reciprocating compressor is controlled with high and low pressure operating controls. The compressor contains a piston, intake valve, exhaust valve, and motor all housed in a hermetically sealed casing. The 1750 RPM motor is suction gas cooled. The piston's down stroke creates a vacuum in the cylinder and suction line pressure forces the intake valve to open allowing refrigerant gas to enter the cylinder. Discharge gas line pressure holds the discharge valve closed. The piston's up stroke increases pressure in the cylinder allowing refrigerant gas to open the exhaust valve and be discharged to the condenser. Suction line pressure holds the intake valve closed.

Water Cooled Condenser

The water-cooled condenser is used to remove the heat from the heat of absorption and added mechanical heat. The condenser is a compact coil and shell style heat exchanger. The water enters the top of the heat exchanger where it travels through two independent copper tubes which are coiled to fit into the shell. The interior of these water tubes is rifled causing additional turbidity, thus enhancing heat transfer. The exterior of these water tubes incorporates an enhanced fin surface creating fine channels. The refrigerant is forced through these channels maximizing the contact of the refrigerant to the heat exchange surface. The coil fits neatly around an interior stay pipe and then is wrapped in a heavy steel shell, with the tubes penetrating the shell through the front. The heat exchanger is fully welded and tested.

Evaporator

The evaporator is a compact WTT America 316L stainless steel heat exchanger. The heat exchanger consists of stainless steel embossed plates stacked so that every other plate is rotated 180°. The spaces between the plates form the channels for the refrigerant and the coolant. Between every two plates is a thin foil of cooper. When heat in a vacuum is applied to the heat exchanger the copper is melted and is drawn into all the plate contact points and seams. The heat exchanger is fully pressure tested.

Evaporator Storage Tank

The welded fluid storage tank consists of a 14 gauge type 304 stainless steel shell with 7 gauge 304 stainless steel heads. The tank is fully insulated with ¾" Armaflex insulation. The non-coded tank is complete with a 30 psig pressure relief valve, tank level sight glass, drain valve, and air vent. The tank includes welded nozzles, at an appropriate size, for supply and return. The tank will also include a series of stainless steel structural stay pipes which serve to reinforce the top and bottom of the tank. The evaporator is welded to the tank center stay pipe and immersed in the tank. It is piped to the exterior of the tank utilizing welded sleeves and bronze brazing techniques. The entire assembly is factory pressure tested (refrigeration 400 psig, tank at 45 psig) prior to final assembly.

Electrical

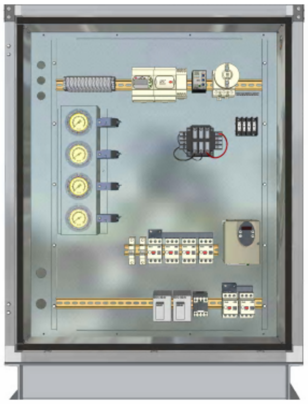

The electrical components in the chiller will be mounted in a NEMA rated enclosure. The enclosure shall have a hinged access door to the electrical control panel. The enclosure contains all motor protectors, contactors, transformers, controls, and relays. All components and wiring are U.L. listed and meet or exceed NEC standards.

The chiller is complete with single point wiring to the main tie in block, with access though an opening provided on the side of the chiller. The electrical box and interior of the chiller are weatherproof by means of neoprene gaskets around all accessible openings. ***(Consult wiring diagram for more information.)***

Chiller Base Frame and Cabinetry

The compressor, evaporator, condenser, tank, and pump are mounted on a heavy duty steel welded channel base frame. This base frame is two part epoxy coated and provides superior corrosion resistance, while also providing structural rigidity for many seismic isolation requirements.

Composite Views of a Typical Low Temperature Chiller

Air Cooled Unit Shown
Redundant System Pumps and Compressors

B.2 CO_2 Pump

Series CP200

Triplex Ceramic Plunger Pump Operating Instructions/ Repair and Service Manual

---

For Models:
CP218
CP219
CP220
CP230

GIANT

Updated 10/02

Contents:

Specifications
Model CP230

Ratings	0.5 GPM (1.9 lm) @ 2030 PSI (139 bar)
Inlet Pressure	14 (0.9 bar) to 140 PSI (9.7 bar)
RPM	Up to 750 RPM
Plunger Diameter	18mm
Stroke	3.4mm
Temperature of Pumped Fluids	-40°F (-40 °C)to 160°F (71 °C)
Inlet Ports	(2) 3/8" BSPP
Discharge Ports	(2) 3/8" BSPP
Shaft Rotation	Top of Pulley Towards Fluid End
Crankshaft Diameter	24mm
Key Width	8mm
Shaft Mounting	Right Side Facing Manifold
Weight	11 lbs. 11oz. (5.4 kg)
Crankcase Oil Capacity	7.5 fl.oz. (222 ml)
Extended Crankcase Oil Capacity	9.0 fl.oz. (266 ml)

+Positive inlet pressure required

Consult the factory for special requirements that must be met if the pump is to operate beyond one or more of the limits specified above.

PULLEY INFORMATION

Pulley selection and pump speed are based on a 1725 RPM motor and "B" section belts. When selecting desired GPM, allow for a ±5% tolerance on pumps output due to variations in pulleys, belts and motors among manufacturers.

1. Select GPM required, then select appropriate motor and pump pulley from the same line.
2. The desired pressure is achieved by selecting the correct nozzle size that corresponds with the pump GPM.

HORSEPOWER INFORMATION

Horsepower ratings shown are the power requirements for the pump. Gas engine power outputs must be approximately twice the pump power requirements shown above.

We recommend that a 1.1 service factor be specified when selecting an electric motor as the power source. To compute specific pump horsepower requirements, use the following formula:

$$\frac{\text{GPM X PSI}}{1450} = \text{hp}$$

CP230 PULLEY SELECTION & HORSEPOWER REQUIREMENTS

PUMP PULLEY	MOTOR PULLEY	RPM	GPM	500 PSI	1000 PSI	1500 PSI	2030 PSI
7.75	2.35	200	0.1	0.0	0.1	0.1	0.1
7.75	3.30	300	0.2	0.1	0.1	0.2	0.3
7.75	4.30	400	0.3	0.1	0.2	0.3	0.4
7.75	5.30	500	0.3	0.1	0.2	0.3	0.4
7.75	6.30	600	0.4	0.1	0.3	0.4	0.6
7.75	7.75	750	0.5	0.2	0.3	0.5	0.7

B.3 Temperature Reading Devices

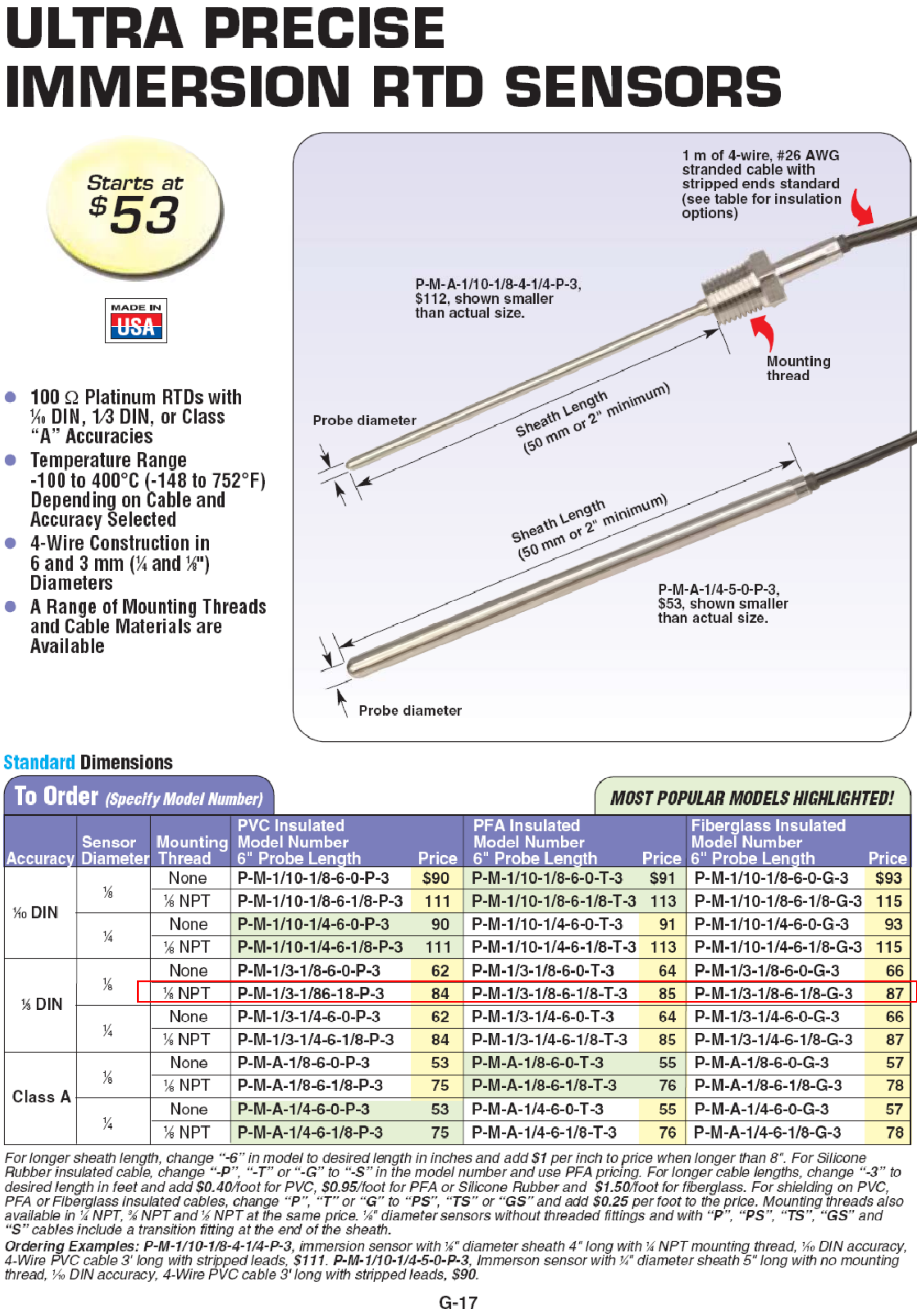

ULTRA PRECISE IMMERSION RTD SENSORS

- 100 Ω Platinum RTDs with ¹⁄₁₀ DIN, 1⁄3 DIN, or Class "A" Accuracies
- Temperature Range -100 to 400°C (-148 to 752°F) Depending on Cable and Accuracy Selected
- 4-Wire Construction in 6 and 3 mm (¼ and ⅛") Diameters
- A Range of Mounting Threads and Cable Materials are Available

Standard Dimensions

To Order *(Specify Model Number)*

MOST POPULAR MODELS HIGHLIGHTED!

Accuracy	Sensor Diameter	Mounting Thread	PVC Insulated Model Number 6" Probe Length	Price	PFA Insulated Model Number 6" Probe Length	Price	Fiberglass Insulated Model Number 6" Probe Length	Price
¹⁄₁₀ DIN	⅛	None	P-M-1/10-1/8-6-0-P-3	$90	P-M-1/10-1/8-6-0-T-3	$91	P-M-1/10-1/8-6-0-G-3	$93
		⅛ NPT	P-M-1/10-1/8-6-1/8-P-3	111	P-M-1/10-1/8-6-1/8-T-3	113	P-M-1/10-1/8-6-1/8-G-3	115
	¼	None	P-M-1/10-1/4-6-0-P-3	90	P-M-1/10-1/4-6-0-T-3	91	P-M-1/10-1/4-6-0-G-3	93
		⅛ NPT	P-M-1/10-1/4-6-1/8-P-3	111	P-M-1/10-1/4-6-1/8-T-3	113	P-M-1/10-1/4-6-1/8-G-3	115
⅓ DIN	⅛	None	P-M-1/3-1/8-6-0-P-3	62	P-M-1/3-1/8-6-0-T-3	64	P-M-1/3-1/8-6-0-G-3	66
		⅛ NPT	P-M-1/3-1/86-18-P-3	84	P-M-1/3-1/8-6-1/8-T-3	85	P-M-1/3-1/8-6-1/8-G-3	87
	¼	None	P-M-1/3-1/4-6-0-P-3	62	P-M-1/3-1/4-6-0-T-3	64	P-M-1/3-1/4-6-0-G-3	66
		⅛ NPT	P-M-1/3-1/4-6-1/8-P-3	84	P-M-1/3-1/4-6-1/8-T-3	85	P-M-1/3-1/4-6-1/8-G-3	87
Class A	⅛	None	P-M-A-1/8-6-0-P-3	53	P-M-A-1/8-6-0-T-3	55	P-M-A-1/8-6-0-G-3	57
		⅛ NPT	P-M-A-1/8-6-1/8-P-3	75	P-M-A-1/8-6-1/8-T-3	76	P-M-A-1/8-6-1/8-G-3	78
	¼	None	P-M-A-1/4-6-0-P-3	53	P-M-A-1/4-6-0-T-3	55	P-M-A-1/4-6-0-G-3	57
		⅛ NPT	P-M-A-1/4-6-1/8-P-3	75	P-M-A-1/4-6-1/8-T-3	76	P-M-A-1/4-6-1/8-G-3	78

*For longer sheath length, change "**-6**" in model to desired length in inches and add **$1** per inch to price when longer than 8". For Silicone Rubber insulated cable, change "**-P**", "**-T**" or "**-G**" to "**-S**" in the model number and use PFA pricing. For longer cable lengths, change "**-3**" to desired length in feet and add **$0.40**/foot for PVC, **$0.95**/foot for PFA or Silicone Rubber and **$1.50**/foot for fiberglass. For shielding on PVC, PFA or Fiberglass insulated cables, change "**P**", "**T**" or "**G**" to "**PS**", "**TS**" or "**GS**" and add **$0.25** per foot to the price. Mounting threads also available in ¼ NPT, ⅜ NPT and ½ NPT at the same price. ⅛" diameter sensors without threaded fittings and with "**P**", "**PS**", "**TS**", "**GS**" and "**S**" cables include a transition fitting at the end of the sheath.*

***Ordering Examples:** **P-M-1/10-1/8-4-1/4-P-3**, immersion sensor with ⅛" diameter sheath 4" long with ¼ NPT mounting thread, ¹⁄₁₀ DIN accuracy, 4-Wire PVC cable 3' long with stripped leads, **$111**. **P-M-1/10-1/4-5-0-P-3**, Immerson sensor with ¼" diameter sheath 5" long with no mounting thread, ¹⁄₁₀ DIN accuracy, 4-Wire PVC cable 3' long with stripped leads, **$90**.*

G-17

Interchangeability in °C			
Temp °C	Class A	⅓ DIN	⅒ DIN
-50	0.25	0.18	
0	0.15	0.10	0.03
100	0.35	0.27	0.08
200	0.55	0.43	
250	0.65	0.52	
300	0.75		
350	0.85		
400	0.95		
450	1.05		

Cable Options Temperature Range	
PVC Insulated	-50 to 100°C (-58 to 212°F)
PFA Insulation	-50 to 250°C (-58 to 482°F)
Fiberglass Insulation	-50 to 400°C (-58 to 753°F)
Silicone Insulated	-50 to 200°C (-58 to 392°F)

Photo by Craig Terry, courtesy of
Chemical Engineering Program at Rowan University

Omega's Ultra-Precise RTD sensors are used in a wide variety of applications where accuracy and precise temperature measurement means the difference between failure and success. Why not join the growing list of customers utilizing the best the market has to offer?

Rugged Transition Joint Probes
With Standard Dimensions

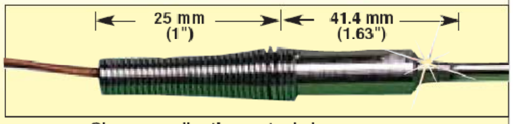

Shown smaller than actual size.

Note: See page A-79 for probe terminations. Please see page A-131 for compression fittings.

- ✓ **304 SS, 310 SS, 316 SS, 321 SS, Inconel or Super OMEGACLAD® XL Sheath**
- ✓ **Diameters from 1/16 to ¼"**
- ✓ **40" PFA Coated Stranded Lead Wire: 20 AWG for 3/16 and ¼" OD, 24 AWG for 1/16 and ⅛" OD Probes**
- ✓ **Cal-5 Available**

OMEGA® heavy duty transition joint probes offer convenient termination to PFA coated lead wire. The transition joint is 1.63" long, with a 1" spring for strain relief. The joint diameter is ¼" for 1/16 and ⅛" Dia. probes, ⅜" for 3/16 and ¼" Dia. probes.

Dual Element TJ Probes
To Order, add suffix "**-DUAL**" to model no. Add to base probe price any options (extra probe length, overbraiding, armored cable), then multiply this price x 1.75. **Ordering Example:TJ36-CASS-14G-12-DUAL**, $35 x 1.75 = **$61.25**.

For additional PFA lead wire length, add **$1.00** per 12" over 40" and change "**36**" in part no. to desired length in inches. **Ordering Example: TJ120-ICSS-14G-12**, type J transition joint probe with 120" of PFA lead wire, ¼ OD stainless steel sheath, 12" length, $35 + 7 = **$42**.

Available as
SUPER OMEGACLAD™ XL THERMOCOUPLE PROBES
MAXIMUM PERFORMANCE SHEATHING ELIMINATES HIGH TEMPERATURE DRIFT
See page A-43 to A-48.

MADE IN USA

MEETS OR EXCEEDS SPECIAL LIMITS OF ERROR (SLE) AND EN 60584-2: Tolerance Class 1

OMEGACAL™ Factory CAL AVAILABLE See Section I

ANSI color code shown

To order IEC color code see page A-9

310 Stainless Steel Sheaths
To Order, replace "**SS**" in Model no. with 310SS, no add'l charge. **Ordering Example: TJ36-CA310SS-18G-12**, type K transition joint probe with 310 stainless steel sheath, **$28**.

Discount Schedule	
1-10 units	Net
11-24 units	10%
25-49 units	20%
50 and up	Consult Sales

▭ ***MOST POPULAR MODELS HIGHLIGHTED!***

To Order *(Specify Model Number)*

Alloy/ANSI Color Code	Sheath Dia. (")	Model No. 12" Length	Price		Model No. 18" Length	Price		Model No. 24" Length	Price		Price/ Add'l 12"
			G*/E	U*		G*/E*	U*		G*/E*	U*	
IRON-CONSTANTAN Inconel Sheath J	1/16"	TJ36-ICIN-116(*)-12	$28.00	$30.00	TJ36-ICIN-116(*)-18	$28.80	$30.80	TJ36-ICIN-116(*)-24	$29.55	$31.55	$1.55
	⅛"	TJ36-ICIN-18(*)-12	28.00	30.00	TJ36-ICIN-18(*)-18	29.60	31.60	TJ36-ICIN-18(*)-24	31.15	33.15	3.15
	3/16"	TJ36-ICIN-316(*)-12	29.00	31.00	TJ36-ICIN-316(*)-18	31.20	33.20	TJ36-ICIN-316(*)-24	33.35	35.35	4.35
	¼"	TJ36-ICIN-14(*)-12	35.00	37.00	TJ36-ICIN-14(*)-18	38.80	40.80	TJ36-ICIN-14(*)-24	42.50	44.50	7.50
IRON-CONSTANTAN 304 SS Sheath J	1/16"	TJ36-ICSS-116(*)-12	$28.00	$30.00	TJ36-ICSS-116(*)-18	$28.80	$30.80	TJ36-ICSS-116(*)-24	$29.55	$31.55	$1.55
	⅛"	TJ36-ICSS-18(*)-12	28.00	30.00	TJ36-ICSS-18(*)-18	28.90	32.90	TJ36-ICSS-18(*)-24	29.85	31.85	1.85
	3/16"	TJ36-ICSS-316(*)-12	29.00	31.00	TJ36-ICSS-316(*)-18	30.60	32.60	TJ36-ICSS-316(*)-24	32.15	34.15	3.15
	¼"	TJ36-ICSS-14(*)-12	35.00	37.00	TJ36-ICSS-14(*)-18	37.50	39.50	TJ36-ICSS-14(*)-24	40.00	42.00	5.00
CHROMEGA®-ALOMEGA® ** Inconel Sheath K	1/16"	TJ36-CAIN-116(*)-12	$28.00	$30.00	TJ36-CAIN-116(*)-18	$28.80	$30.80	TJ36-CAIN-116(*)-24	$29.55	$31.55	$1.55
	⅛"	TJ36-CAIN-18(*)-12	28.00	30.00	TJ36-CAIN-18(*)-18	29.60	31.60	TJ36-CAIN-18(*)-24	31.15	33.15	3.15
	3/16"	TJ36-CAIN-316(*)-12	29.00	31.00	TJ36-CAIN-316(*)-18	31.20	33.20	TJ36-CAIN-316(*)-24	33.35	35.35	4.35
	¼"	TJ36-CAIN-14(*)-12	35.00	37.00	TJ36-CAIN-14(*)-18	38.80	40.80	TJ36-CAIN-14(*)-24	42.50	44.50	7.50
CHROMEGA®-ALOMEGA® 304 SS Sheath K	1/16"	TJ36-CASS-116(*)-12	$28.00	$30.00	TJ36-CASS-116(*)-18	$28.80	$30.80	TJ36-CASS116(*)-24	$29.55	$31.55	$1.55
	⅛"	TJ36-CASS-18(*)-12	28.00	30.00	TJ36-CASS-18(*)-18	28.90	30.90	TJ36-CASS-18(*)-24	29.85	31.85	1.85
	3/16"	TJ36-CASS-316(*)-12	29.00	31.00	TJ36-CASS-316(*)-18	30.60	32.60	TJ36-CASS-316(*)-24	32.15	34.15	3.15
	¼"	TJ36-CASS-14(*)-12	35.00	37.00	TJ36-CASS-14(*)-18	37.50	39.50	TJ36-CASS-14(*)-24	40.00	42.00	5.00
CHROMEGA®-CONSTANTAN Inconel Sheath E	1/16"	TJ36-CXIN-116(*)-12	$28.00	$30.00	TJ36-CXIN-116(*)-18	$28.90	$30.90	TJ36-CXIN-116(*)-24	$29.85	$31.85	$1.85
	⅛"	TJ36-CXIN-18(*)-12	28.00	30.00	TJ36-CXIN-18(*)-18	29.90	31.90	TJ36-CXIN-18(*)-24	31.15	33.15	3.75
	3/16"	TJ36-CXIN-316(*)-12	29.00	31.00	TJ36-CXIN-316(*)-18	31.50	33.50	TJ36-CXIN-316(*)-24	33.35	35.35	5.00
	¼"	TJ36-CXIN-14(*)-12	35.00	38.00	TJ36-CXIN-14(*)-18	39.80	41.80	TJ36-CXIN-14(*)-24	43.50	45.50	7.50
CHROMEGA®-CONSTANTAN 304 SS Sheath E	1/16"	TJ36-CXSS-116(*)-12	$28.00	$30.00	TJ36-CXSS-116(*)-18	$28.90	$30.80	TJ36-CXSS-116(*)-24	$29.55	$31.55	$1.55
	⅛"	TJ36-CXSS-18(*)-12	28.00	30.00	TJ36-CXSS-18(*)-18	29.90	31.30	TJ36-CXSS-18(*)-24	30.50	32.50	2.50
	3/16"	TJ36-CXSS-316(*)-12	29.00	31.00	TJ36-CXSS-316(*)-18	31.50	32.60	TJ36-CXSS-316(*)-24	32.15	34.15	3.15
	¼"	TJ36-CXSS-14(*)-12	35.00	37.00	TJ36-CXSS-14(*)-18	39.80	39.50	TJ36-CXSS-14(*)-24	40.00	42.00	5.00
COPPER-CONSTANTAN Inconel Sheath T	1/16"	TJ36-CPIN-116(*)-12	$28.00	$30.00	TJ36-CPIN-116(*)-18	$28.90	$30.90	TJ36-CPIN-116(*)-24	$29.55	$31.55	$1.85
	⅛"	TJ36-CPIN-18(*)-12	28.00	30.00	TJ36-CPIN-18(*)-18	29.90	31.90	TJ36-CPIN-18(*)-24	31.75	33.75	3.75
	3/16"	TJ36-CPIN-316(*)-12	29.00	31.00	TJ36-CPIN-316(*)-18	31.50	33.50	TJ36-CPIN-316(*)-24	33.35	35.35	5.00
	¼"	TJ36-CPIN-14(*)-12	35.00	38.00	TJ36-CPIN-14(*)-18	39.80	41.80	TJ36-CPIN-14(*)-24	43.50	45.50	7.50
COPPER-CONSTANTAN 304 SS Sheath T	1/16"	TJ36-CPSS-116(*)-12	$28.00	$30.00	TJ36-CPSS-116(*)-18	$28.80	$30.80	TJ36-CPSS-116(*)-24	$29.55	$31.55	$1.55
	⅛"	TJ36-CPSS-18(*)-12	28.00	30.00	TJ36-CPSS-18(*)-18	29.30	31.30	TJ36-CPSS-18(*)-24	30.50	32.50	2.50
	3/16"	TJ36-CPSS-316(*)-12	29.00	31.00	TJ36-CPSS-316(*)-18	30.60	32.60	TJ36-CPSS-316(*)-24	32.15	34.15	3.15
	¼"	TJ36-CPSS-14(*)-12	35.00	37.00	TJ36-CPSS-14(*)-18	37.50	39.50	TJ36-CPSS-14(*)-24	40.00	42.00	5.00
OMEGALLOY®-NICROSIL-NISIL ** Inconel Sheath N	1/16"	TJ36-NNIN-116(*)-12	$28.00	$30.00	TJ36-NNIN-116(*)-18	$28.80	$30.80	TJ36-NNIN-116(*)-24	$29.55	$31.55	$1.55
	⅛"	TJ36-NNIN-18(*)-12	28.00	30.00	TJ36-NNIN-18(*)-18	29.60	31.60	TJ36-NNIN-18(*)-24	31.15	33.15	3.15
	3/16"	TJ36-NNIN-316(*)-12	29.00	31.00	TJ36-NNIN-316(*)-18	31.20	33.20	TJ36-NNIN-316(*)-24	33.35	35.35	4.35
	¼"	TJ36-NNIN-14(*)-12	35.00	37.00	TJ36-NNIN-14(*)-18	38.80	40.75	TJ36-NNIN-14(*)-24	42.50	44.50	7.50

***Note:** Other lengths are available, consult Sales. 6" probes also available, change "-12" to "-6" to order. No additional charge. To order optional sheaths, change "**SS**" in Model no. to "**IN**" for Inconel, "**304SS**" for 304 SS, "**310SS**" for 310 SS, "**316SS**" for 316 SS or "321SS" for 321 SS. No additional charge.*

** Specify junction type: **E** (Exposed), **G** (Grounded) or **U** (Ungrounded). For lengths from 2" to 12", please consult Sales.*

*** For **Super OMEGACLAD® XL**, change "IN" to "XL" and add **$3** to price.*

***Ordering Examples: TJ36-CASS-18U-12**, heavy duty transition joint probe, Type K (CHROMEGA®-ALOMEGA®), 304 SS sheath, ⅛" OD, ungrounded junction, 12" length, **$30. TJ36-NNXL-14G-12**, Type N transition joint probe with Super OMEGACLAD®, ¼ OD stainless steel sheath, 12" length, $35 + 3 = $38.*

B.4 Pressure Transducers

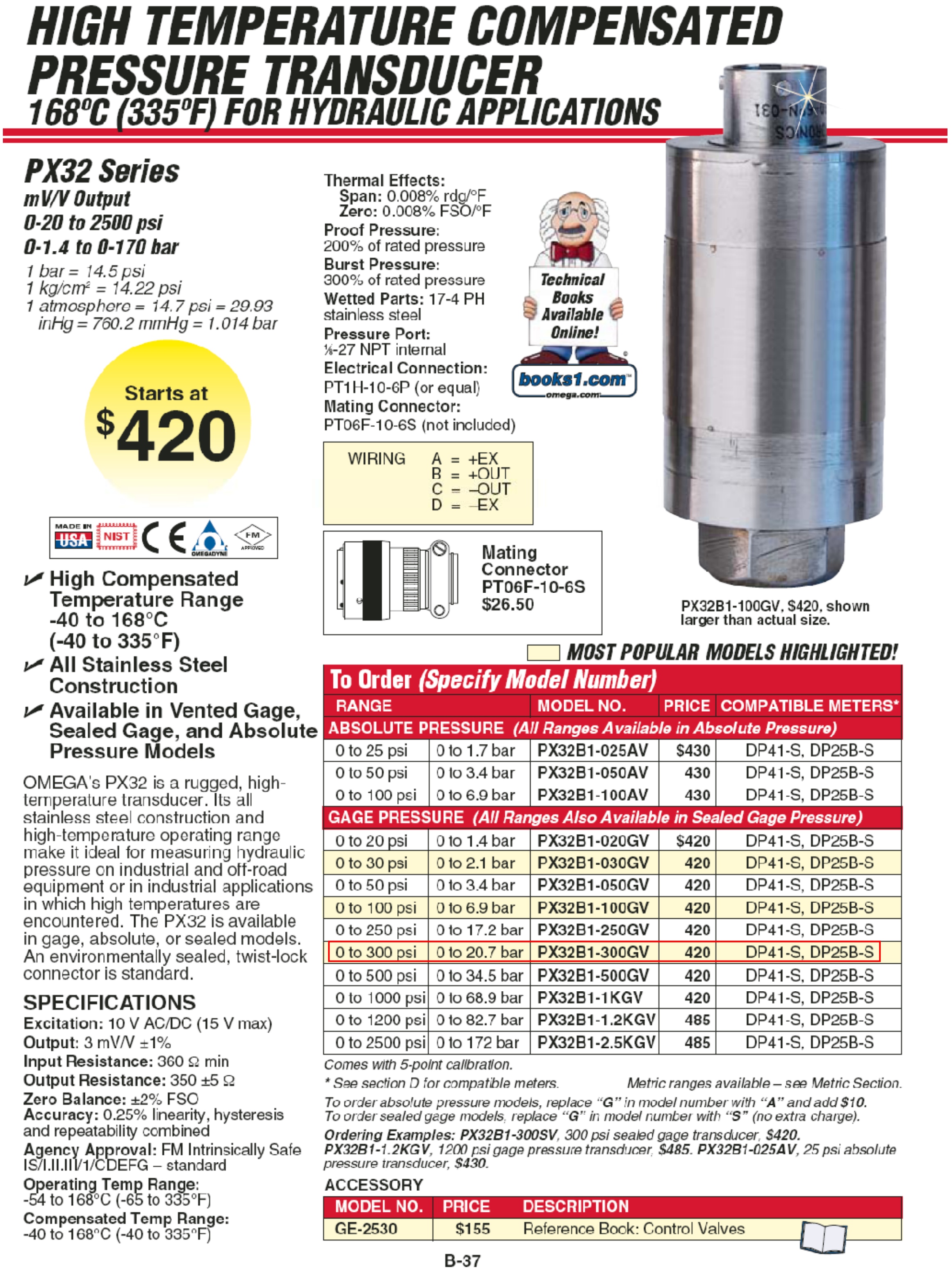

HIGH TEMPERATURE COMPENSATED PRESSURE TRANSDUCER

168°C (335°F) FOR HYDRAULIC APPLICATIONS

PX32 Series

mV/V Output

0-20 to 2500 psi

0-1.4 to 0-170 bar

1 bar = 14.5 psi
1 kg/cm² = 14.22 psi
1 atmosphere = 14.7 psi = 29.93 inHg = 760.2 mmHg = 1.014 bar

Starts at $420

- **High Compensated Temperature Range -40 to 168°C (-40 to 335°F)**
- **All Stainless Steel Construction**
- **Available in Vented Gage, Sealed Gage, and Absolute Pressure Models**

OMEGA's PX32 is a rugged, high-temperature transducer. Its all stainless steel construction and high-temperature operating range make it ideal for measuring hydraulic pressure on industrial and off-road equipment or in industrial applications in which high temperatures are encountered. The PX32 is available in gage, absolute, or sealed models. An environmentally sealed, twist-lock connector is standard.

SPECIFICATIONS

Excitation: 10 V AC/DC (15 V max)

Output: 3 mV/V ±1%

Input Resistance: 360 Ω min

Output Resistance: 350 ±5 Ω

Zero Balance: ±2% FSO

Accuracy: 0.25% linearity, hysteresis and repeatability combined

Agency Approval: FM Intrinsically Safe IS/I.II.III/1/CDEFG – standard

Operating Temp Range: -54 to 168°C (-65 to 335°F)

Compensated Temp Range: -40 to 168°C (-40 to 335°F)

Thermal Effects:
Span: 0.008% rdg/°F
Zero: 0.008% FSO/°F

Proof Pressure: 200% of rated pressure

Burst Pressure: 300% of rated pressure

Wetted Parts: 17-4 PH stainless steel

Pressure Port: ⅛-27 NPT internal

Electrical Connection: PT1H-10-6P (or equal)

Mating Connector: PT06F-10-6S (not included)

WIRING
A = +EX
B = +OUT
C = –OUT
D = –EX

Technical Books Available Online!
books1.com
omega.com

Mating Connector PT06F-10-6S $26.50

PX32B1-100GV, $420, shown larger than actual size.

▭ ***MOST POPULAR MODELS HIGHLIGHTED!***

To Order *(Specify Model Number)*

RANGE		MODEL NO.	PRICE	COMPATIBLE METERS*
ABSOLUTE PRESSURE *(All Ranges Available in Absolute Pressure)*				
0 to 25 psi	0 to 1.7 bar	**PX32B1-025AV**	**$430**	DP41-S, DP25B-S
0 to 50 psi	0 to 3.4 bar	**PX32B1-050AV**	**430**	DP41-S, DP25B-S
0 to 100 psi	0 to 6.9 bar	**PX32B1-100AV**	**430**	DP41-S, DP25B-S
GAGE PRESSURE *(All Ranges Also Available in Sealed Gage Pressure)*				
0 to 20 psi	0 to 1.4 bar	**PX32B1-020GV**	**$420**	DP41-S, DP25B-S
0 to 30 psi	0 to 2.1 bar	**PX32B1-030GV**	**420**	DP41-S, DP25B-S
0 to 50 psi	0 to 3.4 bar	**PX32B1-050GV**	**420**	DP41-S, DP25B-S
0 to 100 psi	0 to 6.9 bar	**PX32B1-100GV**	**420**	DP41-S, DP25B-S
0 to 250 psi	0 to 17.2 bar	**PX32B1-250GV**	**420**	DP41-S, DP25B-S
0 to 300 psi	0 to 20.7 bar	**PX32B1-300GV**	**420**	DP41-S, DP25B-S
0 to 500 psi	0 to 34.5 bar	**PX32B1-500GV**	**420**	DP41-S, DP25B-S
0 to 1000 psi	0 to 68.9 bar	**PX32B1-1KGV**	**420**	DP41-S, DP25B-S
0 to 1200 psi	0 to 82.7 bar	**PX32B1-1.2KGV**	**485**	DP41-S, DP25B-S
0 to 2500 psi	0 to 172 bar	**PX32B1-2.5KGV**	**485**	DP41-S, DP25B-S

Comes with 5-point calibration.

** See section D for compatible meters.* *Metric ranges available – see Metric Section.*

*To order absolute pressure models, replace "**G**" in model number with "**A**" and add **$10.***
*To order sealed gage models, replace "**G**" in model number with "**S**" (no extra charge).*

Ordering Examples: PX32B1-300SV**, 300 psi sealed gage transducer, **$420. PX32B1-1.2KGV**, 1200 psi gage pressure transducer, **$485. PX32B1-025AV**, 25 psi absolute pressure transducer, **$430.

ACCESSORY

MODEL NO.	PRICE	DESCRIPTION
GE-2530	$155	Reference Book: Control Valves

B-37

6:1 TURN-DOWN INDUSTRIAL DIFFERENTIAL PRESSURE TRANSMITTER

PX771A Series

4 to 20 mA Output
0-17 inH$_2$O to 0-300 psid

Starts at
$945

PX771A transmitter, shown with iSeries strain and process meters and controllers featured on page D-7, which start at $150 and are shown smaller than actual size.

- **2-Year Warranty**
- **0.15% FS Accuracy**
- **Explosion-Proof Electrical Housing**
- **Stainless Steel Wetted Parts**
- **Process Wetted Parts Meet NACE Specification MR0175-91**
- **High Common-Mode Pressure Rejection**
- **6:1 Turn-Down Capability**
- **±600% Zero Suppression or Elevation**
- **NEMA 4X (IP66) Housing**
- **4 to 20 mA or 1 to 5 Vdc Output**

PX771A-025DI, $945, shown smaller than actual size.

The OMEGA® PX771A low-power pressure transmitter is a compact, high-performance unit, designed to measure differential pressure and transmit a 4 to 20 mA signal. It has an adjustable range with a turn-down ratio of 6:1, and it comes factory-calibrated at the highest span. Ranges from 17 inH$_2$O to 300 psid are available. Zero and span adjustments are accessed inside the electronic housing. The zero point can be elevated and suppressed up to ±600%. This transducer has an internal silicon diaphragm into which piezoresistive strain gages are diffused, then interconnected to form a pressure sensitive Wheatstone bridge.

FOR GAGE, DIFFERENTIAL, AND VACUUM MEASUREMENTS

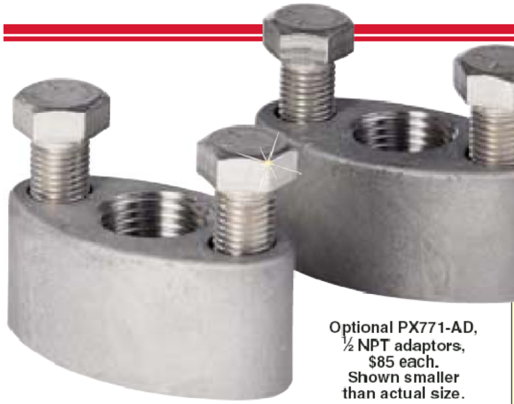

Optional PX771-AD, ½ NPT adaptors, $85 each. Shown smaller than actual size.

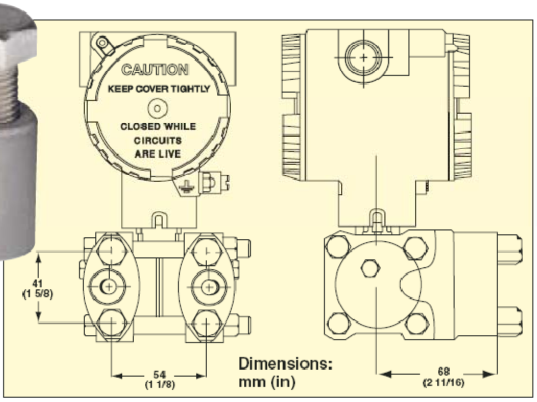

SPECIFICATIONS

Service: Liquid, gas or vapor

Excitation:
24 Vdc, 7 to 36 Vdc mA output,
6 to 42 Vdc @ 1.6 mA voltage output

Output: 4 to 20 mA (2 wire) or 1 to 5 Vdc (3 wire) jumper selectable

Max Loop Resistance: (Supply voltage – 7) x 50 Ω

Accuracy: ±0.1% of URL (upper range limit, includes linearity, hysteresis and repeatability)

Stability: ±0.25% of URL (upper range limit) 1 year

Span Adjust: 16 to 100% URL (DIP switches and pot)

Zero Adjust: -600 to 600% LRL (lower range limit)

Operating Temperature:
Process: -40 to 104°C (-40 to 220°F)
Electrical: -32 to 85°C (-25 to 185°F)

Ambient Total Thermal Effects:
0.010% URL/°F for -25 to 75°F
0.015% URL/°F for 75 to 185°F
(0.020% URL/°F for 100 inH_2O)

Response Time: 63% response 1 ms or 50 ms with damping

Static Pressure Effect:
+0.05% of URL <100 psi ranges
+0.1% of URL for 100 and 300 psi ranges

EMI Effect: ±1% URL @ 10 V/m from 20 to 500 MHz. Meets /SAMA PMC-33-1C with cover in place and electrical wiring in grounded conduit.

Approvals: UL/CUL
Hazardous Location: I/I/C, D
Non-incendive: I/II/A, B, C, D

Wetted Parts: 316 SS

Process Connection: ¼ NPT internal, ½ NPT with optional adaptors

Fill Fluid: DC 200 silicone

Housing: Low copper aluminum, epoxy coated, NEMA 4X (IP66)

Electrical Connection: ½ NPTF conduit, with internal screw terminals

Weight: 2.9 kg (6.4 lb)

Compatible Meters:
DP41-E, DP25-E,
DP24-E, DP460,
DP3002-E and others
(see section D for complete selection)

☐ **MOST POPULAR MODELS HIGHLIGHTED!**

To Order *(Specify Model Number)*

RANGE	MODEL NO.	PRICE	MAX WORK PRES	COMPATIBLE METERS*
0-17 to 0-100 inH_2O	**PX771A-100WCDI**	**$945**	2000 psi	iSeries, DP25B-E, DP41-E, DP460-E
0-50 to 0-300 inH_2O	**PX771A-300WCDI**	**945**	2000 psi	iSeries, DP25B-E, DP41-E, DP460-E
0-4.2 to 0-25 psi	**PX771A-025DI**	**945**	2000 psi	iSeries, DP25B-E, DP41-E, DP460-E
0-17 to 0-100 psi	**PX771A-100DI**	**945**	2000 psi	iSeries, DP25B-E, DP41-E, DP460-E
0-50 to 0-300 psi	**PX771A-300DI**	**945**	2000 psi	iSeries, DP25B-E, DP41-E, DP460-E

OPTIONS AND ACCESSORIES

-SUFFIX or MODEL NO.	PRICE	DESCRIPTION
-M3	**$165**	3½ digit LCD local indicator (FM approval not available with option)
PX771-AD	**85**	1 pair of stainless steel ½ NPT adaptors
PX771A-MB-KIT	**65**	2" pipe mounting bracket (order separately), flange mount
PX771A-MB-KIT-N	**65**	Neck mounting bracket kit (order separately)
OP-17	**15**	Reference Book: Measure for Measure

** See section D for compatible meters.*
Comes with complete operator's manual.
Ordering Example: PX771A-300WCDI**, industrial transmitter with 0 to 50 to 0 to 300 inH_2O range, **$945.

B.5 Turbine Flow Meter (Dynalene)

FT Series

Turbine Flowmeters for Liquid Applications

Description

Flow Technology's FT Series turbine flowmeters utilize a proven flow measurement technology to provide exceptionally reliable digital outputs. Because of their versatility, these flowmeters are the solution for a wide variety of liquid flow sensing applications. FT Series turbine flowmeters, which range in size from 3/8 inch to 4 inches, offer a high turn-down capability, repeatability of ±0.05% of reading, and excellent speed of response.

The precision, axial-mounted rotor design of the standard turbine flowmeter allows it to operate effectively in flow rates from 0.03 to 1,500 GPM, with the linearity rated at ±0.5% of reading over the normal 10:1 turn-down range. All turbine flowmeters can achieve ±0.1% linearity over the full operating range with linearizing electronics. Typical operating pressures for the standard meters are 5,000 PSIG with custom configurations capable of 30,000 PSIG.

A choice of construction materials can be specified for the turbine flowmeter's housing, rotor, bearings and shaft, including standard stainless steel, and exotic materials for specialized applications.

FT Series Meters

Features

- Linearity < 0.10% with linearizing electronics
- High turn-down capability, up to 100:1.
- Excellent repeatability, less than +/- 0.05%.
- Typical response time 3-4mS
- Extensive primary standard NIST traceable calibration capability, offering a wide range of fluids, viscosities and flow rates. Accuracy less than +/-0.05% typical
- Standard materials of construction are 316 SS housing and 430F SS rotor. Additional materials available.
- Robust, compact design capably of compliance to severe shock and vibration requirements.
- Standard pressure capabilities up to 5000 PSIG.
- Extreme operating pressures available in custom packages.
- High shock designs available for applications with large hydraulic water hammer effects.
- Custom designs to meet the specific application are routine, not the exception.

Specifications

Calibration accuracy	±0.05% of reading, traceable to NIST
Repeatability	±0.05% of reading
Linearity	±0.10% with linearizing electronics
Response time	3-4mS typical
Housing material	316 stainless steel, standard
Rotor material	430F stainless steel, standard
Temperature range	-450 to 750°F, dependent on bearing and pick-off
Operating pressure	Up to 30,000PSIG, dependent on fitting
Ball bearing material	440C stainless steel
Journal bearing material	Ceramic, tungsten carbide, graphite
Pick-off's	Modulated carrier and magnetic
Straight Run	10D upstream and 5D downstream minimum
Recommended filtration	Ball bearings: 10 to 100 microns (less filtration with larger sizes) Journal bearings: 75 to 100 microns

FTI FLOW TECHNOLOGY™

Turbine Flow Meter Model Number Selection and Sizing Guidelines

There are 4 major steps in defining a turbine flow meter; these are:

- Choosing the flow meter size
- Bearing selection
- Pick-off selection
- Calibration requirements

These components are interrelated and should be considered as a system to obtain optimum meter performance. Additional options need to be selected that are related more to personal preference. These are end fitting type, materials of construction, and units of measure.

Step 1: Meter size and flow range selection

Detailed below are the considerations that should be taken into account when sizing a flow meter.

- Due to the laws of physics, for optimum results any flow meter (including turbine flow meters) should be operated as high up in their turndown range as possible.
- Clearly, there is a tradeoff between your allowable pressure drop and the size of meter that you can install into your process. In other words, at a given flow rate, a smaller meter will operate higher up in its flow rate range, but will generate a higher pressure drop.
- When selecting the size and flow range of the meter, bearing and pick-off selection must be considered. Ball bearings and RF pick-offs have the least amount of drag, thus provide the widest capable flow range. Journal bearings and magnetic pick-offs create more drag, there fore reducing the turndown capability of the flow meter. Where ever possible an RF pickoff is the ideal choice.
- Ideally, it is beneficial to stay within a 10:1 turndown range. However, the phenomenal repeatability and primary calibration accuracy's enable the Flow Technology turbine to provide outstanding performance over a 100:1 turndown.
- See page 4 for available flow ranges.

Step 2: Pickoff Selection

Reasons to choose a RF pickoff

- Use on FT-24 and smaller meters.
- Use when extended flow range is required.
- Use when real time temperature correction (UVC calibration) is required.
- Flow meter does not require recalibration when pick-off is changed.
- Must be used in conjunction with an amplifier to produce a square wave frequency output.
- Can not be used above an FT-40 size flow meter.

Reasons to choose a Magnetic pickoff

- Use on FT-32 and larger meters.
- Use on cryogenic temperature applications.
- Use when a direct millivolt output is required.
- Flow meter should be recalibrated when pick-off is changed.
- Can be used on smaller flow meters with reduced flow range.

Pick-off Options

- Standard pick-offs have upper operating temperature of 350°F.
- High temperature pick-offs with a 750°F maximum are available.
- Most electronics are available in hazardous area rated enclosures. If system certification is required, pick-offs are available with various ratings.
- Pick-offs are available with built in RTD's when real time temperature correction is required and a UVC calibration is performed on the flow meter. These pick-offs are normally used in conjunction with the Linear Link TCI electronics.
- Amplified pick-offs are available that house circuitry in the pick-off body to provide a high level 0 – 5 volt square wave pulse output. DC power is required.
- See page 6 for pick-off selection options.

Pick-off Mounting Configuration

MS connector

- Pick-offs have two, three or four pin MS connectors.
- Connection to the pick-off is via a mating MS connector with soldered connections and loose wire.
- Typical installation is on test stands or on board applications.
- A junction box or conduit **can not** be attached to this pick-off style.
- This pick-off is used on flow meters that **do not** have 1" MNPT nipples welded to the meter body surrounding the pick-off. Flow meters with threaded end connections typically do not have the 1" nipple.

Flying leads with threaded connection

- Pick-offs have flying leads extending from the potted pick-off body.
- Mechanical connection to the pick-off is via a ½" MNPT thread integral to the top of the pick-off body or the 1" MNPT thread of the flow meter nipple.
- This pick-of style is required when a junction box and rigid or flexible conduit is to be mounted directly to the pick-off body.
- Typical installation is a more industrial environment.
- This threaded body pick-off is used on flow meters that **do not** have 1" MNPT nipples welded to the meter body surrounding the pick-off. A flying lead pick-off with smooth body are used on flow meters that **do** have the 1" MNPT nipple. Flow meters with threaded end connections typically do not have the 1" nipple. Flow meters with flanged end connections typically do have the 1" nipple.

Step 3: Bearing Selection

- Bearings are available in two styles, Ball and Journal Sleeve.
- Ball bearings are manufactured from 440C SS and is the typical choice for lubricating applications.
- Journal Sleeve bearings are available in three different material selections. (Note: The Journal Ceramic bearing is the typical bearing of choice for non-lubricating applications.)
- See page 5 for bearing selection options.

Ball bearings (model # code "A")

- Bearing option to measure lubricating fluids.
- Low frictional drag provides the widest possible flow range.
- Ball bearing set can be replaced in the field.
- 10 to 50 micron filtration required, dependent on meter size.
- Operating temperature range of -450° to 300° F.
- 440C stainless steel materials of construction.
- Provides exceptional life and rugged construction in clean lubricating applications.

Journal Carbide bearings (model # code "D")

- Bearing option to measure low or non-lubricating fluids.
- Hard bearing material provides long life and rugged construction.
- Less turn down capability than the ball bearing. (valid for all journal bearing options)
- Field replacement of bearing not recommended. (valid for all journal bearing options)
- 75 to 100 micron filtration required. (valid for all journal bearing options)
- Operating temperature range of -100° to 1200° F.
- Tungsten Carbide materials of construction.
- Hard bearing material provides long life and rugged construction.

Journal Graphite bearings (model # code "E")

- Bearing option for corrosive applications.
- Operating temperature range of -100° to 550° F.
- Bearing option to measure low or non-lubricating fluids.
- Materials of construction are epoxy impregnated Carbon Graphite bearing with 316 SS shaft.
- Lubricating property of the graphite allows this bearing to run smoother than the other two journal options, however life of the bearing will be slightly reduced.
- Not recommended for use above FT-32 meter size.

Journal Ceramic bearings (model # code "G")

- Typical bearing option to measure low or non-lubricating fluids.
- Operating temperature range of -100° to 800° F.
- Typical bearing option for more corrosive applications.
- AL2O3 (99.5%) Ceramic materials of construction.
- Ceramic material is impervious to most fluids, resists film build up on bearing surface, long life, not as robust as tungsten carbide material.
- Not recommended for use in water above 180° F.

Step 4: Calibration Selection

- Flow Technology has one of the world's largest liquid and gas primary calibration facilities.
- The ability to accurately calibrate a flow meter with trace ability to international standards is one of the fundamental requirements in any flow metering application.
- Flow Technology offers a range of water, solvent, oil, and oil blend calbrations.
- A 10 data point calibration is offered as standard, 20 and 30 point calibrations are offered as options. A higher number of data points will define the calibration curve in more detail. If linearizing electronics will be used a minimum of a 20 point calibration is recommended.
- Viscosity does shift the flow meter calibration curve and should be compensated for.

Application will be at relatively constant temperature and viscosity

- For optimum performance your flow meter should be calibrated close to its operating viscosity. Water at 1 cst and solvent at 1.2 cst viscosity is standard, a specific calibration to simulate the operating viscosity can be specified as an option.

Application will cover a range of operating temperature and viscosity

- If the fluid viscosity or density is changing due to temperature variation, a Universal Viscosity Calibration (UVC) should be used to perform real time temperature correction.
- The viscosity range for the calibration is determined by the minimum fluid viscosity at the maximum operating temperature and the maximum fluid viscosity at the minimum operating temperature.
- See page 5 for calibration options.

FT Series

FT Meter Sizing and End Fittings

					Extended Flow Range							
Series / Order Code	End Fitting Nominal Inches	ID	10:1 Standard Range		Ball Bearing / RF Pickoff	Ball Bearing Mag Pickoff	Journal Bearing / RF Pickoff	Journal Bearing / Mag Pickoff	Max	K Factor	Maximum Frequency Approx.
			Min GPM	Max GPM	Min GPM	Min GPM	Min GPM	Min GPM	GPM	P/G	Frequ.
FT 4-6	3/8	0.30	0.25	2.5	0.03	0.10	0.10	0.12	3	48000	2000
FT 4-8	1/2	0.30	0.25	2.5	0.03	0.10	0.10	0.12	3	48000	2000
FT 6-8	1/2	0.37	0.50	5.0	0.05	0.12	0.15	0.20	5	25000	2100
FT 8-8	1/2	0.40	0.75	7.5	0.08	0.16	0.20	0.25	8	16000	2000
FT -08	1/2	0.44	1.00	10.0	0.10	0.20	0.25	0.30	10	12000	2000
FT-10	* 3/4	0.50	1.25	12.5	0.15	0.30	0.30	0.40	15	9600	2000
FT-12	3/4	0.56	2.0	20	0.25	0.50	0.50	0.50	25	6000	2000
FT-16	1	0.86	5.0	50	0.60	1.0	1.0	1.0	60	2400	2000
FT-20	11/4	1.00	9.0	90	1.0	1.5	1.0	1.5	100	1300	1950
FT-24	11/2	1.32	15.0	150	1.6	2.5	1.6	2.5	160	600	1500
FT-32	2	1.75	22.0	225	2.5	3.5	2.5	3.5	250	350	1300
FT-40	21/2	2.22	40.0	400	4.5	5.0	4.5	5.0	450	180	1200
FT-48	3	2.87	65.0	650	N/A	7.5	N/A	7.5	750	75	812
FT-64	4	3.87	125.0	1250	N/A	15	N/A	15	1500	30	625

* AE fitting = 5/8"

Order Code	End Fittings
AE	AN (or MS) external straight threads - 3/8" to 2 1/2 nominal size - 37° flare
NE	NPT external threads - 1/2" to 4 nominal size
HB	Hose Barb - 13 to 51 mm/ 1/2" to 2
WF	Wafer type - serrated surface - 13 to 76 mm/1/2" to 3 nominal size
C1	150# Raised Face Flange
C2	300# Raised Face Flange
C3	600# Raised Face Flange
C4	900# Raised Face Flange
C5	1500# Raised Face Flange
C6	2500# Raised Face Flange
J2	300# Ring Joint Flange
J3	600# Ring Joint Flange
J4	900# Ring Joint Flange
J5	1500# Ring Joint Flange
J6	2500# Ring Joint Flange
T1	Tri-Clamp 1/2" to 3/4
T2	Tri-Clamp 1" to 1 1/2

Part Number Structure

F	T	x	x	x	x	x	x	x	x	L	x	x	x	x	x	x	x
Meter Size					End Fittings		Calibration				Material	Bearing	Pickoff		Optional Designators		

Calibration

Order Code	# Points	Flow Range	Fluid
NW	10 point	normal 10:1 range	in water
NS	10 point	normal 10:1 range	in solvent
NB	10 point	normal 10:1 range	in oil blend
XW	10 point	extended range	in water
XS	10 point	extended range	in solvent
XB	10 point	extended range	in oil blend
TW	20 point	normal 10:1 range	in water
TS	20 point	normal 10:1 range	in solvent
TB	20 point	normal 10:1 range	in oil blend
YW	20 point	extended range	in water
YS	20 point	extended range	in solvent
YB	20 point	extended range	in oil blend
GW	30 point	extended range	in water
GS	30 point	extended range	in solvent
GB	30 point	extended range	in oil blend

Order Code	# Points	Cal Style	# Viscosities
U2	10 points each viscosity	Universal Viscosity Curve	2 Viscosities (specify minimum viscosity & maximumviscosity).
U3	10 points each viscosity	Universal Viscosity Curve	3 Viscosities (specify minimum viscosity & maximum viscosity).

Order Code	# Points	# Pickoffs	Cal Style	Fluid
BW	10 points each direction	1 pickoff	Bi-directional	water
BS	10 points each direction	1 pickoff	Bi-directional	solvent
BB	10 points each direction	1 pickoff	Bi-directional	oil blend

Note: W = Water. S = Solvent. B = Oil blend. The fluid viscosity must be provided with oil blend calibrations

Material & Bearing Selection

Order Code	Housing	Rotor	Bearing Code
E	316 SST	430F SST	A - D - E - G - H
G	316 SST	316 SST	D - E - G
H	316 SST	17-4 PH SST	A - D - E - G - H
N	HAST C	HAST C	E - G

Note: Please contact factory for material codes "G" and "N".

3rd Digit of Calibration

Code	The third digit of the calibration designator is normally not used and occupied by a dash (-). When required , the following codes are used.
U	To signify required units of measure other than GPM
R	To signify special calibration flow range other than normal 10:1 or extended range
B	To signify both changes in units and special flow range.

Bearing Selection

Order Code	Bearing selections will affect flow range. Refer to sizing specification table to the left for correct flow ranges.
A	Ball Bearings (440 C)
D	Carbide Journal (Carbide Shaft & Sleeve)
E	Graphite Journal (Graphite Sleeve, 316 SST Shaft)
G	Ceramic Journal (Ceramic Shaft & Sleeve)

Part Number Structure

F	T	x	x	x	x	x	x	x	-	L	x	x	x	x	x	x	x
Meter Size					End Fittings		Calibration				Material	Bearing	Pickoff		Optional Designators		

B.6 Coriolis Flow Meter (CO_2 Flow Meter)

Product Data Sheet
PS-00374, Rev. F
June 2006

Micro Motion® ELITE® Mass Flow and Density Meters

With MVD™ Technology

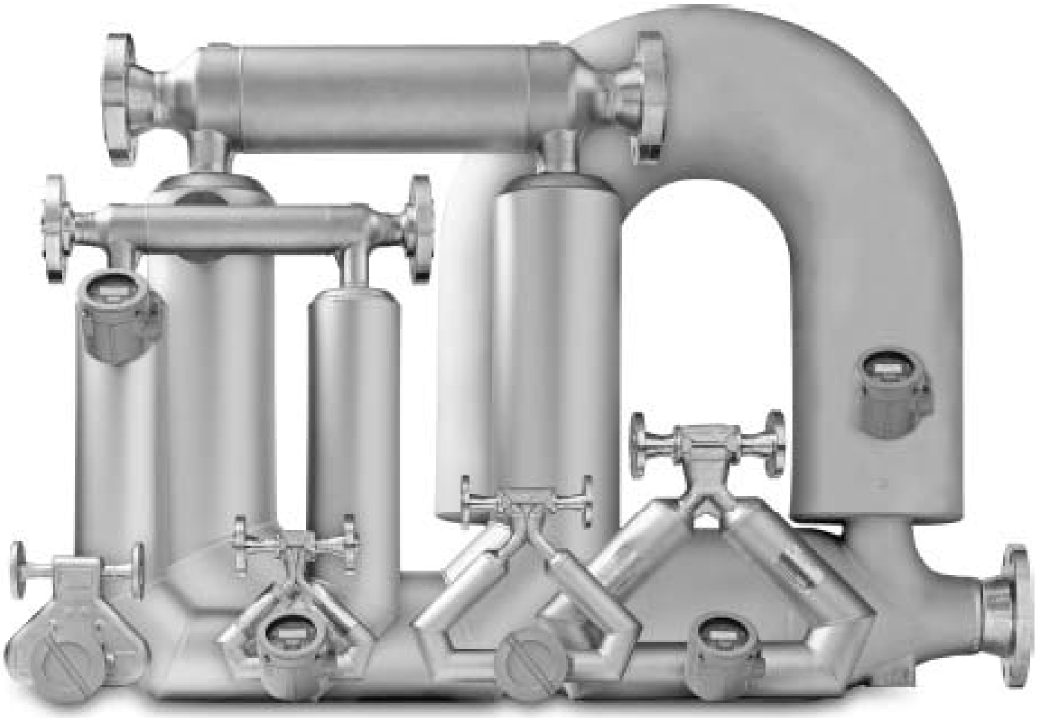

- Unsurpassed performance: mass flow accuracy to ±0.05% of rate, and density accuracy to ±0.0002 g/cm³ (±0.2 kg/m³)
- For mass and volume flow measurement of both gases and liquids
- Wide range of sizes from 1/10″ to 6″ (3 mm to 150 mm)
- Now available with Micro Motion's newest transmitter, the Model 2400S

Micro Motion SERV' INSTRUMENTATION EMERSON. Process Management

Micro Motion® ELITE® mass flow and density meters

Micro Motion® **ELITE®** meters are the leading meters for precision flow and density measurement. ELITE meters offer the most accurate measurement available for virtually any process fluid, while exhibiting exceptionally low pressure drop. Every ELITE meter features standard secondary containment, and is available with stainless steel or nickel alloy wetted parts and a wide variety of process connections to meet your every need.

ELITE meters have been designed for special applications. The CMF010 provides remarkably high performance in low-flow applications. The high-pressure CMF010P is suitable for applications up to 6000 psi (413 bar). The Model CMF400 meter offers the most accurate measurement available in a high-capacity meter. Models CMF200, CMF300, and CMF400 are available in high-temperature and extreme high-temperature versions that provide accurate measurements in severe environments up to 800 °F (427 °C).

Product selector program

Micro Motion offers an on-line program for finding the best products to fit your application. The product selector program allows you to specify the parameters that matter to you, such as accuracy, flow capacity, pressure drop, or turndown. To use the product selector program, visit our web site at **www.micromotion.com**.

Contents

Liquid flow performance

		Mass		Volume(1)			
		lb/min	kg/h	gal/min	l/h	bbl/hr	m^3/h
Maximum flow rate	CMF010	4	108	0.4	108		
	CMF025	80	2180	10	2180		
	CMF050	250	6800	30	6800		
	CMF100	1000	27,200	120	27,200		
	CMF200	3200	87,100	385	87,100	550	87
	CMF300	10,000	272,000	1200	272,000	1700	272
	CMF400	20,000	545,000	2400	545,000	3400	545
Mass and volume flow accuracy(2)(3)	Model 2400S transmitter or enhanced core processor	±0.05% of rate(4)(5)					
	Transmitter with MVD Technology	±0.10% of rate(6)					
	All other transmitters	±0.10% ±[(zero stability / flow rate) × 100]% of rate					
Mass and volume flow repeatability	Model 2400S transmitter or enhanced core processor	±0.025% of rate(4)(5)					
	Transmitter with MVD Technology	±0.05% of rate(6)					
	All other transmitters	±0.05% ±[½(zero stability / flow rate) × 100]% of rate					
		lb/min	kg/h				
Zero stability	CMF010	0.000075	0.002				
	CMF010P	0.00015	0.004				
	CMF025	0.001	0.027				
	CMF050	0.006	0.163				
	CMF100	0.025	0.680				
	CMF200	0.08	2.18				
	CMF300	0.25	6.80				
	CMF400	1.50	40.91				

---

(1) Specifications for volumetric flow rate are based on a process-fluid density of 1 g/cm^3 (1000 kg/m^3). For fluids with density other than 1 g/cm^3 (1000 kg/m^3), the volumetric flow rate equals the mass flow rate divided by the fluid's density.

(2) Stated flow accuracy includes the combined effects of repeatability, linearity, and hysteresis. All specifications for liquids are based on reference conditions of water at 68 to 77 °F (20 to 25 °C) and 15 to 30 psig (1 to 2 bar), unless otherwise noted.

(3) The calibration option for ±0.05% flow accuracy is not available with high-temperature sensor models or Model CMF010P.

(4) When flow rate is less than zero stability / 0.0005, accuracy = ±[(zero stability / flow rate) × 100]% of rate, and repeatability = ±[½(zero stability / flow rate) × 100]%.

(5) When ordered with the ±0.10% factory calibration option, accuracy on liquid = ±0.10% when flow rate ≥ zero stability / 0.001. When flow rate < zero stability / 0.001, accuracy equals ±[(zero stability / flow rate) × 100]% of rate and repeatability equals ±[½(zero stability / flow rate) × 100]% of rate.

(6) When flow rate is less than zero stability / 0.001, accuracy equals ±[(zero stability / flow rate) × 100]% of rate and repeatability equals ±[½(zero stability / flow rate) × 100]% of rate.

Liquid flow performance *continued*

Typical accuracy, turndown, and pressure drop with CMF100 and 2400S transmitter or enhanced core processor

The graph below is an example of the relationship between accuracy, turndown, and pressure drop when measuring the flow of water with a Model CMF100 sensor and Model 2400S transmitter or enhanced core processor.

Actual pressure drop is dependent on process conditions. To determine accuracy, turndown, and pressure drop with your process variables, use Micro Motion's product selector, available at **www.micromotion.com.**

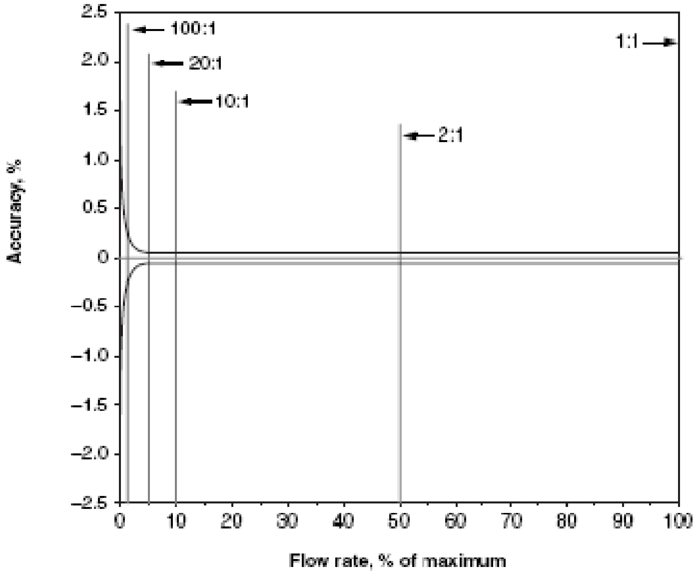

Turndown from maximum flow rate	*500:1*	*100:1*	*20:1*	*10:1*	*2:1*
Accuracy (±%)	1.25	0.25	0.05	0.05	0.05
Pressure drop					
psi	~0	~0	0.2	0.7	13.5
bar	~0	~0	0.01	0.05	0.93

Gas flow performance

When selecting sensors for gas applications, measurement accuracy is a function of fluid mass flow rate independent of operating temperature, pressure, or composition. However, pressure drop through the sensor is dependent upon operating temperature, pressure, and fluid composition. Therefore, when selecting a sensor for any particular gas application, it is highly recommended that each sensor be sized using Micro Motion's product selector, available at **www.micromotion.com**.

	Mass		Volume[1]	
	lb/min	**kg/h**	**SCFM**	**Nm³/h**
Flow rates that produce approximately 10 psid (0.68 bar) pressure drop on *air* at 68 °F (20 °C) and 100 psi (6.8 bar)				
CMF010M, CMF010H	0.30	8	4	6
CMF010P	0.2	6	3	5
CMF025	4	110	60	90
CMF050	10	300	145	230
CMF100	50	1300	640	1000
CMF200	150	4000	2000	3100
CMF300	490	13,300	6500	10,300
CMF400	1250	34,000	16,500	26,250
Flow rates that produce approximately 50 psid (3.4 bar) pressure drop on *natural gas* (MW 16.675) at 68 °F (20 °C) and 500 psi (34.0 bar)				
CMF010M, CMF010H	1	30	30	45
CMF010P	0.9	25	20	35
CMF025	16	450	380	600
CMF050	40	1140	970	1530
CMF100	185	5000	4300	6700
CMF200	560	15,200	13,000	20,500
CMF300	1850	50,500	43,000	68,000
CMF400	4700	128,000	109,000	172,000

---

[1] *Standard (SCFM) reference conditions are 14.7 psia and 68 °F. Normal (Nm³/h) reference conditions are 1.013 bar and 0 °C.*

Gas flow performance *continued*

Mass flow accuracy[1]	Transmitters with MVD Technology (including Model 2400S)	±0.35% of rate[2]	
	All other transmitters	±0.50% of rate $\pm\left[\left(\frac{\text{zero stability}}{\text{flow rate}}\right)\times 100\right]\%$ of rate	
Mass flow repeatability	Transmitters with MVD Technology (including Model 2400S)	±0.20% of rate[2]	
	All other transmitters	±0.25% of rate $\pm\left[\left(\frac{\text{zero stability}}{\text{flow rate}}\right)\times 100\right]\%$ of rate	
		lb/min	**kg/h**
Zero stability	CMF010	0.000075	0.002
	CMF010P	0.00015	0.004
	CMF025	0.001	0.027
	CMF050	0.004	0.103
	CMF100	0.025	0.680
	CMF200	0.08	2.18
	CMF300	0.25	6.80
	CMF400	1.50	40.91

---

(1) Flow accuracy includes the combined effects of repeatability, linearity, and hysteresis.

(2) When flow rate is less than zero stability / 0.0035, accuracy equals ±[(zero stability / flow rate) × 100]% of rate and repeatability equals ±[½(zero stability / flow rate) × 100]% of rate.

Gas flow performance *continued*

Typical mass flow accuracy and pressure drop with CMF100 and transmitter with MVD Technology

Air at 68 °F (20 °C), static pressures as indicated on graph

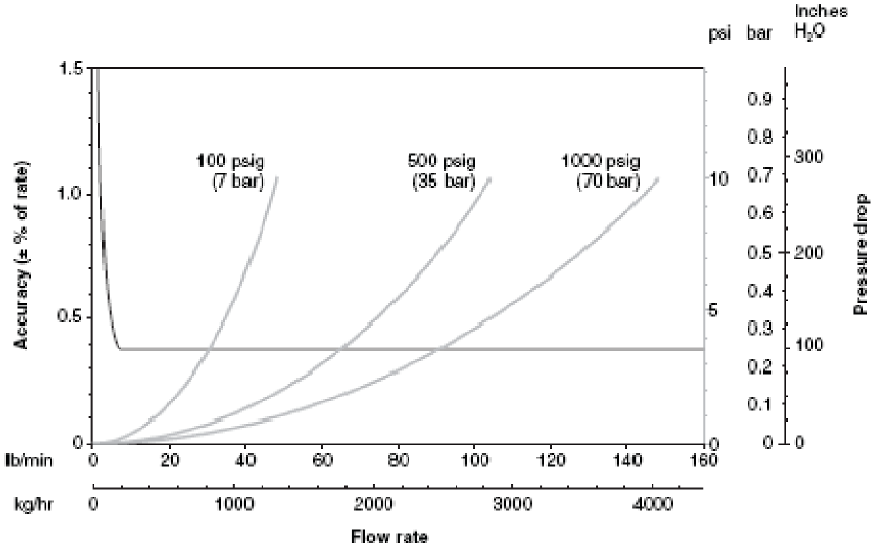

Natural gas (MW 16.675) at 68 °F (20 °C), static pressure as indicated on graph

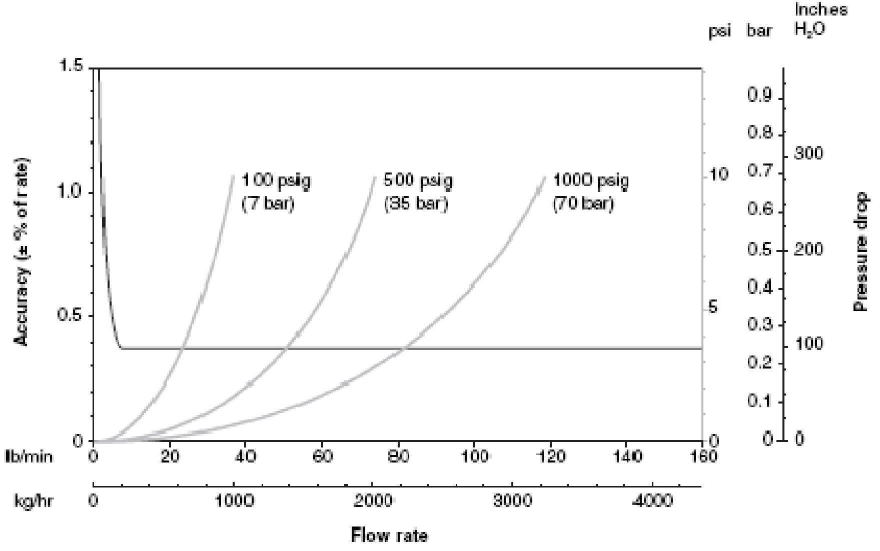

Standard or Normal Volumetric Capability

Standard and normal volumes are "quasi mass" flow units for any fixed composition fluid. Standard and normal volumes do not vary with operating pressure, temperature, or density. With knowledge of density at standard or normal conditions (available from reference sources), a Micro Motion meter can be configured to output in standard or normal volume units without the need for pressure, temperature, or density compensation. Contact your local sales representative for more information.

Density performance (liquid only)

		With 2400S transmitter or enhanced core processor		With transmitter with MVD Technology (except Model 2400S), standard core processor, or RFT9739 transmitter		With IFT9701 transmitter	
		g/cm^3	kg/m^3	g/cm^3	kg/m^3	g/cm^3	kg/m^3
Accuracy(1)	Model CMF010 and high-temperature models	±0.0005	±0.5	±0.0005(2)	±0.5(2)	±0.002(2)	±2.0(2)
	All other models	±0.0002	±0.2	±0.0005	±0.5	±0.002	±2.0
Repeatability	Model CMF010 and high-temperature models	±0.0002	±0.2	±0.0002(2)	±0.2(2)	±0.001(2)	±1.0(2)
	All other models	±0.0001	±0.1	±0.0002	±0.2	±0.001	±1.0
Range	All models	up to 5	up to 5000	up to 5	up to 5000	up to 5	up to 5000

---

(1) *Accuracy includes the combined effects of repeatability, linearity, and hysteresis. Specifications for ±0.0002 g/cm^3 (±0.2 kg/m^3) density accuracy are based on reference conditions of water at 68 to 140 °F (20 to 60 °C) and 15 to 30 psig (1 to 2 bar). All other accuracy specifications are based on reference conditions of water at 68 to 77 °F (20 to 25 °C) and 15 to 30 psig (1 to 2 bar), unless otherwise noted.*

(2) *For these combinations of sensors and transmitters, density accuracy and repeatability differ slightly from standard meter performance. Contact Micro Motion for performance data.*

Power consumption

Meter with core processor	4 watts maximum
Meter with Model 2400S transmitter	7 watts maximum
Meter with Model 1700/2700 transmitter	Refer to transmitter documentation

Vibration limits

Meets IEC 68.2.6, endurance sweep, 5 to 2000 Hz, 50 sweep cycles at 1.0 g

Temperature specifications

Accuracy	All models	±1 °C ± 0.5% of reading in °C
Repeatability	All models	±0.2 °C
Temperature limits[1]	All models except high-temperature models[2]	

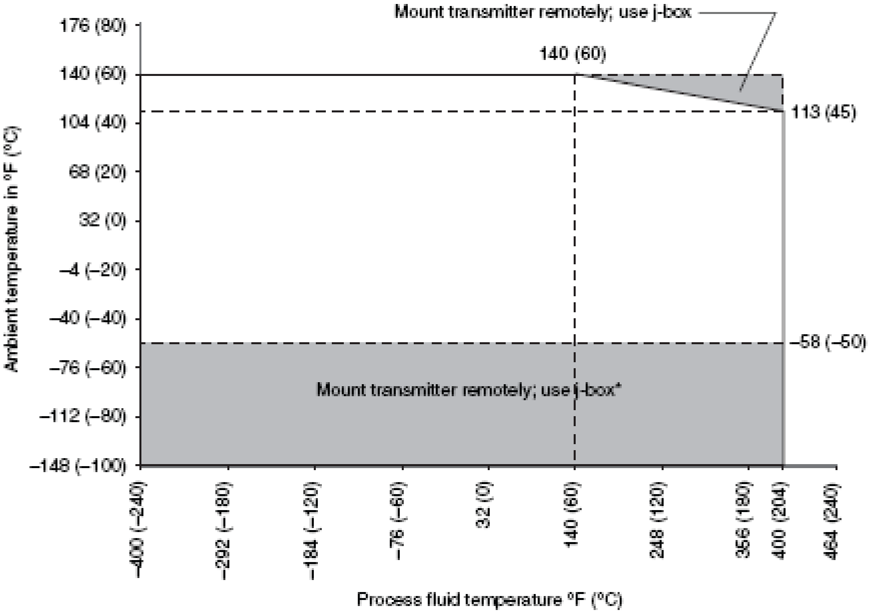

* *When ambient temperature is below –58 °F (–50 °C), a core processor or Model 2400S transmitter must be heated to bring its local ambient temperature to between –58 °F (–50 °C) and +140 °F (+60 °C). Long-term storage of electronics at ambient temperatures below –58 °F (–50 °C) is not recommended.*

---

(1) Temperature limits may be further restricted by hazardous area approvals. See pages 13–20.

(2) The extended mount option allows the sensor case to be insulated without covering the transmitter, core processor, or junction box, but does not affect temperature ratings.

Temperature specifications *continued*

Temperature limits[1]

High-temperature models

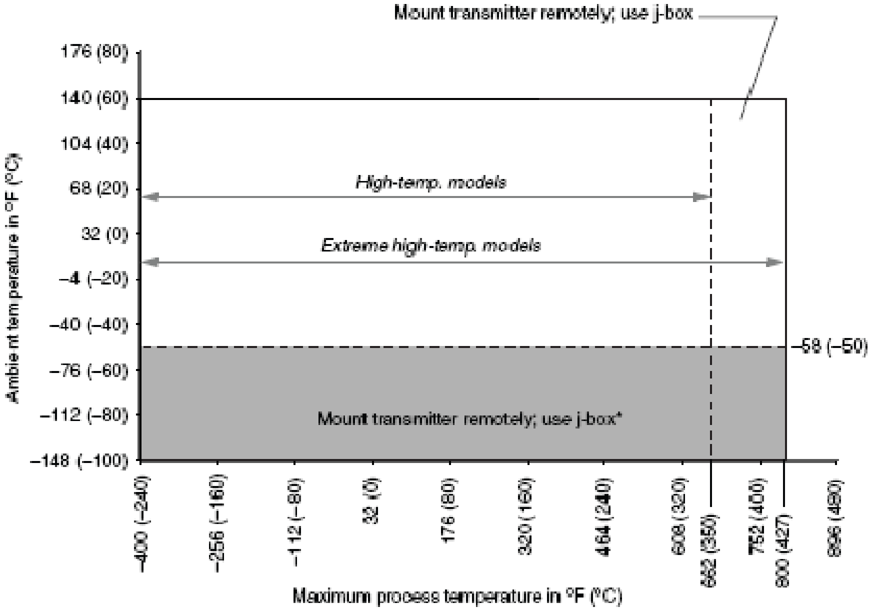

* *When ambient temperature is below –58 °F (–50 °C), a core processor or Model 2400S transmitter must be heated to bring its local ambient temperature to between –58 °F (–50 °C) and +140 °F (+60 °C). Long-term storage of electronics at ambient temperatures below –58 °F (–50 °C) is not recommended.*

---

[1] *Temperature limits may be further restricted by hazardous area approvals. See pages 13–20.*

Pressure ratings

Flow tube rating(1)		**psi**	**bar**
	316L and 304L stainless steel sensors	1450	100
	Hastelloy C-22 sensors	2160	148
	High-pressure CMF010P	6000	413

PED compliance	Sensors comply with council directive 97/23/EC of 29 May 1997 on Pressure Equipment

		ASME B31.3 secondary containment rating(1)		**Burst pressure**	
Housing rating		**psi**	**bar**	**psi**	**bar**
	CMF010(2)	425	29	3042	209
	CMF025	850	58	5480	377
	CMF050	850	58	5280	304
	CMF100	625	43	3299	227
	CMF200	550	37	2786	192
	CMF300	275	18	1568	108
	CMF400	250	17	1556	107

(1) For operating temperatures above 300 °F (148 °C), pressure needs to be derated as follows. Linear interpolation may be used between values.

	Flow tubes			***Housing***
	316L sensors	***304L sensors***	***Hastelloy C-22 sensors***	***All sensors***
up to 300 °F (up to 148 °C)	*None*	*None*	*None*	*None*
at 400 °F (at 204 °C)	*7.2% derating*	*5.4% derating*	*None*	*5.4% derating*
at 500 °F (at 260 °C)	*13.8% derating*	*11.4% derating*	*4.7% derating*	*11.4% derating*
at 600 °F (at 316 °C)	*19.2% derating*	*16.2% derating*	*9.7% derating*	*16.2% derating*
at 650 °F (at 343 °C)	*21.0% derating*	*18.0% derating*	*11.7% derating*	*18.0% derating*
at 700 °F (at 371 °C)	*22.8% derating*	*19.2% derating*	*13.7% derating*	*19.2% derating*
at 750 °F (at 399 °C)	*24.0% derating*	*20.4% derating*	*15.0% derating*	*20.4% derating*
at 800 °F (at 427 °C)	*25.7% derating*	*22.2% derating*	*16.3% derating*	*22.2% derating*

(2) Optional rupture disks for high-pressure CMF010P will burst if pressure inside sensor housing reaches 400 psi (27 bar).

Dimensions

Dimensions in *inches (mm)*

CMF010 with enhanced core processor or Model 2400S transmitter

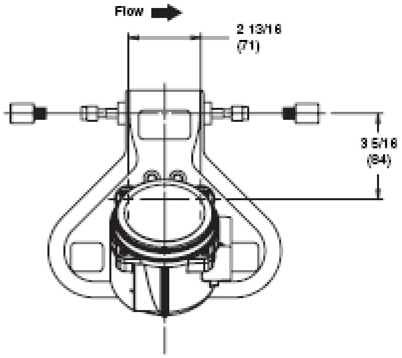

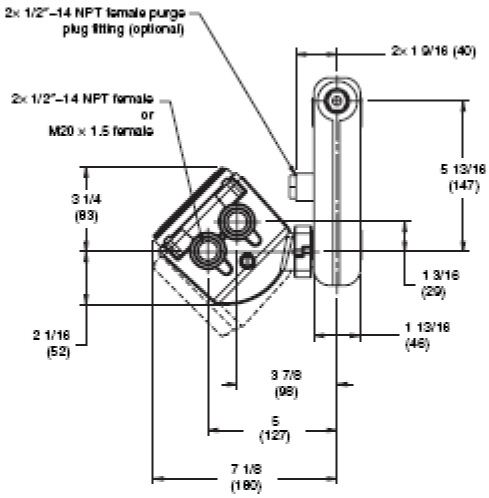

Refer to CMF010 drawings on page 23 for additional sensor dimensions. For CMF010 fitting options and dimensions, see page 40.

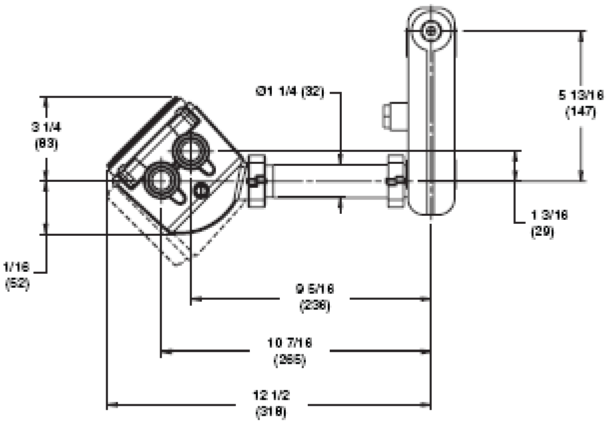

Extended mount option

Dimensions *continued*

Dimensions in $\frac{\textit{inches}}{\textit{(mm)}}$

CMF010 with core processor

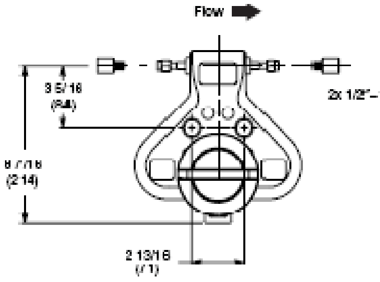

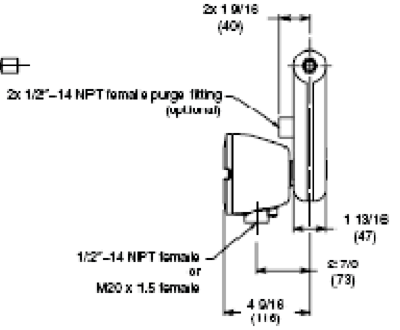

Extended mount option

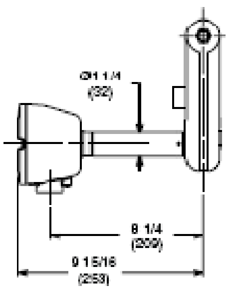

CMF010 with junction box

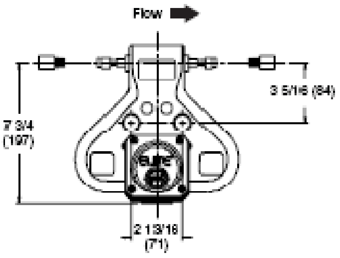

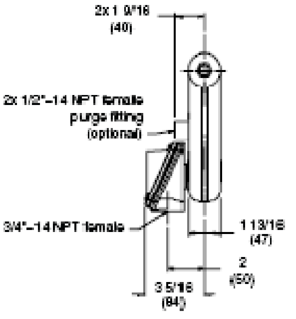

Extended mount option

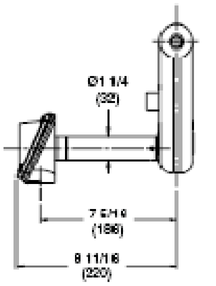

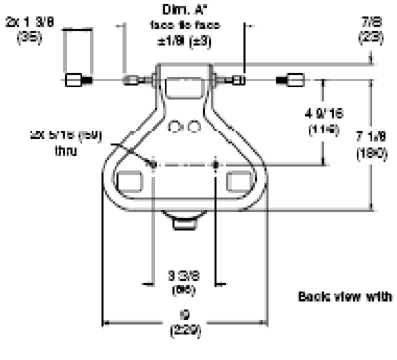

Back view with union fittings

Side view with rupture disks

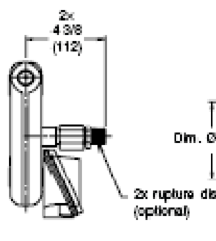

Flange dimensions

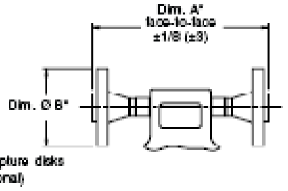

*For dimensions A and B, see page 40.